Center for Experimental Nuclear Physics and Astrophysics

University of Washington

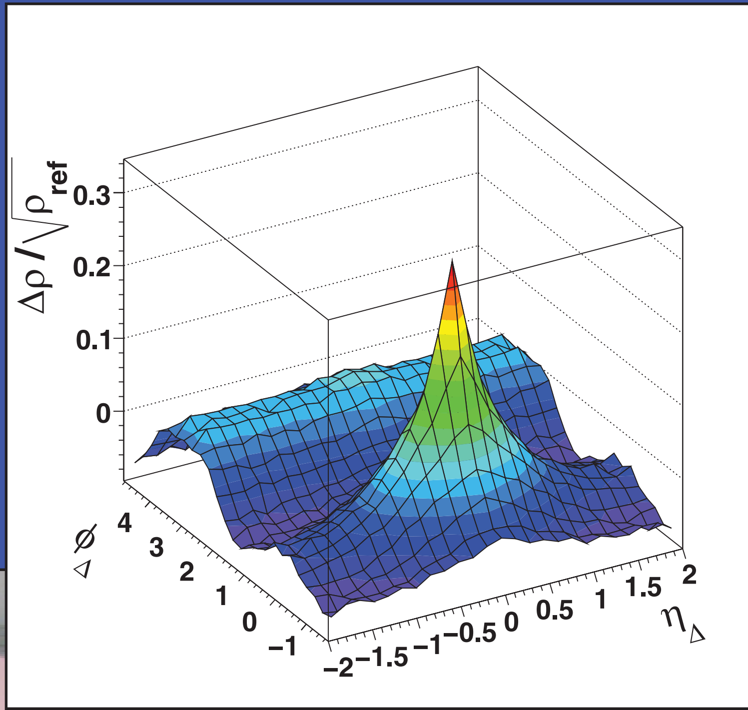

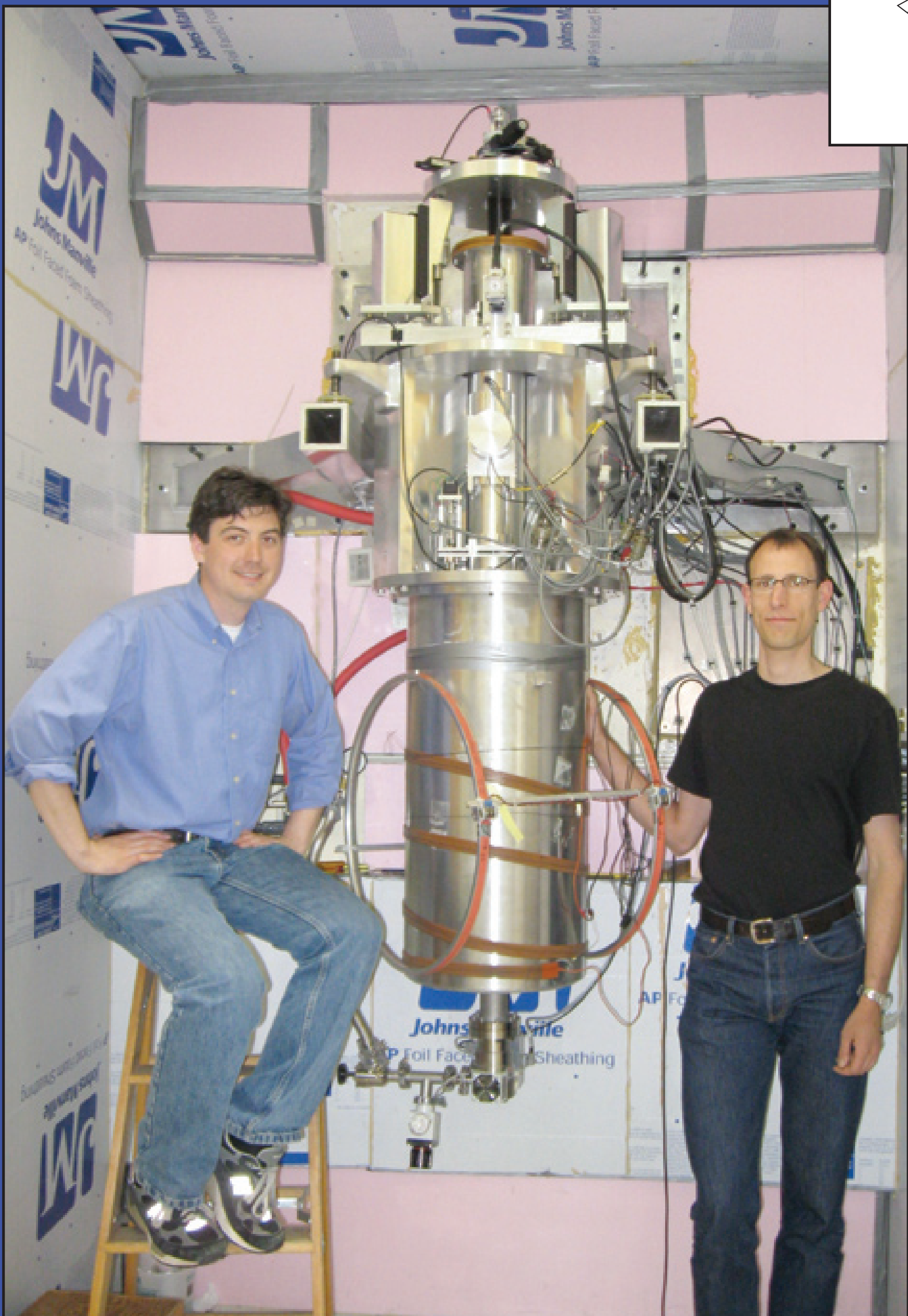

Annual Report 2009

ANNUAL REPORT

Center for Experimental Nuclear Physics and Astrophysics
University of Washington
May, 2009

Sponsored in part by the United States Department of Energy
under Grant #DE-FG02-97ER41020.

This report was prepared as an account of work sponsored in part by the United States Government. Neither the United States nor the United States Department of Energy, nor any of their employees, makes any warranty, expressed or implied or assumes any legal liability or responsibility for accuracy, completeness or usefulness of any information, apparatus, product or process disclosed, or represents that its use would not infringe on privately-owned rights.

The upper, right cover figure is from an analysis of semi-peripheral 200 GeV Au-Au collisions measured in the STAR detector at RHIC. It shows the two-particle correlation strength for particles separated in azimuth by ϕ_Δ and in psuedo-rapidity by η_Δ. There is a prominent same-side peak centered at $(\eta_\Delta, \phi_\Delta) = (0, 0)$ and an away-side ridge at $\phi_\Delta = \pi$. Those two features represent pairs of fragments (jets) from large-angle scattering of partons. There is also a $\cos(2\phi_\Delta)$ structure which has a small amplitude for this centrality and is conventionally associated with elliptic flow. A close look also shows a small ridge at $\eta_\Delta = 0$ due to longitudinal fragmentation of projectile nucleons.
Figure provided by Duncan Prindle.

The left cover photo shows Seth Hoedl and Frank Fleischer next to the axion-search torsion balance. The experiment is designed to look for axions by trying to measure the macroscopic force mediated by them. The right, center photo is of Alexis Schubert installing the first functional detector into a mechanical, electrical, and thermal test cryostat for MAJORANA at LANL. The right, bottom photo shows Carin Schlimmer assembling her experiment to measure gravity gradients.
Photos by Vic Gehman and Greg Harper.

INTRODUCTION

The Center for Experimental Nuclear Physics and Astrophysics, CENPA, was established in 1998 at the University of Washington as the institutional home for a broad program of research in nuclear physics, astrophysics and related fields. Research activities are conducted locally and at remote sites. CENPA has been a major participant in the Sudbury Neutrino Observatory (SNO) and is presently a major participant in the KATRIN tritium beta decay experiment and the MAJORANA double beta decay experiment. Most recently, CENPA physicists have joined the SNO+ double beta decay experiment in Canada. The current program includes "in-house" research on nuclear astrophysics and fundamental interactions using the local tandem Van de Graaff, as well as local and remote non-accelerator research on fundamental interactions and user-mode research on relativistic heavy ions at the Relativistic Heavy Ion Collider at Brookhaven.

The 2008-9 period has seen dramatic change at CENPA. Assistant Professor Nikolai Tolich, who joined the faculty from Lawrence Berkeley Lab in the fall of 2007, has started a research program with SNO+. Professor John Wilkerson, a faculty member since 1994, accepted a position at the University of North Carolina and departed in January 2009. A search is underway for a faculty member to replace John. Our first CENPA Fellow, Research Assistant Professor Michael Miller, joined us from MIT in November and is leading our MAJORANA project. Professor Eric Adelberger, and Research Professors Kurt Snover and Derek Storm all retired within the past two years, but they remain active in research as Emeritus faculty. Derek served as the Director of the Nuclear Physics Laboratory (CENPA's predecessor) and Executive Director of CENPA for more than two decades. We take this opportunity to thank him for his exceptional and dedicated leadership.

Professor Hamish Robertson has taken over as Director of CENPA, and Greg Harper, Senior Research Engineer for many years, has accepted the position of Associate Director. This marks a change in management organization, with the positions of Executive Director and Scientific Director being eliminated in favor of the two described. Hamish was also appointed to the Boeing Distinguished Professorship last summer.

The DOE Office of Nuclear Physics, which provides our operating grant, reviewed our program in September 2008 and subsequently approved funding for a further three years (FY09-11), contingent on successful yearly continuation proposals. We thank our external advisory committee, Baha Balantekin, Stuart Freedman, and Bill Zajc, for their valuable recommendations and advice. The committee reviewed our program in July, 2008 in advance of the DOE panel review.

Results from the third phase of the Sudbury Neutrino Observatory (SNO) with our ^{3}He-filled proportional counters deployed to detect neutrons from the neutral-current disintegration of deuterium were published and reported at Neutrinos 2008 in Christchurch, NZ. The measured fluxes in the three reactions registered by SNO agreed with previous phases, leading to improved precision in the determination of the mixing angle θ_{12}, as well as providing a test of systematic uncertainties given the very different method.

For the SNO+ project we are in the process of replacing the SNO data acquisition software with an ORCA based system. So far we have coded the communication and readout of all the major electronics components used in SNO, and plan to have the entire DAQ system completed later this year. We have also measured the quenching factor for alpha particles in the liquid scintillator.

The construction of the detector system, the US contribution to KATRIN, has continued to make progress during the past year, albeit with some delays as vendors have encountered problems. One of the two superconducting magnets, the magnet support system, the multi-pixel Si PIN diode array, most of the vacuum system, and calibration equipment, have now been completed with support from both DOE and the University. The electronics has been completed and delivered by our colleagues at Forschungszentrum Karlsruhe.

On the MAJORANA R&D project, we have completed the design for a pulsed-reset preamplifier for the front-end of the detector amplifier chain. Fabrication of a prototype is beginning. New concepts for a mechanical design of the detector holders that lends itself to ultra-clean construction have been developed and prototyped.

Our efforts on target developments for an implanted ^{22}Na target paid off and we were able to halve the damage by the high intensity beams on the targets. We have now taken most of the data that we need to determine the consumption of ^{22}Na in explosive stellar environments. Although our data analysis is in progress we have already concluded that a resonance at $E_p \sim 198$ keV that was proposed based on indirect measurements and expected to dominate the consumption rate, actually does not contribute at all.

We published our work on the determination of the electron-capture branch from ^{100}Tc and started working on a similar experiment on ^{116}In that will take place later in 2009. Both these numbers will provide benchmarks for nuclear structure calculations for double-beta decays.

The UCNA collaboration published the first determination of the beta asymmetry using ultracold neutrons. Although the uncertainty in that publication was large at almost 5%, we now have in hand data that should determine the beta asymmetry to $< 1\%$ and we expect to take data within 2009 that could reduce the uncertainty down to $< 0.3\%$. At that level this measurement will be an important check on extraction of V_{ud} from nuclear beta decay and will likely be the best determination of the ratio of the axial to vector coupling constants.

A new upper limit on the permanent electric dipole moment of atomic mercury recently has been reported. The electric dipole moment is generated by interactions that violate time reversal symmetry. The UW result is the most sensitive test of time reversal symmetry violation on ordinary matter.

The test of the possibility of observer-to-observer communication with quantum nonlocality has continued. A new type of nonlinear crystal with vastly improved entangled-photon production is being designed into the experiment.

Work on the quantum mechanical DWEF model describing RHIC collisions has continued. It had been discovered that an additional term must be added to the formalism when imaginary potentials are used.

We have extended our measurements of 2D angular autocorrelations to determine the pt dependence of the azimuth quadrupole (v2) free of jet contributions and the A dependence of minijet angular correlations. We have also established a quantitative connection between minimum-bias jets in spectra and correlations and pQCD calculations of fragment distributions which indicates that almost all scattered partons survive to the final state in the form of correlated hadrons.

Three CENPA graduate students, Adam Cox, Erik Mohrmann, and Sky Sjue, obtained their Ph.D. degrees during the period of this report.

As always, we encourage outside applications for the use of our facilities. As a convenient reference for potential users, the table on the following page lists the capabilities of our accelerators. For further information, please contact Greg Harper, Associate Director, CENPA, Box 354290, University of Washington, Seattle, WA 98195; (206) 543-4080, or gharper@u.washington.edu. Further information is also available on our web page: http://www.npl.washington.edu.

We close this introduction with a reminder that the articles in this report describe work in progress and are not to be regarded as publications or to be quoted without permission of the authors. In each article the names of the investigators are listed alphabetically, with the primary author underlined, to whom inquiries should be addressed.

Hamish Robertson, Director

Greg Harper, Associate Director and Editor

Victoria Clarkson, Assistant Editor

TANDEM VAN DE GRAAFF ACCELERATOR

A High Voltage Engineering Corporation Model FN purchased in 1966 with NSF funds, operation funded primarily by the U.S. Department of Energy. See W. G. Weitkamp and F. H. Schmidt, "The University of Washington Three Stage Van de Graaff Accelerator," *Nucl. Instrum. Methods* **122**, 65 (1974). Recently adapted to an (optional) terminal ion source and a non-inclined tube #3, which enables the accelerator to produce high intensity beams of helium and hydrogen isotopes at energies from 100 keV to 7.5 MeV.

Some Available Energy Analyzed Beams

Ion	Max. Current (particle μA)	Max. Energy (MeV)	Ion Source
^{1}H or ^{2}H	50	18	DEIS or 860
^{3}He or ^{4}He	2	27	Double Charge-Exchange Source
^{3}He or ^{4}He	30	7.5	Tandem Terminal Source
^{6}Li or ^{7}Li	1	36	860
^{11}B	5	54	860
^{12}C or ^{13}C	10	63	860
*^{14}N	1	63	DEIS or 860
^{16}O or ^{18}O	10	72	DEIS or 860
F	10	72	DEIS or 860
* Ca	0.5	99	860
Ni	0.2	99	860
I	0.001	108	860

*Negative ion is the hydride, dihydride, or trihydride.

Additional ion species available including the following: Mg, Al, Si, P, S, Cl, Fe, Cu, Ge, Se, Br and Ag. Less common isotopes are generated from enriched material.
In addition, we have produced a separated beam of 15-MeV ^{8}B at 6 particles/second.

BOOSTER ACCELERATOR

See "Status of and Operating Experience with the University of Washington Superconducting Booster Linac," D. W. Storm *et al.*, Nucl. Instrum. Methods A **287**, 247 (1990). The Booster is presently in a "mothballed" state.

Contents

1 Neutrino Research

SNO

1.1 Status of the SNO project

N. S. Oblath, R. G. H. Robertson, N. R. Tolich, B. VanDevender,
H. S. Wan Chan Tseung, J. F. Wilkerson*, plus the SNO Collaboration.

The primary scientific goal of the Sudbury Neutrino Observatory (SNO) experiment was to measure the flux of the different neutrino flavors coming from the sun in order to understand the solar neutrino anomaly. Data taking ended in November, 2006, and since then all efforts have focussed on analysis of the recorded data. The three distinct phases of the experiment each measured the total flux for all three light neutrino flavors in a different way. Data from the first two phases[1,2] confirmed that the solar neutrino anomaly was due to the nature of the neutrino, with neutrinos changing from electron neutrinos at production in the sun to an admixture of all three light neutrino flavors by the time they reached detectors on the earth. However, these two phases had a strong correlation between the measured electron neutrino flux and the total neutrino flux. For the third phase, proportional counters filled with ^{3}He were deployed within the heavy water in the SNO detector, allowing for an independent measurement of the total neutrino flux.

In June, 2008, the SNO collaboration published[3] an analysis of the third phase data that agreed with the result from the previous two phases and reduced the uncertainty on the neutrino mixing angle θ_{12}. Because this data was collected with a new detector system, there were a number of systematic error estimates and new analyses that had to be completed for this paper. People at CENPA were involved in many aspects of this analysis, and much of this has been described in last years annual report[4]. In the last year Noah Oblath led the group developing a simulation of the pulse shapes caused by various sources of charged particles in the proportional counters. This resulted in probability density functions versus energy for alpha particles from various sources that included a full accounting of the systematic errors due to inaccuracies in their simulation model. The largest systematic error came from not knowing the depth from the inner surface for alphas from ^{210}Po decays. Although these were assumed to come from the surface, due to a surface layer of ^{210}Pb from ^{210}Rn decay, there was evidence for migration with a depth of approximately 1 μm. Nikolai Tolich led the group responsible for extracting the neutrino flux from the data. In order to handle systematic errors more rigorously than previous SNO analyses, this group decided to use a new method based on a Markov Chain Monte Carlo method and Bayesian statistics. After the release of the first results from the third phase, Noah Oblath has worked on developing a method to distinguish neutrons and alphas in the proportional counter data, in an effort to remove a significant background, reducing both statistical and systematic errors.

---

*Currently at the University of North Carolina
[1] B. Aharmim, *et al.*, Phys. Rev. C **75**, 045502 (2007).
[2] B. Aharmim, *et al.*, Phys. Rev. C **72**, 055502 (2005).
[3] B. Aharmim, *et al.*, Phys. Rev. Lett. **101**, 111301 (2008).
[4] CENPA Annual Report, University of Washington (2008) p. 1.

The SNO experiment is unique, and there is a commitment to optimize the analysis of these data as this will likely provide the best constraint on the neutrino mixing angle θ_{12} for the foreseeable future. In order to achieve this there has been an effort underway for a number of years to lower the energy threshold for the previous analyses of the first two phases from 5 MeV to 3.5 MeV. This process is reaching a conclusion with blindness removed, and the final analysis currently underway. As analysis co-ordinator Nikolai Tolich has ensured that this analysis proceeded with a thorough internal review. Once this analysis is completed, there is a plan to combine it with an analysis of the final phase, providing the most complete analysis of the SNO data.

As analysis co-ordinator Nikolai Tolich has also overseen the completion of a paper[5] measuring the flux of both muons and neutrinos produced in cosmic ray showers. The depth of SNO uniquely allowed for a measurement of the atmospheric neutrino flux coming from above the horizon where the neutrinos were not expected to have undergone neutrino oscillations. There is also an on-going analysis searching for so-called hep neutrinos from the sun. The predicted flux for these neutrinos has a large uncertainty, and SNO has previously published limits based on the first phase data. However, there is a prospect that with data from all three phases we would observe a signal if it were at the upper limit of expectations. Finally, there are also searches underway for “exotic” physics, such as fractionally charged particles, neutron anti-neutron oscillations, and astronomical sources.

[5]B. Aharmim, *et al.*, submitted to Phys. Rev. D (2009).

1.2 NCD pulse fitting with simulated-pulse libraries

N. S. Oblath

We have previously developed a unique and detailed pulse simulation for the SNO Neutral Current Detection system[1]. With the goal of using the simulation to separate neutron-capture signal events from the alpha-decay backgrounds, simulated neutron-capture and alpha pulses are used to fit the NCD data.

Due to the speed of the NCD pulse simulation it is impractical to simulate pulses during the fitting process. Instead libraries of pulses are created before fitting. Three libraries are used: neutron captures, wall alphas (alphas originating from decays in or on the NCD walls), and wire alphas (from decays in or on the NCD anode wires).

The variety of neutron and alpha pulse shapes, real and simulated, is a result of the initial energy and the location and direction of the ionization track inside the NCD. Four coordinates define the parameter spaces of the neutron and alpha simulations, and the pulses in each library are simulated on a grid in each space. For neutrons, the parameters are the track direction, the position of the capture along the counter, and the capture radius from the anode wire. For alphas the radius is constant but the initial energy varies. Each library is composed of approximately 3,500 pulses. This particular library size was optimized for each library to cover the various pulse shapes sufficiently without making the fits take too long.

Each pulse in a data set is fit with all pulses in a library. The fit region of each data pulse extends from the leading edge (10% of the pulse amplitude) to beginning of the ion tail. A χ^2 is calculated for the comparison of each library pulse to a data pulse. An additional term is added to the χ^2 to account for the energy difference between data and library pulses.

The result is a fit that reliably finds a simulated pulse shape to match the events in the NCD data set. The quality of the fits was verified by using neutron calibration pulses and alpha pulses from the ^{4}He strings. Fig. 1.2-1 shows a neutron pulse fit with the neutron library (left), and an alpha pulse fit with the alpha library (right). This fitting algorithm is being used to determine the number of neutrons detected by the NCDs (see Sec. 1.3).

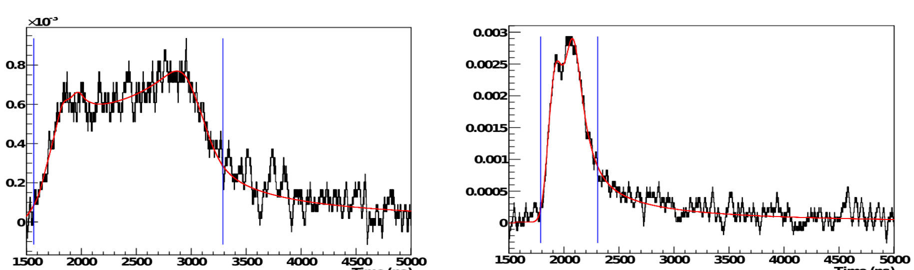

Figure 1.2-1. Examples of a neutron (left) and alpha (right) pulse fit.

[1] CENPA Annual Report, University of Washington (2008) p. 5.

1.3 Development of a background-free NCD pulse-shape analysis

N. S. Oblath

We have developed a method for determining the number of neutron captures in the SNO NCD data set based on pulse shapes. We fit the NCD pulses with libraries of signal and background events (see Sec. 1.2) to identify a subset of neutron-capture pulses that are unique from the alpha backgrounds.

A data pulse is fit with the neutron library and the alpha (wall & wire) library, producing two fit results, χ^2_n and χ^2_α. In Fig. 1.3-1 the left plot shows neutron and alpha events in the two-dimensional parameter space, $\log(\chi^2_\alpha)$ versus $\log(\chi^2_n)$. There is a distinct region of the parameter space that is almost entirely free of alpha events.

A linear combination of the two χ^2 values can be used to simplify the event discrimination: $\Delta\log(\chi^2) \equiv \log(\chi^2_\alpha) - \log(\chi^2_n)$. The right plot in Fig. 1.3-1 shows the $\Delta\log(\chi^2)$ distribution for neutron captures, alpha events, and the full NCD data set. The alphas fall in a single peak near zero. The neutrons also exhibit a peak around 0, which is composed of pulses that resemble alpha events. Additionally, however, there is a shoulder of neutron capture events that is composed of pulses that look uniquely like neutron-captures.

Alpha pulses are created by a single ionizing alpha particle, whereas neutron pulses are a result of a back-to-back proton/triton pair. When the proton and triton travel parallel to the anode wire they create a pulse that resembles an alpha event. When they travel perpendicular to the anode wire the two-particle structure is revealed. The pulses created by a perpendicular ionization track are easily distinguishable from alpha pulses.

Since there is limited information about the shape of the alpha $\Delta\log(\chi^2)$ distribution ($\approx 1,000$ events on the ^{4}He strings, versus $\approx 80,000$ neutron events from the ^{24}Na calibrations), systematic errors resulting from the alpha backgrounds can be minimized by using a background-"free" cut. The cut fraction for neutron pulses is well-determined by the ^{24}Na calibrations. A preliminary cut removes $\approx 99\%$ of the alpha events, while keeping $\approx 38\%$ of the neutron-capture events. By cutting so many signal events the statistics become the dominant source of error. Optimization of the cut is currently underway to minimize the total error.

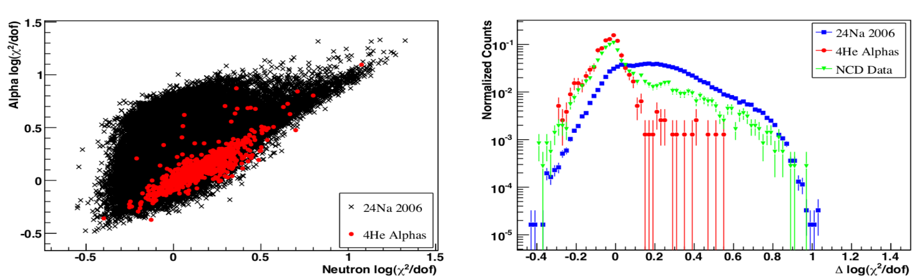

Figure 1.3-1. The two-dimensional (left) and one-dimensional (right) χ^2 space.

SNO+

1.4 Status of the SNO+ experiment

M. A. Howe*, J. Kaspar, J. K. Nance, N. R. Tolich, H. S. Wan Chan Tseung, and J. F. Wilkerson*

The Sudbury Neutrino Observatory (SNO) project ended data taking in November, 2006. Filling the detector with a liquid scintillator will transform the SNO experiment into the SNO+ project. The scintillator will provide 25 times more photoelectrons per electron than the Cherenkov process in SNO, which will improve the energy resolution and allow the energy threshold to be decreased. The SNO+ project is being built upon existing infrastructure of the SNO experiment allowing for a shorter time to the first data, which is expected in 2011.

The diverse scientific goals address fundamental questions in particle physics, astrophysics, and geosciences. In particular, adding ^{150}Nd to the scintillator will enable a search for neutrino-less double-beta-decay with the neutrino mass sensitivity of 50 meV (5σ c.l.). SNO+ will detect geoneutrinos, i.e., electron antineutrinos from natural radioactivity in the earth, to understand the radiogenic component of the earth's heat flow, and to test competing models of the composition of the continents. The measurement is possible thanks to the position of the detector in a well-studied continental crust in a region with low background from nuclear reactors. However, the reactor signal still allows SNO+ to detect antineutrinos from distant reactors and to observe spectral distortions due to neutrino oscillations. Before Nd is added to the scintillator, SNO+ will measure the low-energy solar neutrinos (pep and CNO reactions) to report on the sterile neutrino admixture, non-standard interactions, and sun's metallicity. Finally, the SNO+ will maintain excellent supernova neutrino capabilities.

CENPA has been active in the Monte Carlo group working on energy and position fitters. New fitters are under development to handle scintillation light which is uniform in direction. In the SNO project the information on position came from the Cherenkov cone which is now strongly suppressed by the scintillation light. This work has been accompanied by a detailed understanding of the optical properties of the SNO+ setup.

A dedicated measurement of the SNO+ scintillator was performed in summer 2008. A bucket filled with the scintillator was placed into the center of the detector filled with water. We have contributed to the analysis of the bucket data focusing on energy resolution and quenching of the alpha lines coming from Rn dissolved in the scintillator. This analysis is critical for determining the detector response to different ionizing particles and for determining sensitivity to neutrino mass, since it depends directly on the energy resolution achieved.

The UW group has been leading the DAQ task to deliver a new ORCA based system to read out SNO+ data. ORCA was used to read out data from the proportional counters in the final SNO phase. The present system to read out the PMT data in SNO could not handle two orders of magnitude higher data rate from the scintillator. The new system is under development to be delivered in fall 2009.

*University of North Carolina, Chapel Hill, NC

1.5 ORCA DAQ system for SNO+

M. A. Howe*, J. Kaspar, N. R. Tolich, and J. F. Wilkerson*

The scintillator filling the SNO+ detector will provide 25 times more photoelectrons per electron than the Cherenkov process in SNO, which will improve the energy resolution and allow the energy threshold to be decreased. However, the present data acquisition system, based on OS9 and SUN computers mastering VME crates controlled by a Motorola embedded CPU, cannot handle such a data rate, and is not scalable enough to be upgraded in a reasonable and reliable way. Therefore, it is necessary to develop a new DAQ system.

The new DAQ system is based on ORCA, which was developed in CENPA led by Mark Howe. ORCA is a general purpose, highly modular, object-oriented, acquisition and control system that is easy to use, develop, and maintain. It has been well received in the final SNO phase to read out the proportional counters. Its general-purpose design enables moving from a master-slave paradigm towards more independent standalone units. The former SNO and future SNO+ topologies are compared in Fig. 1.5-1.

A test stand located in Sudbury has been used for our DAQ development. It allows us to run both the former SHaRC and the future ORCA system in parallel to cross-check the outputs. We have managed to initialize, control, and read out all the hardware devices in the SNO+ setup with ORCA. We have developed a control code for the single board computer mastering the interface crate running Linux (see Sec. 7.6). Now we are proceeding with the run control, hardware calibration and validation. The first underground tests are scheduled for May, 2009. The full DAQ system will be running in fall 2009. Besides the DAQ system itself we have also started to code the DAQ part of the Monte Carlo model of the SNO+ detector.

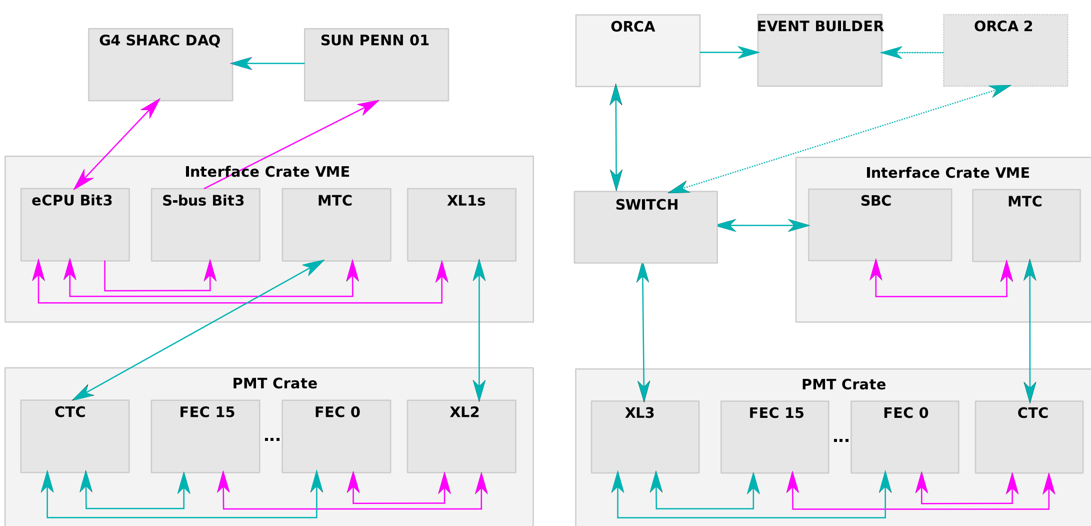

Figure 1.5-1. The left figure shows a DAQ scheme for the PMT readout in SNO. The right figure shows the planned DAQ scheme for the SNO+ . Only one out of nineteen PMT data crates is shown.

*University of North Carolina, Chapel Hill, NC

1.6 Quenching and energy resolution of alpha lines in SNO+

N. R. Tolich and H. S. Wan Chan Tseung

During October 2008, several calibrations were carried out to study the optical properties of the SNO+ scintillator. A cylindrical acrylic container containing about 1 L of scintillator was deployed within the SNO acrylic vessel, which was filled with water. The scintillation light yield L from electrons (in units of phototube hits per MeV) was obtained by positioning an AmBe neutron source near the bucket, and locating the Compton edges of the 2.2 MeV neutron-capture γ and the 4.4 MeV γ from the first excited state of ^{12}C. Corrections due to Cherenkov light contributions, multi-photon hits and random noise triggers were applied[1].

We measured the quenching of alphas by using the decays of dissolved ^{222}Rn and its daughters, which produced two noticeable peaks below 1 MeV equivalent electron energy in the spectrum. The higher-energy peak was found to be predominantly composed of ^{214}Po α decays via the delayed coincidence method. The number of ^{214}Bi–^{214}Po coincidences decreased over time with a half life of about 4 days, confirming the presence of ^{222}Rn. The low-energy peak consisted mainly of ^{218}Po and ^{222}Rn alphas. The positions of these three alpha lines were obtained through Gaussian fits to the peaks, after subtracting out the underlying β–γ background, which is dominated by ^{214}Pb and ^{214}Bi decays. Monte Carlo studies indicated that the shape of the β–γ background spectrum can be approximated by a 6^{th} order polynomial. An example fit to a group of 8 runs, after β–γ removal, is shown in Fig. 1.6-1 (left), where the green-dashed, red-dashed and blue curves are the ^{222}Rn, ^{218}Po and ^{214}Po alphas, respectively. For Nd-doped scintillator, the corresponding quenching factors were 10.2 ± 0.8, 9.6 ± 0.8 and 8.1 ± 0.5, while the energy resolution was found to be $6.5\%/\sqrt{E}$ (MeV).

The quenching effect is well-described by Birks' law[2]. By using L and the three alpha peak positions, a value for Birks' constant can be extracted (Fig. 1.6-1, right). This was found to be 73.2 ± 3.6 μm/MeV.

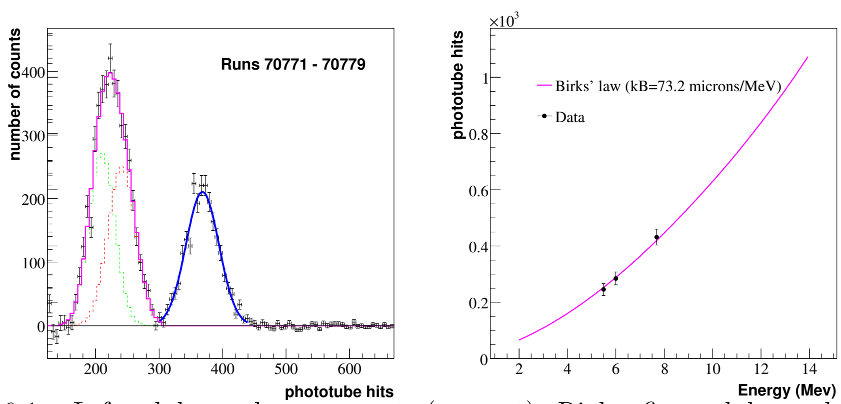

Figure 1.6-1. Left: alpha peak components (see text). Right: fit to alpha peak positions using Birks' law.

[1] Helen O'Keeffe (Queen's University), private communication.

[2] J. B. Birks, The theory and practice of scintillation counting, Pergamon Press, 1964.

1.7 Understanding light propagation in the SNO+ detector

J. K. Nance and N. R. Tolich

A significant source of backgrounds in any large spherical detector such as the SNO+ detector is external radiation either penetrating from the surrounding materials or present on the inner surface of the detector itself. In order to reduce the influence of those backgrounds, the SNO+ detector will implement a fiducial volume cut such that only events occurring well within the scintillation volume are accepted. Event reconstruction is then performed using timing and charge collection information from the surrounding photomultiplier tubes.

However, the nature of excitations in organic scintillating cocktails such as that proposed for use in SNO+ complicates the problem of event reconstruction. Because the scintillator can absorb and re-emit photons generated in an interaction, the original vertex of a physics event can become obscured and more difficult to understand. A GEANT4 based C++ Monte Carlo simulation is used to model the response of the detector to physics events in the scintillation volume, but information about the physics processes that take place in between the vertex and the photomultiplier tubes is lost.

Work is therefore currently being done to recover this lost information and make use of it in the event reconstruction process. It is hoped that the effect of position on the timing distributions can be determined and thus improve the PDFs used for reconstruction. Below is a figure which helps motivate this type of analysis. Shown in Fig. 1.7-1 is the photomultiplier tube hit time distribution for photons which reflected from surfaces outside the acrylic vessel in the SNO+ detector. At this level of the analysis, it demonstrates that there is a significant contribution to the spectrum from these reflections. Importantly, if the reflections occur outside the acrylic vessel, they should be independent of the position of the event inside the vessel, which is important information from the reconstruction perspective.

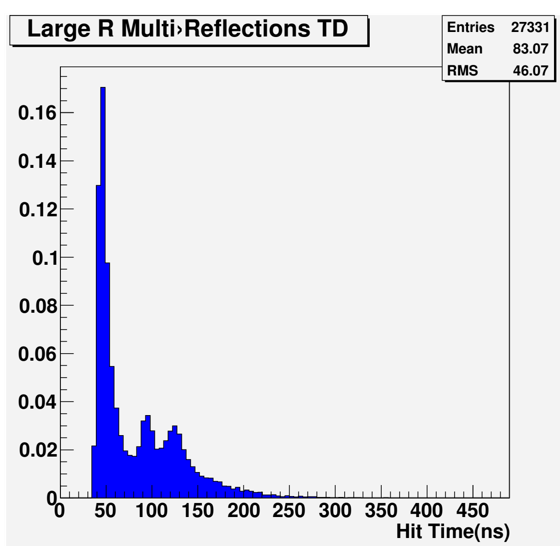

Figure 1.7-1. Simulated time spectrum for PMT hits caused by photons reflected from surfaces outside the SNO+ AV.

KATRIN

1.8 Status of the CENPA contribution to the KATRIN experiment

J. F. Amsbaugh, L. Bodine, T. H. Burritt, P. J. Doe , G. C. Harper, M. L. Leber, E. L. Martin, A. W. Myers, R. G. H. Robertson, K. Tolich, B. VanDevender, T. D. Van Wechel, B. Wall.

The KATRIN collaboration aims to set a limit on the neutrino mass to a sensitivity of 0.2 eV via a study of tritium beta decay. The main components of the experiment are a windowless, gaseous tritium source, a transport section that carries the beta electrons to a pair of electrostatic spectrometers and, finally, a detector system that measures the flux of electrons passing through the spectrometers. The US institutes, consisting of the University of Washington (UW), the Massachusetts Institute of Technology (MIT) and the University of North Carolina (UNC) are responsible for providing the detector system and the data acquisition software. The University of California, Santa Barbara (UCSB) has recently joined the US contingent and will be participating in diagnostics, simulations and analysis. The KATRIN project is currently at the height of its construction activities at the Forschungzentrum, Karlsruhe (FZK). The US is scheduled to complete installation of the detector at the FZK by December 2010, and data taking with tritium is expected to begin in September 2012.

Significant progress has been made in acquiring the main KATRIN components although challenges remain. Principal among these is the windowless gaseous tritium source (WGTS). The company originally contracted to supply this component was acquired, and the division responsible for supplying the WGTS was split off. A solution to this is in hand, and the WGTS is expected to be commissioned in early 2012.

Tritium gas emerging from the windowless source is returned via a differential pumping system (DPS). The DPS has passed its cooling tests and field mapping. Delivery is expected in May 2009. Tritium escaping the DPS is trapped by the cryogenic pumping system (CPS) in order to prevent tritium contaminating the spectrometers. Trapping is achieved by coating the walls of the beam pipe with argon snow. Delivery of the CPS is expected in September 2010. The spectrometer system consists of a pre-spectrometer that is used to filter out the uninteresting, low energy parts of the spectrum and a main spectrometer. The prespectrometer was delivered in 2004 and has been used to optimize the electrode design for the main spectrometer and study sources of backgrounds such as Penning traps. The main spectrometer, with a resolution of 0.93 eV, enables the precision measurement of the beta spectrum. This vessel, delivered in late 2006, has passed its vacuum commissioning and is currently having a field-shaping, background-suppressing electrode installed. Completion is expected in October 2009 after which the spectrometer will undergo electrostatic commissioning beginning in March 2010. Commissioning and background studies conducted with the pre and main spectrometers are being carried out with the data acquisition software supplied by the US.

Assembly and commissioning of the detector system is taking place at UW with MIT providing the calibration, and background control hardware, consisting of inert shielding and a scintillator veto. UNC is providing the DAQ software for the system.

Assembly has been slowed by delays in supplying certain critical components; the magnets, a custom, low background feedthrough, and the post acceleration electrode system, although resolution of these difficulties is underway.

The problem that prevented the pair of superconducting magnets from reaching their design field of 6T was traced to mismatched coefficients of expansion in the material chosen to wrap the magnet coil. This has now been rectified, and delivery is anticipated in early May 2009. The electroformed copper horn of the post acceleration electrode suffered blistering during the assembly brazing process. This component has now been replaced with a spun copper part, and delivery is expected in early May 2009, allowing completion of the vacuum system. Finally, the low background sapphire signal feedthough continues to experience manufacturing problems. While these are being resolved, two feedthroughs using standard, less radioactively clean, glass insulators have been ordered. This will allow testing of the electronics and evaluation of the detector wafers.

The detector wafers were received in July. They have met their dimensional tolerances, and room temperature leakage currents are within specifications. Further evaluation will take place upon receiving the custom signal feedthrough on which the detectors are to be mounted. The detector electronics have been received from FZK and are currently being assembled and commissioned. The vacuum system and pumping station have been assembled, with final commissioning awaiting the delivery of the post acceleration electrode and baking system.

The calibration system, provided by MIT, has been delivered to UW and installed on the vacuum system. A method of measuring the absolute efficiency of the detector by recording the photo current from the electron calibration source has been prototyped by UW and is undergoing testing.

The copper and lead shield and handling device has been completed at MIT and is ready to be shipped to UW. Measurements of the laboratory background as a function of shielding have begun and will be used to better understand the measured efficiency of the shield when tested in the laboratory. The veto is currently under construction at MIT with delivery expected in May 2009.

The background model continues to be improved and tested. Incorporating the results of the assays of detector materials gives us confidence that we will meet the background goal of 1 mHz. Testing of the Mk3 DAQ crate hardware has been carried out at UW, and the Mk4 version is expected in Fall 2009. The Slow Control system was delivered to UW in Fall 2008 with final commissioning expected in summer 2009.

A revised schedule accounting for the delays in equipment delivery has been produced. The fully commissioned detector system will be shipped to the FZK on July 2010 and installation is expected to be complete in December 2010.

1.9 Estimation of the environmental radioactivity in the KATRIN spectrometer hall

M. L. Leber, P. Renschler*, and S. Kage*

The detector-related backgrounds in the KATRIN experiment need to be under 1 mHz in the region of interest. By radio-assay of construction materials and using known cosmic ray fluxes, the background from these sources can be estimated with the existing KATRIN Geant4 simulation. A challenging background to estimate is the environmental radioactivity which originates in materials outside of the detector section. By measuring this background with a Germanium detector and comparing to an estimate from the simulation, we can make a projection about the rate in the KATRIN silicon detector.

Three measurements were made in the KATRIN prespectrometer hall with a Germanium detector: an unshielded measurement, a measurement inside 15 cm of lead shielding, and a measurement inside the 15 cm shield with a twelve-degree opening that matches the KATRIN shield. This combination of measurements allowed an estimate of the total flux of photons from radioactive decay and an estimate of the flux coming from the direction of the shield opening.

To simulate the environmental radioactivity, we assumed the initial unstable isotopes are embedded in concrete, so the emitted photons can Compton scatter within the source. This ensures that the spectrum incident on the germanium detector contains both full energy peaks and the photons which have already Compton scattered within the concrete. Uranium, Thorium, and Potassium are spread throughout the concrete surrounding the Germanium detector. The full-energy peaks were fit in the simulation and measurement to determine the area, or total number of counts. The simulation was then scaled to match the measurement and determine the total flux.

To estimate the angular dependence of the incident photons, the measurement with the completely closed shield was compared to the measurement with a twelve-degree opening in the shield. The full-energy peaks of each measurement were fit to determine the area. Photons entering through the opening were simulated, and the peak areas in the simulation were matched to the difference of the two measurements.

Finally, to determine the background in the KATRIN silicon detector, the initial energy spectra of photons determined by the unshielded measurements was used. The angular distribution of the photons was isotropic, except the rates were different through the shield opening and otherwise, as determined from the two shielded measurements. The background rate without post-acceleration is expected to be 0.92 mHz from the environmental radioactivity alone. Therefore, to reach our background goal of 1 mHz total, post-acceleration will be necessary.

*Forschungszentrum Karlsruhe, Institut für Experimentelle Kernphysik, Postfach 3640, 76021 Karlsruhe, Germany.

1.10 Monte Carlo Studies of low energy electrons incident on silicon

H. Bichsel, Z. Chaoui*, P. Renschler† and R. G. H. Robertson

The purpose of this simulation is to determine the energy loss of low-energy electrons (e.g. $E = 18.6\ keV$) in silicon for the KATRIN focal plane detector. Electrons backscattered from the detector surface will return to the detector due to magnetic reflection in the detector pinch magnet or electrostatic reflection at the main spectrometer. This leads to multiple passages through the detector surface layer (d≈100 nm) in which deposited energy does not contribute to the detector readout. Both effects are included in the simulation results shown in Fig. 1.10-1 and Fig. 1.10-2.

In Fig. 1.10-2 the effect of different inelastic cross sections on the simulation results is shown. One is obtained with a model dielectric function given by Penn[1], the other was calculated using the Bethe-Fano approach[2]. Assuming a cut at 1% of F(T), the observable energy windows differ by ≈16%.

In the current Monte Carlo program all energy lost by primary electrons is assumed to be deposited locally. Further studies[3] will show if there is a need for a more detailed simulation that also takes production and tracking of secondary electrons by atomic ionization and relaxation into account.

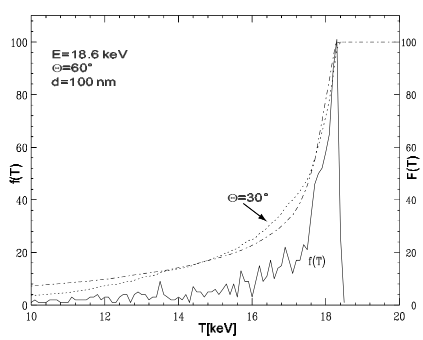

Figure 1.10-1. Spectrum f(T) shows energy lost in the sensitive volume for incident electrons with $E = 18.6\ keV$ and θ=60° (solid line). The dotted line shows the integral F(T). The chained line shows F(T) for θ=30°.

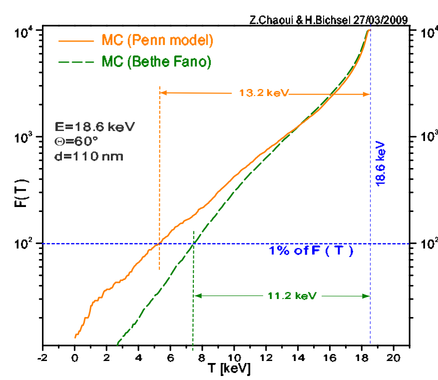

Figure 1.10-2. Comparison between two inelastic cross section models. Shown is F(T) obtained with the Penn and the Bethe-Fano approach for $E = 18.6\ keV$ and θ=60°.

*University of Setif, Algeria
†Karlsruhe Institute of Technology, Germany
[1]D.R. Penn, Phys. Rev. B **35** 482 (1987).
[2]H. Bichsel, Rev. Mod. Phys. **60** 663 (1988).
[3]Z. Chaoui *et al.*, Phys. Lett. A **373** 1679 (2009).

1.11 Status of the vacuum system for the KATRIN detector

J. F. Amsbaugh, T. H. Burritt, G. C. Harper, and K. Tolich

The sensitivity of KATRIN critically depends on minimizing background by avoiding interactions among particles along the path of electrons from the tritium source to the focal plane detector (FPD). Therefore the FPD will be placed in an extreme high vacuum (XHV) chamber whose design pressure is less than 10^{-10} mbar. The XHV chamber is separated from the main spectrometer by a DN250 gate valve. The XHV chamber provides mounts for its vacuum pumps, vacuum measuring equipment, the post-acceleration electrode, and the FPD calibration devices. Signals from the FPD exit the XHV chamber through a feedthrough flange and are fed into preamplifiers placed in a high vacuum (HV) chamber whose design pressure is less than 10^{-6} mbar. The HV chamber provides mounts for its vacuum pumps, vacuum gauges, a pulse tube cooler, and another signal feedthrough flange, through which signals exit the HV chamber. The initial rough pumping of each chamber is performed and monitored by its designated combination of roughing pumps and vacuum gauges, all of which reside on a mobile cart (roughing station). After rough pumping, the design pressure is achieved and maintained by a cryopump mounted on each chamber. The chambers and their accessories are supported by a stand that rolls on rails allowing adjustment of the vacuum system position.

Since the previous report[1], the majority of components for the vacuum system has been either delivered or manufactured onsite and assembled. The XHV chamber has been mounted on the stand, and the DN250 gate valve, the vacuum measuring devices, cryopump, and the FPD calibration devices are mounted on it. The HV chamber with its cryopump and gauges has been mounted on the XHV chamber. A prototype roughing station cart has been manufactured, and all the components housed by the cart are assembled. Fig. 1.11-1 shows a photograph of the vacuum system assembled as of April 30, 2009.

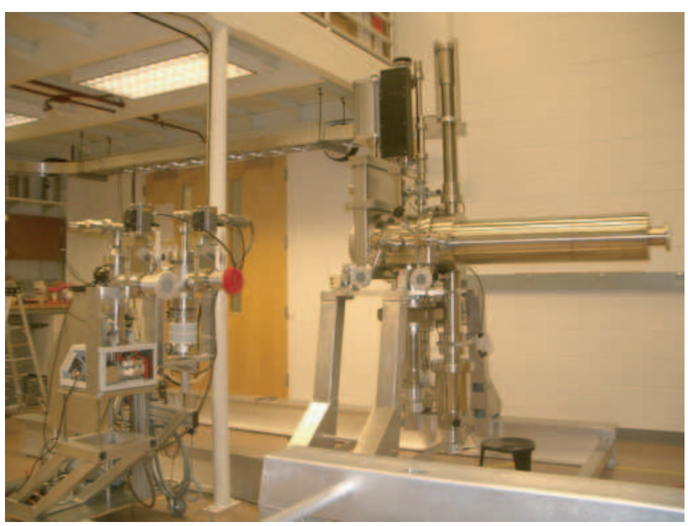

Figure 1.11-1. KATRIN FPD vacuum system assembly

[1] CENPA Annual Report, University of Washington (2008) p. 11.

1.12 Absolute efficiency calibration of KATRIN Si multipixel focal-plane detector

E. L. Martin, A. W. Myers, R. G. H. Robertson, and T. D. Van Wechel

In order to determine the absolute efficiency of the KATRIN focal-plane detector we intend to measure the electron current from a photoemissive electron gun and compare it to the count rate detected by the detector. This requires a precise current measurement of a femtoamp at a voltage of 20 kV.

PULCINELLA (Precision Ultra-Low Current Integrating Normalization Electrometer for Low-Level Analysis) is a current meter capable of measuring fA scale current. The low current measurement was accomplished by use of a current integrator and ADC from Texas Instruments, the DDC-114. For the scale used, full scale charge is 12 pC with 20 bit resolution. The chip contains reset circuitry and twin ADCs that alternate charge collection and readout switched by a supplied clock.

The ADC was placed on a single integrator board with a voltage regulator, oscillator, and FPGA used to control the ADC and convert the digital output to serial format and transmit it to a receiver board. To run the 5 V integrator board floating on 20 kV the power and output are optically isolated. Optical power isolation is accomplished with an array of LEDs and a solar panel while data are transmitted over a fiber optic cable.

The electron emitter to calibrate the focal-plane detector is a copper disc attached to an isolated shaft passing through a bellows to allow moving it in and out of the beam path from the KATRIN main spectrometer. UV light will pass through a sapphire window to illuminate the photoelectrode.

To remove zero current offsets the UV light will be pulsed and status of the light will also be sent to the receiver board and packaged with the charge measurement data. The receiver board also adds an incremental counter for data loss detection and converts the data to an Ethernet signal that can be downloaded to a computer.

PULCINELLA was calibrated using a square wave generator with a voltage divider and a 5 GΩ resistor to generate a pulsed 9.24 pA signal. Due to uncertainty on the measurement of the voltage and the value of the 5 GΩ resistor systematic uncertainty was 1.6%. Full scale charge was found to be 11.8 pC with negligible statistical uncertainty.

Each charge measurement cycle takes from 10 to 2550 ms. The major noise contribution to individual charge measurements was independent of integration time, favoring long measurement cycles for accurate results. Noise was 0.87 fC rms at 20 ms (44 fA) and .98 fC at 1 s (.98 fA).

1.13 Status of the superconducting magnets for KATRIN

L. I. Bodine, R. G. H. Robertson, and D. I. Will

The two superconducting solenoidal magnets for KATRIN[1] are being manufactured by Cryomagnetics, Inc., Oak Ridge, TN. Construction of the pinch magnet system has been completed and preliminary tests of the system have been performed. The pinch system can safely maintain the full 6 T central field and survive a heater induced quench. The detector magnet system is nearing completion. Installation in the cryostat (see Fig. 1.13-1) is the only remaining construction task.

Our lab in the Physics Astronomy Building (B037) has been prepared for the magnets. A layout that does not conflict with neighboring, field-sensitive experiments has been found and the magnet stands as well as the necessary electrical and water connections have been installed. The necessary cryogen transfer equipment is available and a cryogen supplier has been identified.

A preliminary integration of the magnet electronics with the KATRIN Slow Control system has been completed. The temperature sensors, cryogen level sensors and the power supplies can be computer controlled and the final test of the integration will be completed upon the magnets' arrival at UW.

D. I. Will has been designated as the safety officer and has designed a mandatory superconducting magnet safety training. The training will take place following the testing of the magnets at Cryomagnetics, Inc.

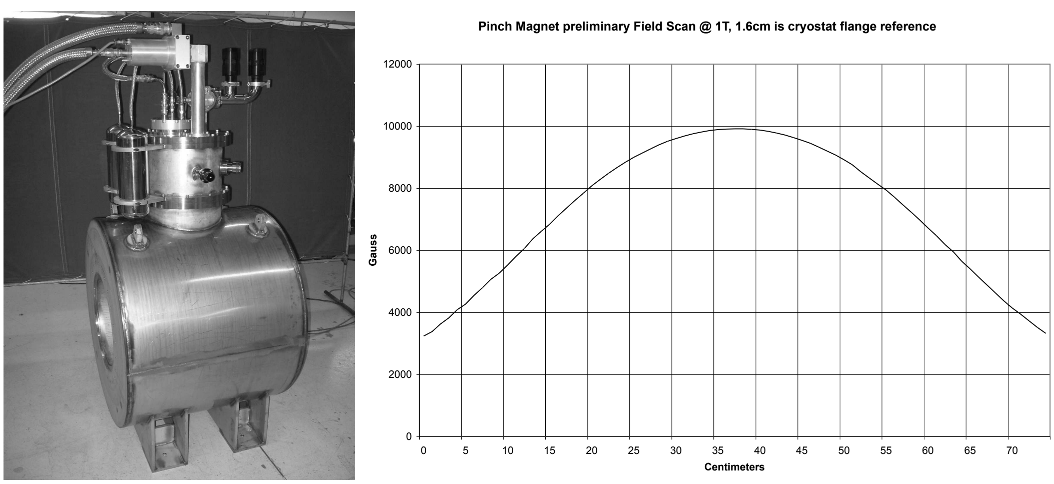

Figure 1.13-1. The left panel shows a picture of the completed pinch magnet system. The right panel shows an axial scan of the magnetic field of the pinch coil system with a 1 T central value

[1]CENPA Annual Report, University of Washington (2008) p. 15.

1.14 Preparations for KATRIN FPD electronics commissioning

B. VanDevender, B. L. Wall

The Institut fur Prozessdatenverarbeitung und Elektronik at the Forschungszentrum Karlsruhe has designed and built a commissioning set of electronics. The electronics for the KATRIN Focal Plane Detector (FPD) consists of 4 major parts and works as follows. The Power And Control (PAC) board provides power regulation to the preamplifier boards. It controls the preamp module and channel multiplexing. It measures leakage currents, temperatures and bias voltages, and sets the variable gains on the Optical Sender board. The PAC board is connected to 24 preamp modules via an interface board that distributes the power and multiplexing signals and returns the temperature and leakage current read out voltages. Each preamp module has 6 or 7 channels providing the 148 channels needed for the FPD. The signals from the 24 modules are connected to the Optical Sender board which provides a secondary amplification stage and converts the charge signal to optical. The optical signals are received by the IPE crate which is equipped with Optical Receiver boards. Each signal is then converted from an analog to digital signal in the IPE crate where ORCA[1] does the data read out.

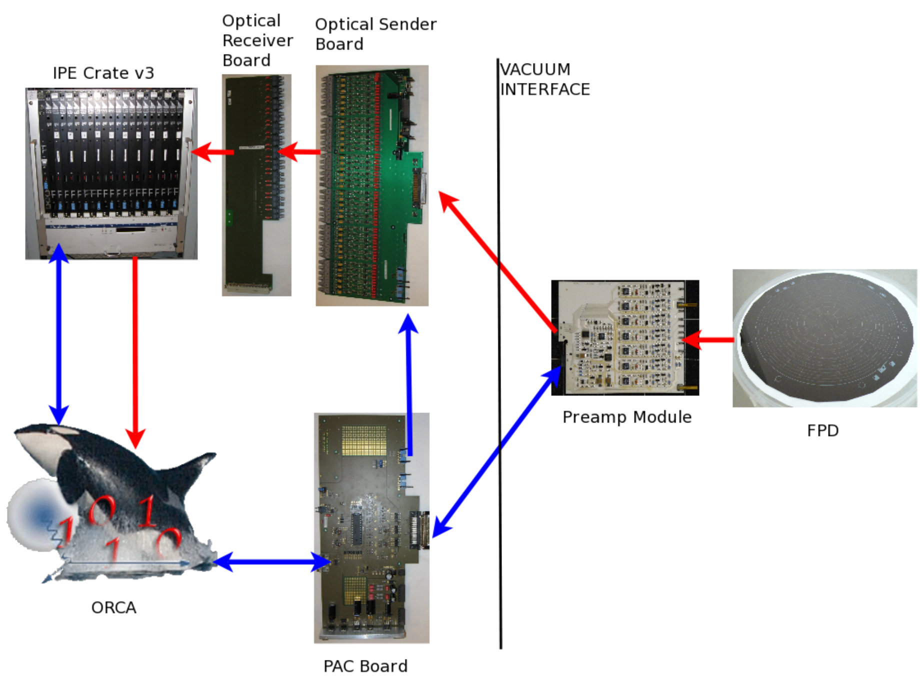

Figure 1.14-1. The electronics data and control diagram. The red arrows show the data path and the blue arrows show the control path.

The IPE group has delivered a commissioning set of electronics to CENPA. The delivery

[1]CENPA Annual Report, University of Washington (2008) p. 81.

included 24 preamp modules for a total of 148 channels, the PAC board, a single optical sender board, and two optical receiver boards. An IPE version 3 crate already resides at CENPA. This will allow us to test one quadrant of the detector at a time. After receiving the electronics Lars Petzold of the IPE group visited CENPA and helped establish operation of the electronics. Also during this time Mark Howe visited and established ORCA control of the PAC board and the programmable power supplies that are going to be used to power the detector electronics. We are currently able to select individual preamp channels for pulsing or leakage current measurement, to read the temperature of individual modules, and to select the gains on the optical sender board.

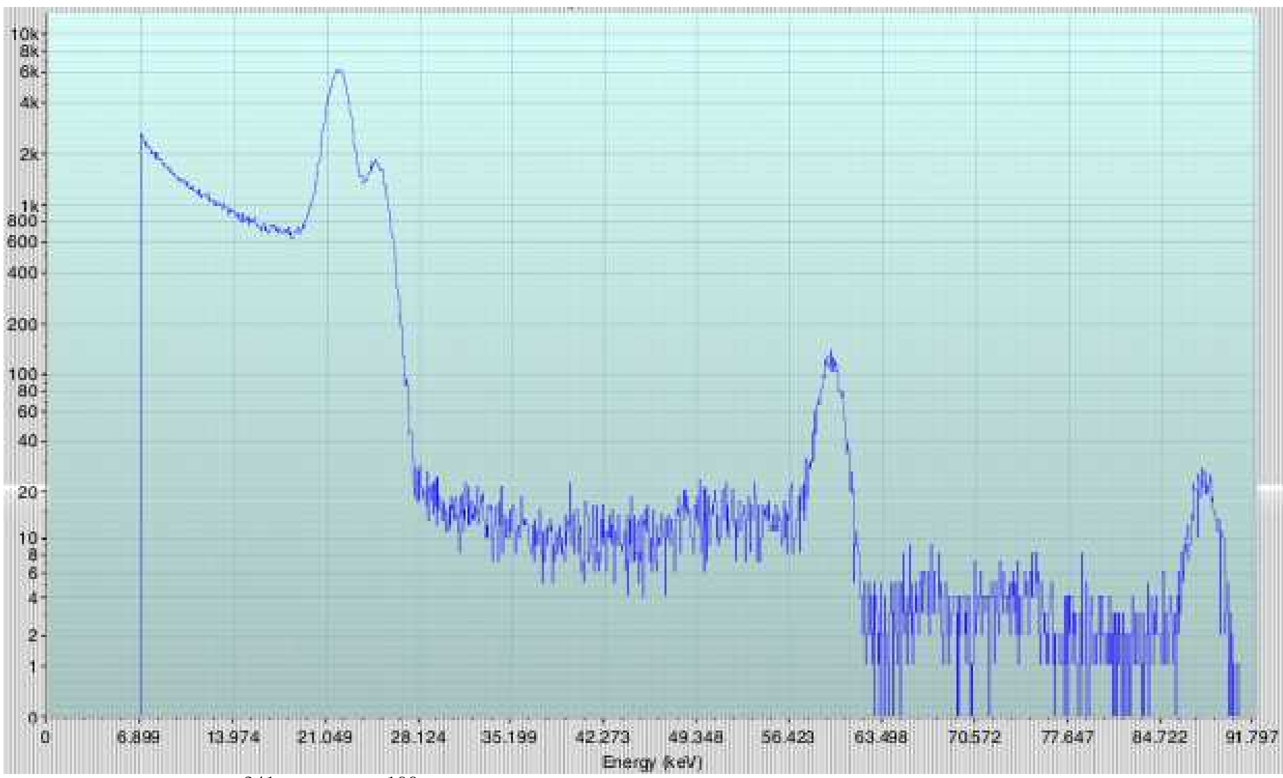

Figure 1.14-2. ^{241}Am and ^{109}Cd spectrum taken with IPE preamp module. The most energetic lines are the 59 keV and 88 keV γs from those sources

Preliminary tests of the preamplifier performance have also begun. We connected a Hamamatsu S3096 to the input of an IPE preamp module and connected the output to the IPE v3 crate for analog to digital conversion. The detector was illuminated with an 10 μC ^{241}Am and a 100 μC ^{109}Cd. The width of the 59.5 keV line of the ^{241}Am is 1.91 keV.

1.15 Preparations for KATRIN FPD commissioning

B. A. VanDevender, M. Steidl, B. L. Wall

Three KATRIN Focal-Plane Detectors (FPDs) were received at CENPA in August, 2008. The manufacturer, Canberra Belgium, verified specifications for reverse-bias leakage currents less than 100 nA/cm^2 at 20 °C before delivery (Fig. 1.15-1). All three devices were examined at UW under a microscope with a high-precision translating stage (Fig. 1.15-2). The software interface to the scope allowed mapping of all mechanical dimensions of the device. The coordinates of all 24 wafer corners, 148 pixels, guard ring and bias contact region of all three devices meet specifications well within allowed tolerances provided to Canberra. Other specifications are listed in Table 1.15-1.

The devices are currently stored in a dry nitrogen environment awaiting full characterization of their properties. They will be installed in CENPA's electron gun[1] with the front-end electronics described in this report (see Sec. 1.14). The full commissioning program will determine the optimum reverse-bias potential, leakage currents, and responses to gamma rays and electrons with energies in KATRINs signal region at the optimum bias at both room temperature and -100 °C.

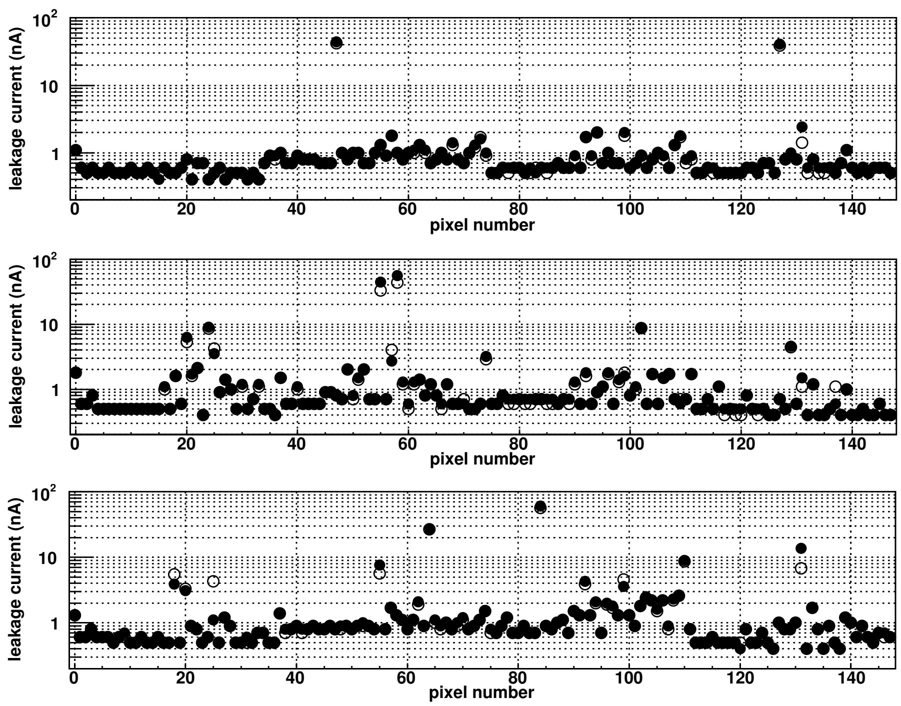

Figure 1.15-1. Room-temperature leakage current measurements on the three delivered KATRIN FPDs. Closed circles represent measurements at the recommended 120 V bias potential. Open circles represent measurements at the maximum 150 V bias potential.

[1]CENPA Annual Report, University of Washington (2008) p. 17.

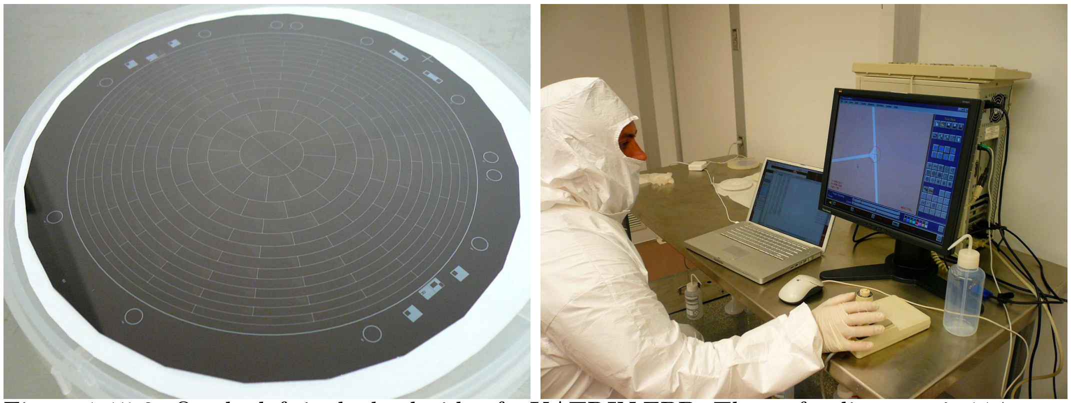

Figure 1.15-2. On the left is the back side of a KATRIN FPD. The wafer diameter is 114 mm from corner to corner. The dark gray color is due to a TiN layer intended to provide ohmic contact between the p^{++} doping and front-end electronics. The central dartboard pattern contains 148 44.1 mm^2 active pixels. A continuous guard ring surrounds the pixels. The outermost ring of TiN extends around the edge of the device so that the bias potential on the front of the detector can be supplied with contacts on the back. The picture on the right shows the inspection of an FPD. The image on the monitor is the intersection of three pixels (which appear red on the monitor). The gap between pixels (white) is 0.05 mm.

Table 1.15-1. Specifications for KATRIN FPDs

Geometry:	
bulk material	silicon
shape	regular 24-sided polygon, 114 mm corner-to-corner
thickness	500 μm
sensitive area	90 mm diameter circle
number of pixels	148
pixel area	44.1 mm^2
pixel capacitance	9.45 pF
guard ring	90–94 mm diameter circle
Doping:	
substrate	n
front (entrance) side	n^{++} unsegmented, no metallization
back side	p^{++} segmented, TiN metallization
dead layer	$<$ 150 nm
Operating Conditions:	
temperature	-100–30 °C
pressure	$< 10^{-10}$ mbar
magnetic field	$<$ 6 T
recommended bias	120 V
maximum bias	150 V

Majorana

1.16 Majorana R&D activities

J.F. Amsbaugh, T.H. Burritt, P.J. Doe, A. García, M. A. Howe* R.A. Johnson, M.G. Marino, M.L. Miller, A.W. Myers, R.G.H. Robertson, A.G. Schubert, T.D. Van Wechel, B.A. VanDevender, J.F. Wilkerson*, and D.I. Will

The Majorana Collaboration is performing R&D to demonstrate the feasibility of building a 1 tonne modular array of 86% enriched ^{76}Ge capable of searching for neutrinoless double-beta ($0\nu\beta\beta$) decay in the inverted mass hierarchy region ($\approx$30 meV). A cornerstone of the plan is the development and construction of the Majorana Demonstrator, a R&D module comprised of 30 kg of 86% enriched ^{76}Ge and 30 kg of non-enriched Ge detectors. The use of a mixture of both enriched and natural or depleted Ge has the advantages of lowering the costs in the R&D phase, accelerating the deployment schedule, and also giving Majorana an opportunity to verify that any observed peak in the $0\nu\beta\beta$ region of interest is directly associated with the presence of ^{76}Ge. The goals for the Demonstrator are:

- Show that backgrounds, at or below 1 count/tonne/year in the $0\nu\beta\beta$ decay peak 4 keV region of interest, can be achieved, a necessary condition for scaling to a 1 tonne or larger mass detector.
- Demonstrate sensitivity by testing the validity of the Klapdor-Kleingrothaus reported ^{76}Ge $0\nu\beta\beta$ observation[1].
- Show successful long-term operation of crystals in their respective environments.
- Demonstrate a cost-effective and scalable approach.

The proposed method uses the well-established technique of searching for $0\nu\beta\beta$ in high- purity Ge (HPGe) diode radiation detectors that play both roles of source and detector. These detectors will be located in specially fabricated ultra low-background, electroformed Cu cryostats. The technique is augmented with recent improvements in signal processing, detector design, and advances in controlling intrinsic and external backgrounds. Major advances in detector R&D (both laboratory and industrial) have led to the choice of p-type point-contact (PPC) detectors for the demonstrator module. These detectors offer low capacitance and excellent resolution, providing the ability to (1) tag and veto two-site background interactions via pulse shape analysis and (2) probe ultra low-energy events (E>$\approx$300 eV) to competitively search for dark matter candidates (WIMPs, axions, etc)[2].

*Now at University of North Carolina

[1]H. V. Klapdor-Kleingrothaus, I. V. Krivosheina, A. Dietz, and O. Chkvorets, Physics Letters B **586** 198 (2004).

[2]C.E. Aalseth, P.S. Barbeau, D.G. Cerdeno, Phys. Rev. Letters **101**, 251301 (2008).

1.17 Material screening with germanium detectors

J. F. Amsbaugh, K. Boddy, R. A. Johnson, M. G. Marino, A. G. Schubert, H. Simons, J. F. Wilkerson*, and D. I. Will

The MAJORANA neutrinoless double-beta decay experiment will require extremely low background rates. The MAJORANA Collaboration has a background goal of 1 count per tonne-year in the 4-keV region of interest surrounding the ^{76}Ge double-beta decay endpoint. To achieve MAJORANA background goals, materials used in the experiment must meet high radiopurity standards. Assaying raw materials at the sensitivity required for MAJORANA is costly and time consuming. A surface-level material-screening facility has been established at CENPA to prescreen materials for MAJORANA.

The CENPA material-screening facility consists of a high-purity germanium detector enclosed in a six-inch-thick lead shield. A scintillator panel was constructed and added to the system. The scintillator tags events in the germanium detectors associated with incident cosmic rays. The original lead shielding was dismantled and reconstructed from lead known to be radiologically clean. The background spectrum in the detector with and without the cosmic-ray veto is shown in Fig. 1.17-1. The facility allows materials not clean enough for MAJORANA to be identified without sending the materials to higher-sensitivity facilities. The minimum sensitivity of the facility, calculated for a massless point source 1 mm from the front face of the detector after seven days of counting, is ≈20 mBq for ^{232}Th and ^{238}U in equilibrium, and ≈30 mBq for ^{40}K.

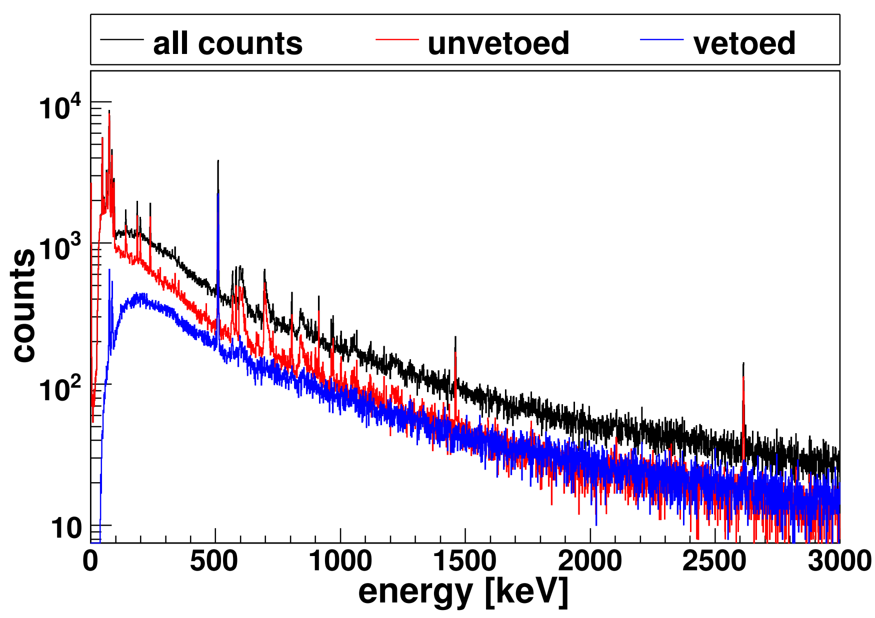

Figure 1.17-1. Background spectrum inside lead shielding in the MAJORANA lab. The full spectrum, counts tagged by the veto, and counts not tagged by the veto are shown. Data were collected for 5.6 days.

*University of North Carolina, Chapel Hill, NC

1.18 Surface-alpha measurements on HPGe detectors

T. H. Burritt, S. R. Elliott[*], V. M. Gehman[*], V. E. Guiseppe[*], R. A. Johnson, and J. F. Wilkerson[†]

A test stand for the study of surface-alpha measurements on HPGe detectors has been built and data have been collected. The goal is to understand the response of a detector to alpha particles of different incidence angles and build a more realistic background model for surface alpha decays on HPGe detectors in double-beta decay experiments. The test stand allows an alpha source to shine on the surface of an N-type HPGe detector through various collimation holes of different angles. An ^{241}Am source attached to a rotational feedthrough allows alignment of the source with a particular collimation hole via manipulation of the feedthrough. In this way, several data runs of different collimation angles can be obtained without opening up the cryostat.

Data were taken (Fig. 1.18-1) with alphas of incidence angles 0°, 30°, 45°, and 60°, with the angle defined with respect to the normal of the surface. The ^{241}Am source consists of three main alpha peaks (5388, 5443, and 5486 keV) as well as a 59.5 keV gamma that accompanies the 5486 keV alpha and results in a 4^{th} peak. The width and offset of the peaks is due to energy losses within the dead region of the detector; larger incidence angles result in wider spread and greater offset. The data are being fit using a PDF that matches the width and offset of the peaks to the dead layer of the detector. This information will be used to validate surface-alpha decay simulations and infer purity requirements.

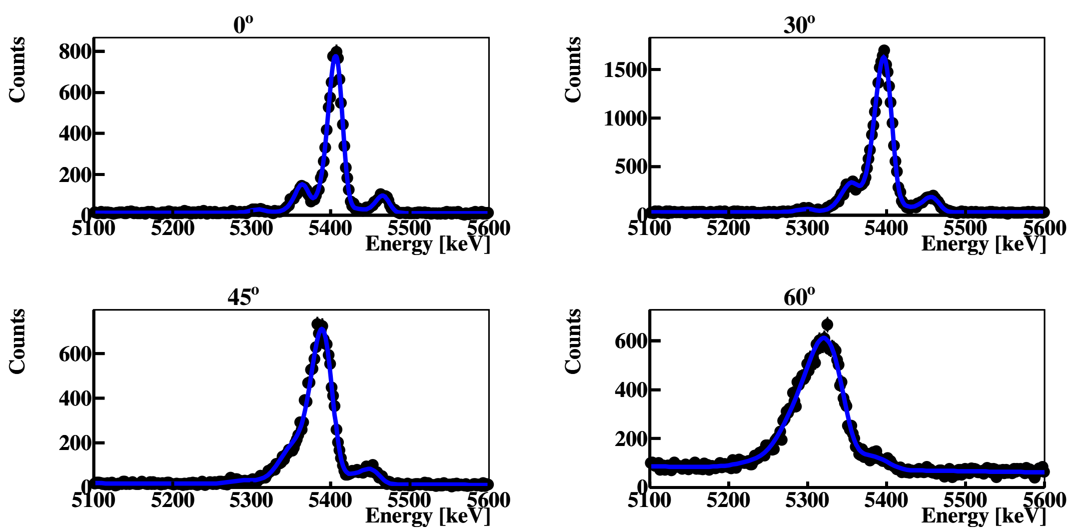

Figure 1.18-1. Alpha spectra from ^{241}Am at four different incidence angles. Alphas at larger incidence angles must travel through more dead regions of the crystal, and therefore lose more energy and are subject to more energy straggling.

[*]Los Alamos National Laboratory, Los Alamos, NM
[†]University of North Carolina, Chapel Hill, NC

1.19 Methods for deploying ultra-clean detectors

T. H. Burritt, S. R. Elliott*, V. M. Gehman*, V. E. Guiseppe* A. G. Schubert, and J. F Wilkerson†

The MAJORANA Collaboration will use an array of germanium crystals enriched in ^{76}Ge to search for neutrinoless double-beta decay. The germanium crystals will be housed in radiologically-pure copper cryostats. Several vertical strings of four or five Ge crystals will be deployed in each cryostat.

Strings for the MAJORANA experiment must be constructed from ultra-pure materials and maintain proper thermal and electrical operating conditions for Ge detectors. A preliminary design for the building block of a detector string, a detector mount, is shown in Fig. 1.19-1. The intent is to minimize the amount of material near the detector and to minimize handling of the parts during fabrication.

A test cryostat at Los Alamos National Laboratory has been used to test electrical and mechanical properties of string designs for MAJORANA. Several temperature sensors within the cryostat are used to evaluate the thermal performance. Temperature data taken while cooling the system with liquid nitrogen has been used to study the flow of heat from detector blanks and has provided information about the conduction of heat through the detector string.

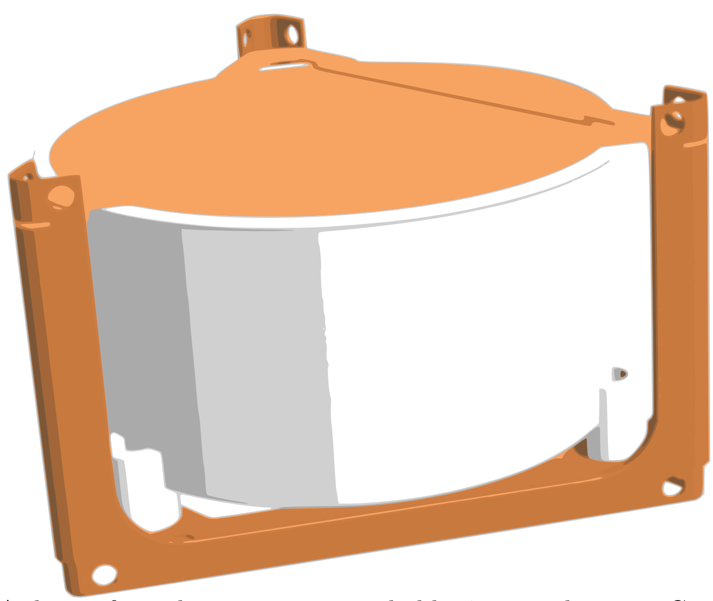

Figure 1.19-1. A design for a detector mount to hold a 70 mm diameter Ge detector. The detector is shown in grey; the detector mount is created from ultra-pure copper and small amounts of electrically-insulating material.

*Los Alamos National Laboratory, Los Alamos, NM
†University of North Carolina, Chapel Hill, NC

2 Fundamental Symmetries and Weak Interactions

Torsion Balance Experiments

2.1 Charge measurement for gravitational wave observatories

J.H. Gundlach, C.A. Hagedorn, J.L. McIver, S.E. Pollack*, S. Schlamminger, M. Turner

Electrical charges on the end masses of interferometric gravitational wave observatories are an important noise source for the planned space based gravitational wave antenna LISA, as well as for existing ground based observatories like LIGO. In both systems an interferometer compares the light travel time between two pairs of end masses. The end masses are inertial along the direction of the light and an incoming gravitational wave will alter the light travel time in one arm with respect to a second arm. For LISA and LIGO, the end masses are electrically isolated. For LISA, the isolation occurs because the end mass is freely falling inside a spacecraft which is servoed such that the mass is essentially force free. For Advanced LIGO, the end masses are suspended from insulating fused silica fibers, which have been chosen for their low mechanical loss. In both cases, fluctuating charge on the end masses can couple to conductive surfaces nearby and produce small spurious accelerations, limiting the sensitivity of the gravitational wave antenna.

We have been using our torsion balance experiment to investigate such charge fluctuations. Fig. 2.1-1 shows the geometry of the experiment. A silicon pendulum is suspended from a quartz fiber. Two copper plates are placed in the vicinity of the pendulum, and the gap between plates and pendulum can be varied from 0.05 mm to 10 mm. The angular excursion of the pendulum is measured by an autocollimator and processed by a digital feedback loop. The feedback loop creates a control voltage that is applied to either one of the larger electrodes such that the pendulum remains parallel to the copper plates. The sign of the control voltage can be selected by the user and the measured control voltage is recorded as the science signal. In order to avoid large contact potentials, all surfaces have been gold plated.

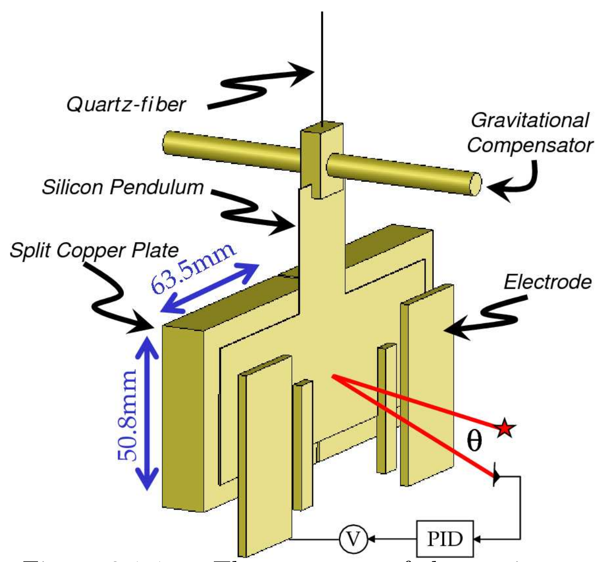

Figure 2.1-1. The geometry of the torsion balance experiment.

In the past year we have established an electrostatic model of the geometry described above. This model has been tested with measurements and a finite element analysis. The

*Presently at Rice University, Houston, Tx.

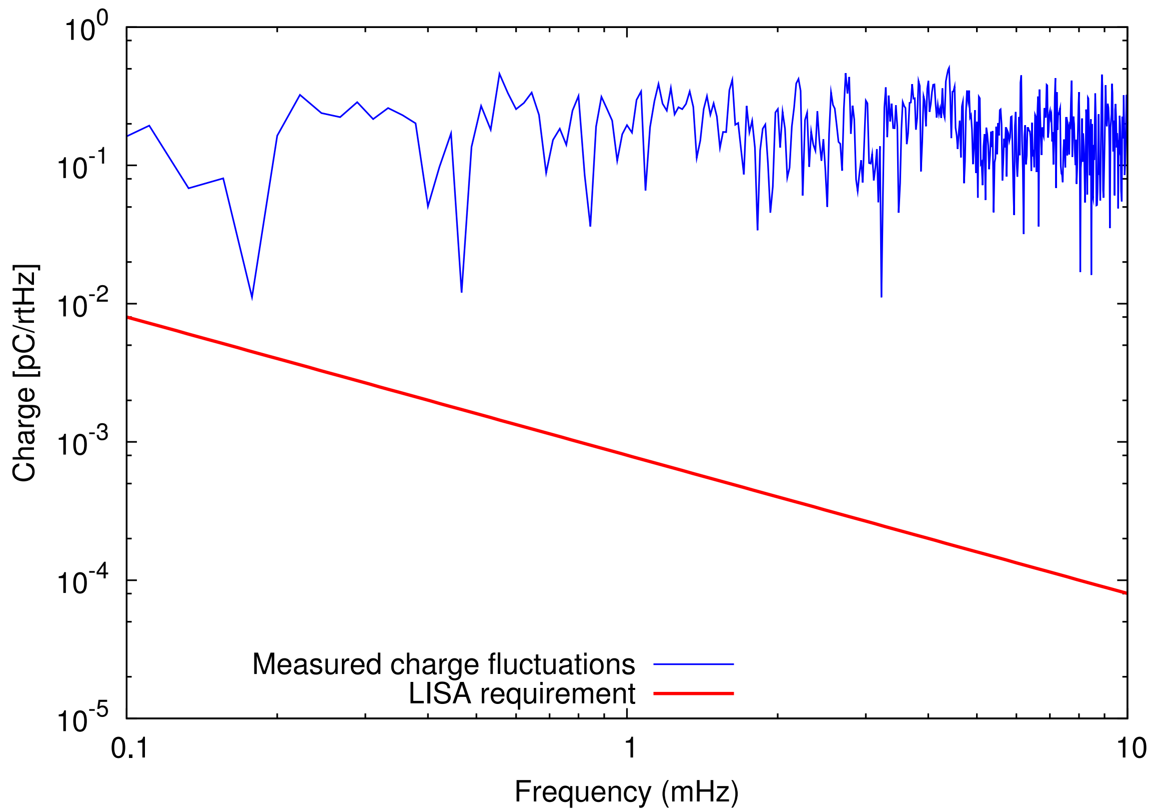

Figure 2.1-2. A preliminary measurement of the power spectral amplitude of the charge on the pendulum. The thick solid line is the LISA requirement.

model, experiment, and simulation agree within their uncertainties. We have developed a procedure to infer the charge on the pendulum by holding the pendulum parallel to the plate with a positive control voltage V_+ and then with a negative voltage V_-. The charge on the pendulum is given by $Q = C(V_+ + V_-)$, where C is the capacitance between the pendulum and one copper plate. The data acquisition software has been altered to automatically change the polarity of the feedback voltage every 20 s. The mean feedback voltage and the known capacitance C is used to calculate the charge fluctuation.

A preliminary measurement of the power spectral amplitude of the charge fluctuation is shown in Fig. 2.1-2. In the measured frequency range, the charge fluctuations appear to be white with a value of 0.2 pC/$\sqrt{\text{Hz}}$. There are several noise sources that may be contributing to the measured level of charge fluctuations; therefore, this measurement is an upper limit of the level of charge noise which may be expected for LISA. We are currently characterizing our systematics, including surface potential fluctuations on the nearby conducting surfaces, thermally activated torque noise in the quartz fiber, and seismic couplings. In addition we are preparing schemes to actively discharge the pendulum and hence reduce the noise in the system.

2.2 Progress on improved equivalence principle limits for gravitational self-energy

E.G. Adelberger, J.H. Gundlach, B.R. Heckel, S. Schlamminger, T.A. Wagner

Lunar laser ranging now makes range measurements with 1 mm uncertainty[1]. This improvement will result in better constraints on equivalence principle violations. However, an ambiguity exists in testing equivalence principle violations with the Earth-Moon system because the Earth and Moon have significant gravitational self-energy as well as different compositions. In the laboratory we test for equivalence principle violation based only on composition differences since the test bodies have insignificant gravitational self-energy. Combining the lunar laser ranging and laboratory measurements allows for separate limits on equivalence principle violations due to gravitational self-energy and composition differences.

We test for composition dependent equivalence principle violation using a rotating torsion balance. The pendulum is configured with a composition dipole based upon the differences in the Earth's and Moon's compositions. In previous measurements, our torsion balances have operated near the thermal limit imposed by the torsion fiber. However, the pendulum used for the Earth-Moon test experienced noise about a factor of 3 greater than this. The dominant noise source was traced to extremely small pressure bursts in our vacuum chamber. These pressure bursts occurred roughly once an hour. The pressure increased to about two times the base pressure of 5×10^{-5} Pa, but was pumped back down within 20 s. Extensive testing of our vacuum system led to a redesign of some of the O-ring seals. During the redesign, we took the opportunity to stiffen the central column as well, as shown in Fig. 2.2-1.

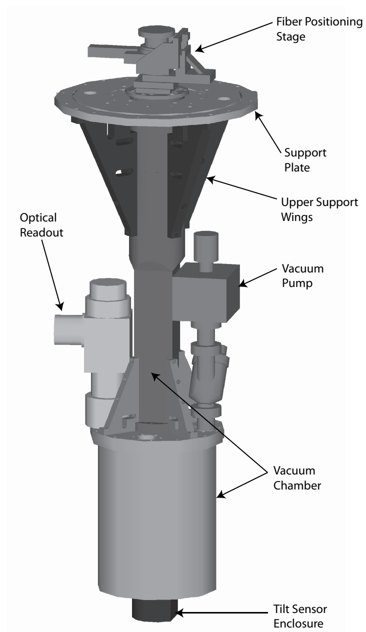

Figure 2.2-1. New design for our vacuum chamber column.

The new vacuum chamber was designed to minimize changes to our apparatus, while improving the O-ring seals and avoiding new weldments. With the redesign we improved mechanical stiffness and immunity to temperature gradients. Two sliding O-ring seals on the central column were replaced with more reliable compression O-ring seals. The column wall is a factor of six thicker, and the thickness of the rocket-wing like support fins was doubled. These changes resulted in more than an order of magnitude increase in the stiffness of the vacuum chamber column. The seal between the column and the fiber positioning stage was separated from structural support of the column. The fiber support stage rests on top of the column which extends through the fiber support plate. There is a gap between the column and fiber support stage to reduce thermal coupling. We previously determined that the top support plate was the location of the apparatus' greatest sensitivity to temperature gradients. We expect to resume taking data with the Earth-Moon test bodies in May.

[1]Battat, J. B. R., *et al.*, PASP, **121**, 29 (2008)

2.3 Continued progress toward a new sub-millimeter test of the gravitational inverse square law

J.H. Gundlach, C.A. Hagedorn, S. Schlamminger, M. D. Turner

We have continued work on a new torsion balance for a parallel plate test of the gravitational inverse square law[1,2]. Our experiment is within reach of new limits, but further characterization of systematic effects is required. We have undertaken many improvements to the apparatus and our data analysis software to increase the experiment's intrinsic sensitivity, close systematic loopholes, and more cleanly extract signals from the data stream.

Important improvements include: (1) replacement of the aluminum isolating foil with beryllium copper; (2) fabrication and installation of an improved attractor plate with significantly smaller gravitational field inhomogeneities; (3) improvements in alignment and cleaning techniques; (4) the installation of a commercial in-vacuum encoder on the attractor to supplement and, recently, replace our simple optical readout; (5) acquisition and installation of an electrically isolated data acquisition and control system for attractor-related signals; (6) installation of additional feedthroughs and cabling to further segregate signaling; (7) improved internal grounding and added optical isolation for critical feedback voltages; and (8) the fabrication and installation of new thermal insulation for the bell jar. Furthermore, intensive gravitational simulation work to both optimize our attractor design and predict expected Newtonian torques has reached improved levels of sophistication and detail.

These improvements have brought us closer to a successful measurement. The torque noise in our region of interest ($\approx$ 2-10 mHz) is $< 2 \times 10^{-14}$ N-m/$\sqrt{(\text{Hz})}$ at ≈ 50 μm pendulum-foil separation. We are able to achieve pendulum-attractor separations of 60 μm while maintaining feedback lock at an increased noise level. We anticipate releasing our first results in the coming year.

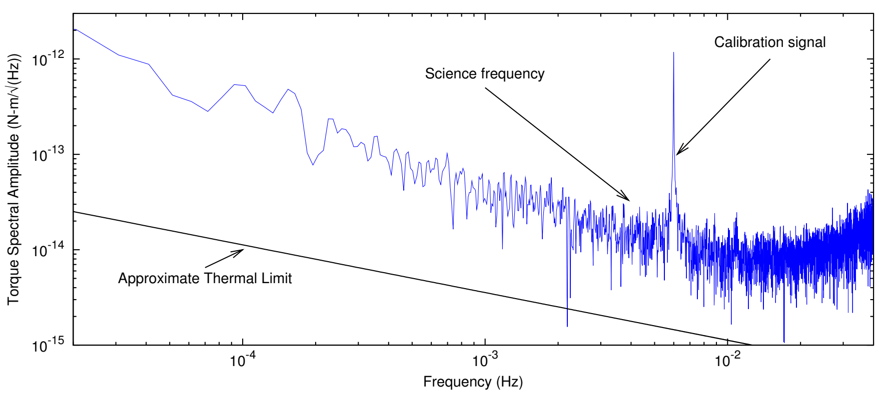

Figure 2.3-1. Torque noise performance with 50 micron pendulum-foil separation.

[1] CENPA Annual Report, University of Washington (2007) p. 40.
[2] CENPA Annual Report, University of Washington (2008) p. 33.

2.4 A cryogenic torsion balance for gravitational experiments

E. G. Adelberger, F. Fleischer and B. R. Heckel

A fundamental limiting factor for our torsion balance experiments is thermal noise. To overcome this limitation, we have started a new project aimed at the development of a torsion balance experiment operating at cryogenic temperatures. Because of its relative simplicity, its first application will be a non-rotating equivalence principle test.

We have developed a setup which allows to cool down a torsion balance to temperatures near liquid helium temperature (4.2 K). Due to the extreme sensitivity of these experiments, special consideration was given to maintaining a low level of vibrations. A two-stage pulse tube cooler made by Sumitomo (model RP-062B) has been chosen for its low-vibration characteristics, and the setup has been designed to provide vibrational isolation between the cryo-cooler and the vacuum chamber containing the torsion balance.

Fig. 2.4-1 shows a schematic cross section of the experiment. The vacuum vessel contains two thermal shields, an outer one at an intermediate temperature of $\approx 90\,\mathrm{K}$ and an inner one at $\approx 4\,\mathrm{K}$. The inner shield will hold the torsion balance, consisting of a composition dipole pendulum hanging from a thin conductive fiber. Both shields are connected to the corresponding stages of the pulse tube cooler via flexible heat links made from copper braids. Furthermore, to insure good vibrational decoupling, the cold head is supported by a separate wall mount featuring a set of three air springs with a low resonance frequency of $\approx 3\,\mathrm{Hz}$. A laser autocollimator will be used for monitoring the torsion balance's movement.

The construction of the actual experimental setup started in the fall of 2008. By the end of the report period, the structural parts, the vacuum system, the flexible heat links and the thermal shields as well as a system for montoring the temperatures of different parts using silicon diode temperature sensors were completed and assembled. The vacuum system has been successfully evacuated to pressures in the upper 10^{-7} mbar range at room temperature. The first cool-down test for setup was a success.

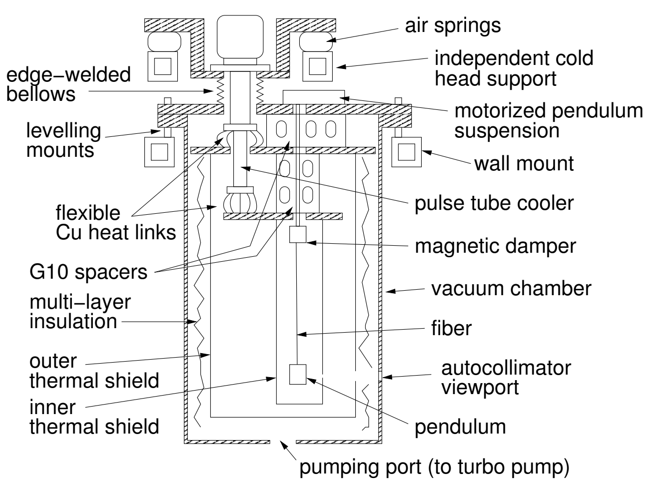

Figure 2.4-1. A schematic cross sectional view of the cryostat setup for the cryogenic torsion balance.

2.5 Wedge pendulum progress report: testing the gravitational inverse-square law

E. G. Adelberger, T. S. Cook and H. E. Swanson

Last year we reported solving our technology hurdles and were preparing to take data[1]. As it turns out we were only partially correct in our assessment. While our data collection is now nearly complete, we were forced to abandon one piece of technology due to its failure to work reliably. This past year has also been marked by the development of code to calculate torques for non-aligned geometry.

We began taking data with the Wedge pendulum in July of 2008. About a month into the process our Nanomotion motor began to exhibit erratic behavior showing large swings in temperature and ultimately losing the ability to turn in one direction. We decided it was no longer worth our time to pursue this technology and returned to our previous method of rotation, a stepper motor. Fortunately, with only minor modifications we were able to use the feedback system designed for the Nanomotion motor to run the stepper motor in lock-step with our angle encoder. While not as precise as the Nanomotion motor (by approximately a factor of 2), the fed-back stepper motor still represents an improvement in angle error of over two orders of magnitude when compared to the stepper motor run with a clock pulse (the method used to run the stepper in previous incarnation of the short range experiment).

One feature of the wedge geometry is that it allows for a nearly analytic solution for calculating torques. This solution involves a single integral over some Bessel functions which result from writing down the Green's function for a gravity-type or Yukawa-type potential in cylindrical coordinates. When the pendulum is not exactly aligned with the attractor, however, the cylindrical coordinate system is broken and the solution now requires more complicated integrals over the geometry. To calculate torques for such alignments (which is the more accurate physical description of our experiment), we developed code in C++ that runs on the Athena Cluster (see Sec. 7.5), a highly parallel computer located at CENPA, to perform the Monte Carlo integrations. Two versions of the code were developed: (1) a simple yet time consuming point-by-point integration over both attractor and pendulum and (2) an extension of the Bessel function solution that integrates the analytic solution of the attractor for each point in the offset pendulum. The Athena Cluster allows for extreme parallelization of the calculation to quickly build statistical error bars within our desired accuracy. Current testing shows perfect agreement between methods (1) and (2) (both of which agree with the analytic solution on center), with the Bessel method converging about 8 times faster.

We are now taking data, exploring changes both in separation distance and in radial alignment. We anticipate ending data taking and performing a complete analysis of the data shortly.

[1] CENPA Annual Report, University of Washington (2008) p. 28.

2.6 Progress on a torsion balance test of new spin coupled forces

E. G. Adelberger, B. R. Heckel and W. A. Terrano

The torsion balance experiment to measure spin dependent forces[1] is nearly ready for commissioning. All that remains is assembling it in the vacuum system with the torsion fiber attachments.

Since our pendulum will have large numbers of aligned spins in order to be sensitive to spin coupled forces, an essential component to the experiment is demonstrating that its magnetic couplings can be controlled.

To this end, after assembling the ring we tune the magnetizations of each individual segment. This reduces the measured peak to peak magnetic field 70 thousandths of an inch above the rings from 600 G to 30 G (Fig. 2.6-1). Housing the magnets under two layers of magnetic shielding, as in the experimental design, further reduces the measured magnetic field to ≈ 1 mG (Fig. 2.6-2). Since we are only interested in torques at 10 times the rotation frequency of the attractor, we can take the Fourier transform of these traces to get an idea of the shielding at the science signal. The torque on the pendulum depends on the product of the magnetic fields of the pendulum and attractor, and so we can get a very rough estimate of the shielding factor by comparing $5 \cdot 10^3$ G of spin contrast every 18° to a magnetic field variation of $4 \cdot 10^{-5}$ G at the same frequency outside the ring. This means we have room to see spin coupled interactions down to 10^{-16} compared to magnetic interactions. This is compatible with our experimental goal.

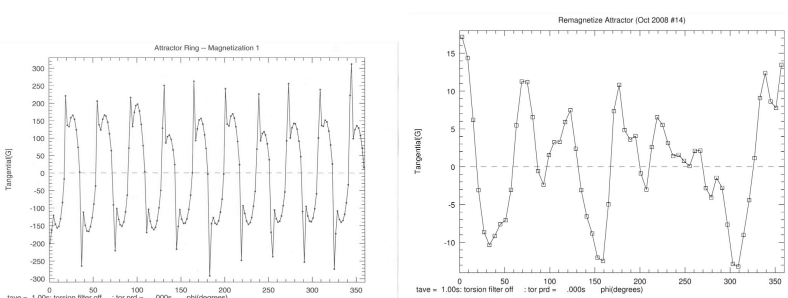

Figure 2.6-1. Left: Before tuning the Alnico magnetization. Right : After tuning

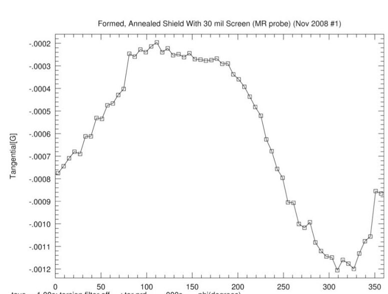

Figure 2.6-2. With magnetic shielding

[1]CENPA Annual Report, University of Washington (2007) p. 38.

2.7 Designing an equivalence principle pendulum with hydrogen rich test bodies

E. G. Adelberger, J. H. Gundlach, B. R. Heckel, S. Schlamminger, W. A. Terrano

One of the deepest puzzles of contemporary physics is the nature of Dark Matter. Despite the fact that Dark Matter appears to be around five times more prevalent than ordinary matter we have very little experimental information about its behaviour and interactions. There are limits on weak and electromagnetic point contact interactions from WIMP and axion detection experiments. Galactic rotation curves, large scale structure and CMB/BBN considerations indicate that Dark Matter interacts gravitationally with hydrogen. An interesting question then is the nature of long range interactions between dark matter and other materials. Such an additional, non-gravitational, force would appear similar to an Equivalence Principle violation, pointed in the direction of the galactic dark matter halo.

To investigate such interactions, we are gearing up for a version of the classic torsion balance tests of the Equivalence Principle with test bodies that are rich in Hydrogen. The major difficulty at this point is working with materials that have a high concentration of Hydrogen. At this time we have designed and are building a prototype that uses Ultra-High-Molecular-Weight Polyethylene. A cross section of the prototype is shown below.

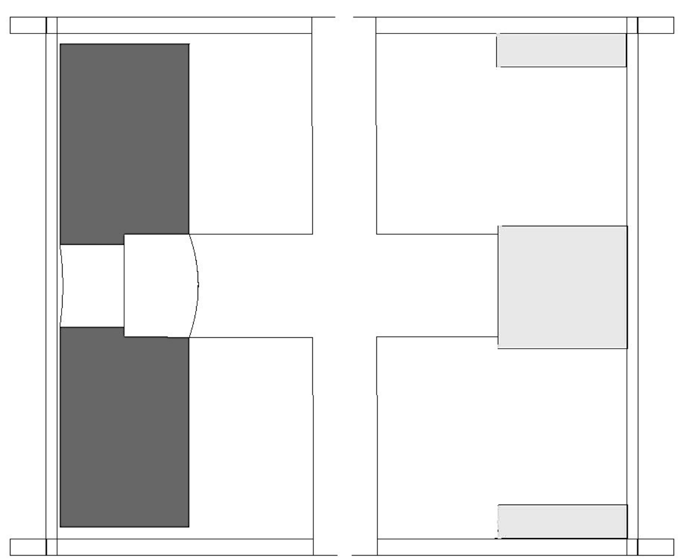

Figure 2.7-1. The Polyethylene is in dark grey, and the Aluminum test masses are in light grey. They each make up one half of a cylindrical shell. The unshaded regions are an aluminum shell that surrounds the entire pendulum for electrostatic shielding and the rods that attach the pendulum to the torsion fiber.

Weak Interactions

2.8 Production of ^{6}He to determine the e-$\overline{\nu}_e$ correlation

G. C. Harper, A. García, Z. T. Lu*, P. Muller*, R. G. H. Robertson, C. Wrede, and D. W. Zumwalt

We are planning to develop a laser trap for ^{6}He with the aim of determining the e-$\overline{\nu}_e$ correlation with unprecedented precision. We are presently building an apparatus to serve as a production target to produce an intense source (10^9 s^{-1}) of ^{6}He. We plan to use the ^{7}Li(d,^{3}He)^{6}He reaction on molten Li from a 12 MeV beam of deuterons at a current of order 10 μA from the CENPA Van de Graaff. This should allow sufficient ^{6}He production, but it is unclear how fast the ^{6}He will be transmitted to the trapping site, so we plan to test this system.

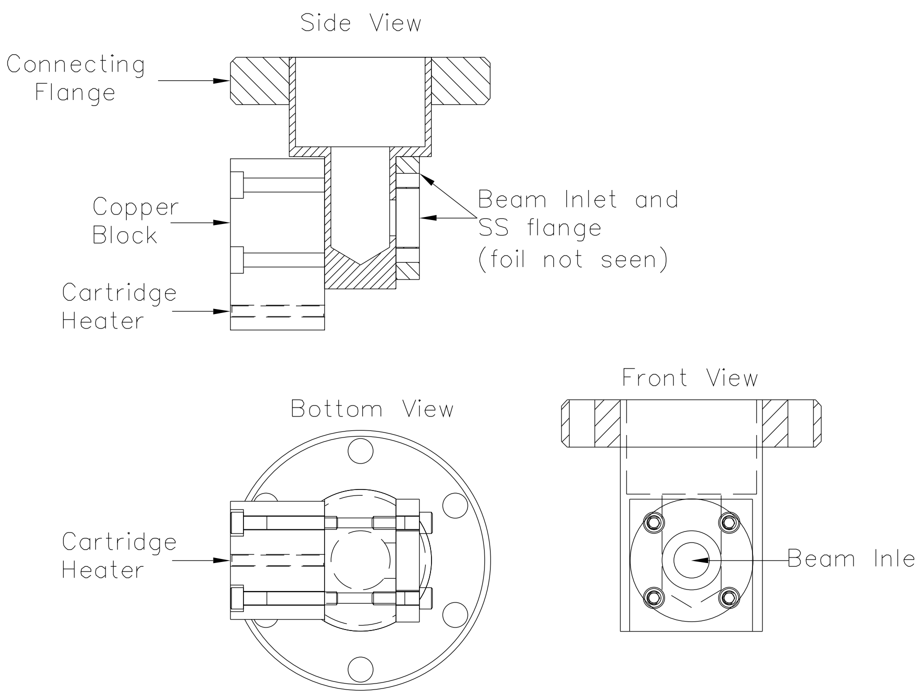

Figure 2.8-1. Lithium cup for production of ^{6}He.

We are using a cylindrical cup made of stainless steel (volume roughly 70 cm^3) to contain the molten Li. Lithium does not have any corrosive reaction with stainless steel, so it is a good material for a holding cell. The cylinder will then be partially milled flat on two sides. On one side, we will drill a hole into the cup and attach over the hole a stainless steel foil through which the deuteron beam can pass (see Fig. 2.8-1). This attachment will be made by clamping the foil onto the flat face of the cylinder using a custom Stainless Steel flange with a semi-circular ridge machined around the face of the flange. On the other flat face, a

*Physics Division, Argonne National Laboratory, Argonne, IL block of copper will be attached for use in regulating the temperature to melt or solidify the lithium. Copper is used here for its good thermal conductivity properties.

An electrical cartridge heater will be placed inside the copper block and will be controlled by a temperature regulator attached to the cup. We will also have two cooling-gas lines attached to the copper block, an inlet and an outlet. In the event of overheating, compressed air will be used to cool the copper block, and the power to the cartridge heater will be shut off. This is important because our beam current can be of order 10 μA, and so at 12 MeV we would be introducing power of order 100 W.

To isolate our apparatus thermally and electrically, we have used ceramic breaks. There are three isolators used for our design. The first is a ceramic electrical isolator used on the electrical feed-through port, which prevents electrical noise from interfering with the reading on the temperature controller. The other two are for both thermal and electrical isolation. The primary insulator is attached to the main outlet of the cup, which will then transfer the ^{6}He into a turbopump and into an experimental area. The other two insulators form a break in the two cooling lines.

Initial testing will address concerns regarding the integrity of the stainless steel foil after the molten lithium cools. If the foil breaks, we have alternative (more complicated) designs that we will consider.

2.9 Measurement of the neutron beta asymmetry with ultracold neutrons

A. García, S. Hoedl, A. L. Sallaska, S. K. L. Sjue*, C. Wrede, and UCNA collaboration†

Precision measurements of the neutron half life and β asymmetry parameter A_0 together could provide a value for the CKM quark-mixing matrix-element V_{ud} that is competitive with, and complementary to, the most precise value that is determined from superallowed $0^+ \rightarrow 0^+$ β decays.

Traditionally, measurements of A_0 have been made using polarized cold neutrons ($E_{CN} <$ 25 meV) that include substantial systematic uncertainties related to their polarization and self-induced background via activation of the apparatus. To reduce these uncertainties the UCNA collaboration made the first measurement of A_0 using polarized *ultra*-cold neutrons ($E_{UCN} <$ 340 neV) at the Los Alamos Neutron Science Center in 2006 and 2007. Results of these limited post-commissioning measurements were published in 2009 and yielded $A_0 = -0.1138(0.0046)_{stat}(0.0021)_{syst}$, in agreement with the world average of $A_0 = -0.1173(0.0013)$ from the Particle Data Group that is based entirely on cold-neutron measurements.

In 2008 the efforts of the UCNA collaboration were focused on reducing both the statistical and systematic uncertainties to achieve a 1% measurement of A_0. Statistical uncertainties have been reduced by a factor of ≈ 5 by increasing the proton production-beam current, improving neutron transport from the UCN source to the UCNA spectrometer, and running for a much longer period of time. Systematic uncertainties have been improved by a factor of ≈ 4 by carrying out several dedicated systematic studies. For example, Monte Carlo studies of electron backscattering and angle-dependent energy loss have been tested by running in different geometries, depolarization studies have been refined, and the energy calibration has been improved by using new calibration sources (section 2.11). Based on these improvements we expect to report a sub-1% measurement of A_0 for 2008 (see Table 2.9-1), with a goal of 0.3% for the future.

	2007	2008
Statistics	4.0%	$<$ 0.8%
Polarization	1.3%	$<$ 0.4%
Energy calibration	1.5%	0.3%
Angle effects	0.5%	0.2%
Backscattering	0.4%	0.2%
Total	4.5%	$<$ 1.0%

Table 2.9-1. Uncertainties contributing to the measurement of A_0 by the UCNA collaboration in 2007 and 2008. The 2008 numbers are preliminary.

*Present address: TRIUMF, Vancouver, BC, Canada

†A. Saunders, A. Young spokespersons; the collaboration is formed by approximately 30 scientists from Caltech, Duke Univ., Idaho State Univ., Univ. of Kentucky, Los Alamos National Lab., North Carolina State Univ., Texas A&M Univ., Virginia Tech, Univ. of Washington and Univ. of Winnipeg.

2.10 Characterization of ultracold neutron detectors for use in the UCNA experiment at LANL: conclusions

A. García, S. A. Hoedl, and A. L. Sallaska

We have fabricated ultracold neutron (UCN) detectors that consist of silicon charged particle detectors coupled with thin nickel foils coated with either natural LiF or ^{10}B implanted into vanadium. The foils convert neutrons into energetic, charged particles which readily produce measurable signals in silicon detectors. The detectors were tested with a gravitational spectrometer at the Institut Laue-Langevin, and both detectors and experimental setup have previously been described in detail[1]. The central problem is that neutrons will only be detected if they penetrate the surface (or surface window) of the detector. This will occur if the velocity of the UCN is greater than a "cutoff velocity," defined by the effective potential barrier of the foil.

The analysis to determine the values of the cutoff velocities for the foils has concluded and has been accepted for publication[2]. Because of the availability of the Athena cluster (see Sec. 7.5), the Monte Carlo simulation portion of the analysis was extended to include a more accurate treatment of the finite implantation distribution of ^{10}B implanted into vanadium, as well as widening the scope of systematic error checks in order to fix simulation parameters accurately. The vast extent of the parameter space probed would not have been possible without access to the cluster. The minimum detection cutoff velocities (effective potentials) were determined to be 309$\pm$17 cm/s (49.8$\pm$2.7 neV) for LiF and 367$\pm$39 cm/s (70.3$\pm$7.5 neV) for ^{10}B in vanadium. Although the result for LiF is consistent with expectations, the result for ^{10}B in vanadium is significantly higher. We interpret this discrepancy as due to contamination. We also show that while a thicker foil is more efficient for UCN detection, a thinner foil is more suitable for determining the cutoff velocity.

[1] CENPA Annual Report, University of Washington (2007) p. 50

[2] 10.1016/j.nima.2009.02.014

2.11 Development of a ^{114m}In calibration source for the UCNA experiment

A. García, G. C. Harper, A. Palmer, D. I. Will, C. Wrede, and UCNA collaboration

Uncertainties in detector response and nonlinearity contributed the largest systematic uncertainty (1.5%) to the 2007 measurement of A_0 by the UCNA collaboration (section 2.9). A goal of the 2008 measurements was to reduce the total uncertainty in A_0 to 1%, which required a substantial improvement in the energy calibration. The 2007 calibration relied on conversion electrons from ^{113}Sn and ^{207}Bi sources, which provided good calibration points for the high-energy portion of the neutron β-decay spectra ($E_\beta > 400$ keV), but a low-energy source was not available. The scarce availability of commercial calibration sources that produce intense low-energy conversion-electron lines suitable for detector calibrations of this sort prompted us to develop a ^{114m}In calibration source ($E_\beta < 200$ keV) at CENPA in collaboration with North Carolina State University (NCSU).

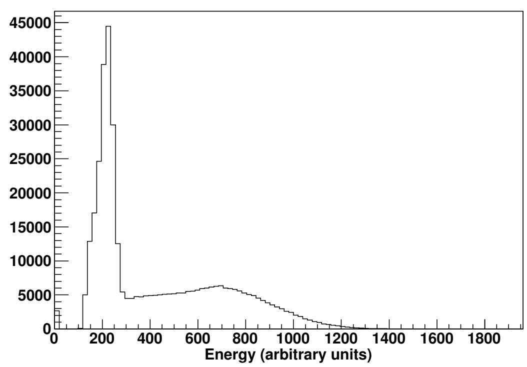

Figure 2.11-1. Raw energy spectrum of ^{114m}In source measured with UCNA scintillator detector. The peak corresponds to conversion electrons from the decay of ^{114m}In to ^{114g}In and the continuum is from the subsequent β decay of ^{114g}In to ^{114}Sn.

The general procedure was to prepare samples containing ^{113}In at CENPA and ship them to NCSU for irradiation in the PULSTAR research reactor to produce ^{114m}In ($T_{1/2} = 50$ days) via the (n, γ) reaction. A sample of ^{113}In was initially prepared by vacuum evaporation of natural indium (4.3% ^{113}In, 95.7% ^{115}In) onto a thin Kapton substrate and irradiated to produce ^{114m}In successfully. However, evidence for the oxidation and migration of the exposed indium during irradiation was observed afterwards. Attempts to encapsulate the evaporated In between evaporated layers of other elements in the next iteration of source development improved the situation, but showed that migration was still possible. This prompted us to prepare ^{113}In samples via ion implantation on the low-energy beam line of CENPA's tandem Van de Graaff instead. A 100 nA, ^{113}In^{16}O$^-$ molecular ion beam was mass selected with a 90° magnet, accelerated to 45 keV, and magnetically rastered over a 3 mm collimator to implant a 3 mm diameter, 5 μg/cm^2 sample of ^{113}In in a thin aluminized-mylar substrate. This sample was irradiated and used in December of 2008 to calibrate the UCNA scintillators. Subsequent analysis of the acquired spectra has shown that the source fabrication was successful. The ^{114m}In spectra will be used with spectra from other sources to improve the energy-calibration uncertainties in A_0 to $\approx 0.3\%$ for the 2008 runs.

2.12 Parity non-conserving neutron spin rotation experiment

C. Bass*, K. Gan†, B. R. Heckel, D. Luo‡, D. Markoff§, H. P. Mumm*, J. Nico*, A. Opper†, W. M. Snow‡, and H. E. Swanson

The parity non-conserving (PNC) neutron spin rotation experiment[1] was completed in June, 2008. The apparatus was subsequently removed from the NIST beam line and shipped to Indiana University. The experiment ran for 3 reactor cycles or about 106 calendar days. Near the end of the last cycle a coupling on the pump shaft broke and we were no longer able to transfer liquid Helium between target chambers. We decided against making a repair and instead continued to investigate systematics until the end of the cycle using cold Helium and Nitrogen gases.

The hold time for liquid Helium in the targets was 8 hours which determined the length of each run. We started the analysis phase by reviewing the entire data set and discarded data where target chambers failed to completely fill, the ion chamber showed signs of sparking, or there were abrupt changes in residual magnetic fields. The surviving data set amounted to 21 days of live running.

The weak interaction produces small rotations of the neutron spins as they pass through liquid Helium targets. The approximately 100 μGauss residual field produces a much larger precession but the design of the experiment makes the measured PNC angle relatively insensitive to this field. Periodically throughout the run set a known angle was applied to the polarized neutrons and the response of the apparatus was measured. This calibration turned out to be important in maintaining the precision angle measuring capabilities of the apparatus as well as its insensitivity to various systematic effects. Slow drifting of the residual field however can be a significant source of systematic error. To reduce the effects of varying fields we employ two independent strategies. The first of these uses linear regression on the data in each run where the angle is then determined from the residuals. This analysis is being carried out at NIST. The second uses a sliding filter (see Sec. 7.7) applied to sequential data that removes any linear or quadratic dependence prior to obtaining the angle. This later method has been part of the analysis effort at CENPA. Both of these should give similar results and comparing them will contribute to our understanding of the drift systematic.

We searched the surviving data set for any significant correlations between PNC precession angle and target Helium levels, residual magnetic fields, detector segments, or neutron velocity and none have been found. Preliminary results show no resolved angle and that we are limited by statistical errors consistent with neutron shot noise.

*NIST Center for Neutron Research, 100 Bureau Drive, Stop 8461, Gaithersburg, MD 20899-8461

†The George Washington University, Department of Physics, Corcoran 105, 725 21st St, NW, Washington, DC 47408

‡Department of Physics, Indiana University Cyclotron facility, 2401 Milo B Sampson Land, Bloomington, IN 47408

§North Carolina State University, TUNL, Raleigh, NC 27695

[1] CENPA Annual Report, University of Washington (2003) p. 5.

2.13 Permanent electric dipole moment of atomic mercury

B. Heckel, E. N. Fortson, and T. Loftus

Atomic EDM experiments offer perhaps the most sensitive probe of CP violation in Supersymmetry and other theories of physics beyond the Standard Model, and our measurements of the ^{199}Hg EDM over the years have achieved the most precise EDM limit on any system. Our previous experiment[1], which used a frequency-quadrupled laser diode on the 254 nm mercury absorption line to orient the ^{199}Hg nuclear spins, yielded an upper bound on the EDM of $|d(^{199}\mathrm{Hg})| < 2.1 \times 10^{-28} e\,\mathrm{cm}$ (95% confidence level). The leading theoretical extension to the Standard Model, supersymmetry (SUSY), is expected to generate a ^{199}Hg EDM comparable to our experimental limit. By increasing the precision of our result, we can provide important information about the model parameter space of SUSY and other theories. Since the Standard Model itself does not generate an EDM of detectable size, an actual observation of an EDM would be proof of some form of new physics.

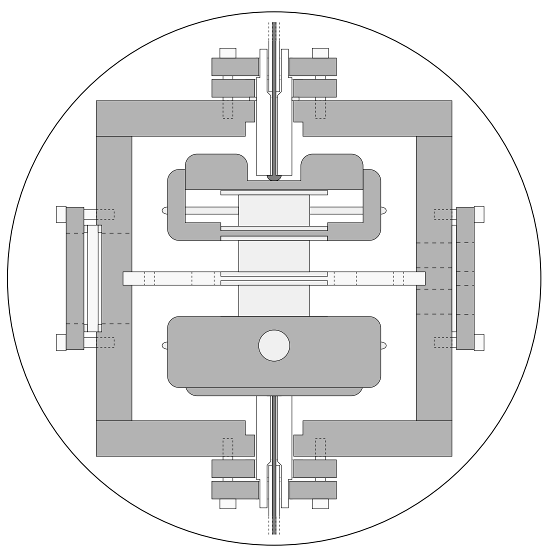

Figure 2.13-1. Cutaway view of the EDM cell-holding vessel. High voltage ($\pm$ 10 kV) is applied to the middle two cells with the ground plane in the center, so that the electric field is opposite in the two cells. The outer two cells are enclosed in the HV electrodes (with light access holes as shown here for the bottommost cell), and are at zero electric field. A uniform magnetic field is applied in the vertical direction.

In the past year, we have completed the data acquisition and analysis of an improved ^{199}Hg EDM experiment. We began with a study of the spin relaxation in our vapor cells,

[1] M. V. Romalis, *et al.*, Phys. Rev. Lett. **86**, 2505 (2001).

which led us to construct new cells that on average have 1.5 times longer spin coherence times. However, the main improvement to the experiment was the construction of an apparatus that incorporates a stack of four vapor cells (see Fig. 2.13-1). Previous versions of the experiment compared the spin precession frequency between two vapor cells, where the cells are in a common magnetic field and oppositely directed electric fields. In the current experiment the two additional cells are at zero electric field and are used as magnetometers above and below the EDM sensitive cells. They help to improve our statistical sensitivity by allowing magnetic field gradient noise cancellation, and they are also used to cancel out possible magnetic systematic effects. After spending considerable time and effort investigating systematic effects, we have recently published a new result[2] for the EDM of ^{199}Hg: $|d(^{199}\mathrm{Hg})| < 3.1 \times 10^{-29} e\,\mathrm{cm}$ (95% confidence level), a seven-fold improvement in the upper limit on the EDM of ^{199}Hg.

We have also investigated a linear Stark interference effect on the 254 nm transition we use to optically pump and probe the spin precession of ^{199}Hg. The effect can lead to a fractional change in the absorptivity that is linear in a static electric field $\mathbf{E}_S$. Our initial measurement of this tiny effect has given a preliminary result, $(3.1 \pm 3.2_{\mathrm{stat.}} \times 10^{-9}\ \ \mathbf{E}_S(\mathrm{kV/cm})^{-1})$, that is very close to the calculated size, and we plan to complete the measurement before undertaking new EDM data. Understanding this effect is important to the ^{199}Hg EDM measurement because any effect linear in applied electric field can easily lead to a systematic that might mimic an EDM. Also, agreement between the measured and calculated effect verifies part of the atomic theory that relates the ^{199}Hg atomic EDM to an underlying CP violating theory.

[2] W. C. Griffith, *et al.*, Phys. Rev. Lett. **102**, 101601 (2009).

2.14 The APOLLO lunar laser ranging project progress report

E. G. Adelberger, J. B. R. Battat*, C. D. Hoyle†, R. J. McMillan‡, E. L. Michelsen§, T. W. Murphy, Jr.§, C. W. Stubbs¶, and H. E. Swanson

The Apache Point Observatory Lunar Laser-ranging Operation (APOLLO) is a lunar ranging experiment designed to achieve 1 mm range precision to further probe the nature of gravity. After two years of operation we consistently observe photon return rates an order of magnitude higher than other stations. APOLLO is installed on the 3.5 m astronomical telescope at the Apache Point Observatory in southern New Mexico at an altitude of 2780 m. A detailed description of the apparatus can be found in Murphy *et al.* (2008)[1]. We are typically allocated 8-10 one-hour slots of telescope time per lunar month which provides a few dozen normal point measurements for each of the reflectors. The goal is to achieve uniform coverage of the lunar-phase angle. For each one-hour session we perform a laser warm-up, acquire a nearby star to correct the pointing, move the telescope to the desired reflector position on the moon and do a small raster search if necessary. We typically have time for several rounds among the reflectors.

The excellent atmospheric conditions at the site occasionally allows us to detect multiple photons per shot. Table 2.14-1 shows some of our recent record results.

Reflector	Date	Laser Shots	Photons detected (× prev. record)	Photons/minute (× prev. record)	Phot/shot
Apollo 11	2008-10-17	5000	4497 (26×)	1079 (65×)	0.90
Apollo 14	2008-10-17	5000	7606 (36×)	1825 (69×)	1.52
Apollo 15	2008-10-17	5000	15730 (26×)	3775 (67×)	3.15
Lunokhod 2	2008-09-22	5000	750 (11×)	180 (31×)	0.15

Table 2.14-1. Summary of APOLLO record runs

Roughly one-third of scheduled ranging nights are lost to weather issues (e.g., precipitation, clouds, high winds, or humidity). When APOLLO does operate we have an overall success rate of 70% but that has been steadily increasing. If we look at the distribution of uncertainties obtained by combining all normal points from a single retro-reflector array on a single night the median uncertainty is 1.8 mm for the entire data set and 1.1 mm for more recent data. As far as statistical errors are concerned, APOLLO seems to be approaching its design goal of 1 mm precision.

*Massachusetts Institute of Technology, Cambridge, MA, USA
†Humboldt State University, Arcata, CA, USA
‡Apache Point Observatory, Sunspot, NM, USA
§University of California, San Diego, LaJolla, CA, USA
¶Harvard University, Cambridge, MA, USA

[1]Murphy, T. W., Adelberger, E.G., Battat, J. B. R., Carey, L. N., Hoyle, C. D., LeBlanc, P., Michelsen, E. L., Nordtvedt, K., Orin, A. E., Strasburg, J. D., Stubbs, C. W., Swanson, H. E., and Williams, E., The Apache Point Observatory Lunar Laser-ranging Operation: Instrument Description and First Detections, Publications of the Astronomical Society of the Pacific, **120**, 2037, (2008)

Quantum Optics

2.15 Progress on a test of quantum nonlocal communication

J. G. Cramer

The question we have been investigating is whether quantum nonlocality is the private domain of Nature, as is generally assumed by the physics community, or whether in special circumstances it can be used to send signals from one observer to another. With the aid of generous private contributions and some use of CENPA resources, we have continued the work on this test of nonlocal quantum communication reported in the past two years[1,2]. The experiment, described in those references, employs a high power argon-ion laser operating in the ultraviolet at 351 nm to pump nonlinear crystals (BBO or $LiIO_3$) to produce pairs of momentum-entangled photons, on which measurements are subsequently performed. The initial version of the experiment was temporarily assembled in the UW Laser Physics Facility beginning in late January, 2007. In September, 2007, when a laser table became available in a more permanent laboratory location, the experiment was moved two doors down the hall to Room B055 of the Physics-Astronomy Building, where it presently resides.

The tests performed in the past year indicate that the efficiency is extremely low for producing pairs of entangled photons with the present argon-ion pump laser and the nonlinear crystals (BBO and lithium iodate) that have been used so far. With very few entangled photon pairs in the presence of large background noise, it is now clear that the coincidence-free tests that were envisioned, based on previous experiments of Dopfer and the Shih group, are not possible.

However, there appears to be a way of making the production of entangled photon pairs much more efficient by using “periodically poled” nonlinear crystals. Such crystals have only become commercially available in the past two years. In previously-used nonlinear crystal there is a “walk-out” phenomenon that limits the distance within the crystal over which phase matching holds, so that entangled pairs can be efficiently produced by down-conversion. However, nonlinear crystals like lithium niobiate have very large nonlinear coefficients and are also ferroelectric, with a large electric dipole moment. By using a large pulsed electric field, one can“write” on such crystals to change the orientation of the local dipole moment over small distances (a few tens of wavelengths) periodically along the pump direction through the crystal, so that the phase drift periodically reverses and cancels out as the pump radiation progresses through the crystal. This is called “periodic poling”. With this kind of crystal, the walk-out is suppressed, and one can use very long crystals that efficiently produce entangled pairs of photons over their entire length. The group of Anton Zeilinger in Vienna has used periodically polled crystals more than 25 mm long to get millions of entangled photon pairs per second. In the coming year we will obtain one or more of these crystals and will re-design the nonlocal communication test around this new technology.

[1] CENPA Annual Report, University of Washington (2007) p. 52.
[2] CENPA Annual Report, University of Washington (2008) p. 42.

3 Axion Searches

3.1 First results from the "axion" torsion-balance experiment

E. G. Adelberger, F. Fleischer, B. R. Heckel, and S. A. Hoedl

Our torsion pendulum search for an axion-like particle offers a significant improvement over the most recent such measurement[1]. The axion is the result of the hypothesized Peccei-Quinn symmetry and is a favored cold dark matter candidate. Its mass is constrained by the known flat geometry of the universe to be heavier than 1 μeV, and is constrained by the neutrino flux from SN1987A to be lighter than 10000 μeV.[2] Note that microwave cavity searches probe for light axions ($m_a \sim 1\mu$eV) and have sufficient sensitivity to see the expected cosmological axion flux[3]. A torsion-pendulum based search is possible because the axion mediates a macroscopic pseudo-scalar potential ($\propto \Theta_{QCD}$) between polarized and unpolarized fermions. By observing the motion of a planar torsion pendulum (source of unpolarized fermions) positioned near the pole faces of an energized ferromagnet, we can observe such a force. Note, however, that given the experimental limit $\Theta_{QCD} < 10^{-9}$, our apparatus will not be sensitive to either the DSFZ or KSVZ axion models.

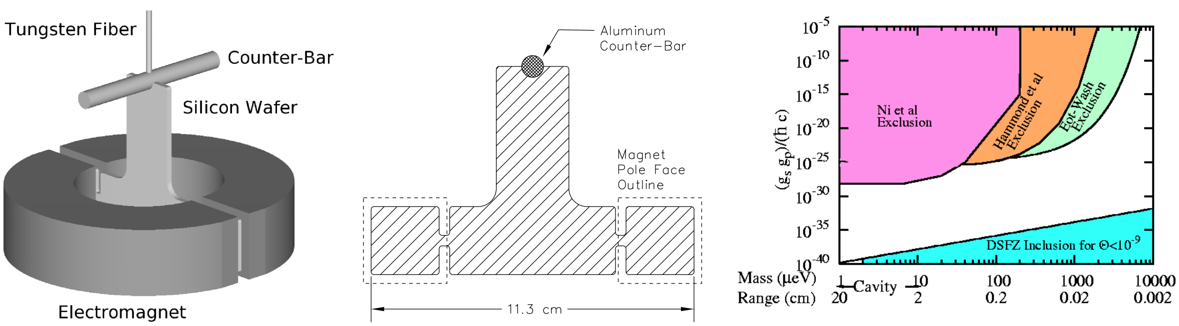

Figure 3.1-1. A scale diagram of one of our pendulums positioned in between the magnet pole faces; A face-on view of the pendulum; Our exclusion bounds compared with recent experimental searches and the expected coupling for $\Theta_{QCD} < 10^{-9}$.

In the past year, we have made progress to mitigate the dominant systematic errors associated with operating the pendulum in a strong magnetic field. We have now constructed, and are using, a mechanism which should be able to coat the pendulum with a uniform layer of terbium in a controlled, repeatable and uniform manner. We expect the coating will be uniform to within 0.5% over the full surface of the pendulum. Terbium is strongly paramagnetic, and thus, this coating will compensate for the slight diamagnetism of the silicon and minimize the pendulum's magnetic susceptibility. At present, assuming statistical errors will be the limiting factor, the apparatus puts a limit on a macroscopic parity and time violating force which is 100 trillion times more restrictive than Hammond *et al.* for an axion mass of 2 meV.

[1] G. D. Hammond *et al.*, Phys. Rev. Lett. **98**, 081101 (2007).
[2] G. Raffelt hep-ph/0611350
[3] L. D. Duffy *et al.*, Phys. Rev. D **74**, 012006 (2006).

3.2 The Axion Dark-Matter Experiment at CENPA: the phase II upgrade

M. Hotz, L. Rosenberg, G. Rybka

Our group's focus is experimental research in dark matter and our main activity is the Axion Dark Matter eXperiment (ADMX), search for axions that would make up most of the matter in our Milky Way Halo. In early 2008 this experiment completed the first phase of a major upgrade path (the "Phase I Upgrade") that increases the experiment sensitivity to allow the detection of even the more pessimistically-coupled axion variants. Cold commissioning on this first upgrade phase transitioned on April 1, 2008 into production data-taking. At the end of this current run currently targeted for fall 2009 the experiment will begin the second phase of the project upgrade (the "Phase II Upgrade") to further improve sensitivity. This final phase is the so-called "ultimate experiment". Early in Phase II construction the experiment will move to CENPA at the University of Washington (UW).

Introduction

Cosmologists have converged on a "standard model" of cosmology which successfully unifies a wide array of diverse observational constraints but requires the existence of two exotic new forms of matter and energy. In particular, the matter density of the Universe, the material in the Universe that clusters gravitationally, appears to be dominated by some form of non-baryonic "dark matter," and the energy density, the material uniformly distributed through the universe, is dominated by a new form of vacuum energy with negative pressure, dubbed "dark energy". 96% of the mass and energy of the Universe is "dark" (unseen) and cannot be accommodated by the Standard Model of Particle Physics. Therefore dramatic new physics must exist in order to reconcile all observations.

The case for a large non-baryonic component of dark matter continues to be strengthened by the ongoing developments in experimental cosmology. A prime Cold Dark Matter (CDM) candidate is the axion, which arises from an elegant and minimal extension of the Standard Model that enforces Strong-CP conservation. These dark-matter axions have mass in the approximate window 10^{-6} to 10^{-3} eV, constrained by overclosure of the universe on the low-mass end and excessively large axion couplings to normal matter and radiation at the high-mass end. Dark matter axions, once thought to be 'invisible' due to their extraordinarily weak couplings to normal matter and radiation, can be detected by their conversion into a feeble microwave signal in the presence of a strong magnetic field, resonantly enhanced by a high-Q electromagnetic cavity. First-generation experiments in the late 1980's established the feasibility of this technique and identified key technologies and challenges, thus preparing the way for the Axion Dark Matter eXperiment (ADMX), a large-scale effort operating since 1996. It was this detector where the sensitivity required to detect "KSVZ" axions, one of two classes of benchmark models, was reached at plausible axion masses for the first time.

This ADMX RF cavity axion search is a spectral-analysis problem, for which low-noise amplification is the key technology. Several years ago, John Clarke's group at UC Berkeley achieved a breakthrough in making dc Superconducting Quantum Interference Devices (SQUIDs, a type of quantum-electronics device), which can operate as high-gain, low-noise amplifiers into the GHz range. With measured SQUID noise temperatures of lower than

100 mK, compared with 1.5 K for Heterojunction Field-Effect Transistor (HFET) amplifiers, we launched a “Phase I Upgrade” to ADMX (the Phase I hardware replaces HFET amplifiers with SQUIDs) and are planning a subsequent “Phase II Upgrade” (the Phase II hardware adds dilution refrigerator cooling) to be sited at CENPA at the University of Washington (UW). The Phase II upgrade allows us to carry out a much more sensitive experiment. Ultimately we will conduct the search for halo axions with sensitivity to detect the generic, more weaker-coupled “DFSZ” axion, a particularly attractive and generic type, even should they constitute a minority fraction of our Milky Way CDM halo.

Early last year, ADMX finished constructing the Phase I upgrade and started taking data at the present experiment site at Lawerence Livermore National Laboratory (LLNL). The University of Washington participation was absolutely crucial to the success of the Upgrade. The overwhelming majority of ADMX operations and analysis personnel are from the University of Washington. The University of Washington hosts the ADMX data repository and analysis computing resources. University of Washington technicians machine parts and order pieces for ADMX. The Phase I upgrade is the thesis project of University of Washington Ph. D. student Michael Hotz, and University of Washington postdoc Gray Rybka generated limits over our first target bandwidth.

After 18 months of data-taking at LLNL, where we will search for axions having masses inaccessible to the earlier round of experiments and with coupling sensitivity towards the upper level of plausible axion couplings, the ADMX experiment will move to CENPA at the University of Washington. At UW, the experiment will be retrofitted with a dilution refrigerator in place of the present pumped ^{4}He system. This resulting lower operating temperature will allow ADMX to achieve near quantum-limited noise performance and thereby achieve ADMX sensitivity to even the more pessimistically coupled (yet plausible) axions at fractional halo density. This Phase II upgrade at UW/CENPA will be the “definitive experiment”, meaning it will have sensitivity to detect axions or reject the QCD-axion hypothesis with high confidence.

Phase II Upgrade Plans

With the experience of successfully operating SQUIDs *in situ,* we will upgrade the cryogenic hardware of the experiment by retrofitting a dilution refrigerator, thereby reducing the physical temperature of the cavity and SQUID to 100 mK and allowing a system noise temperature of 200 mK. The SQUIDs plus dilution refrigerator cooling of the Phase II system will permit us to explore a substantial fraction of the lowest of the three decades of the open axion mass window, approximately 10^{-6} to 10^{-3} eV, with exquisite sensitivity and thus the Phase II upgrade is highly compelling. The timetable for the Phase II Upgrade has a construction start in FY10. The move of the experiment to CENPA comes from UW internal funds. The ADMX Phase II construction is a DOE-HEP project.

Our University of Florida collaborators have overall responsibility for the Phase II dilution-refrigerator design. Our National Radio Astronomy Observatory (NRAO) collaborators have responsibility for fabricating passive components for the Phase II SQUID amplifiers. LLNL is responsible for the SQUID device fabrication. UW/CENPA is responsible for the site, experimental hardware, and microwave receiver.

The move of the experiment to the University of Washington will occur just after Phase I data-taking ends in 2009 (assuming timely Phase II construction funding).

Phase II Upgrade Site at the University of Washington

The UW has been supporting technical evaluations of the risks in moving the cryostat and magnet assembly to the University of Washington. There was an extensive analysis, with summary. The magnet coil is supported at the bottom against transverse motions by fiberglass bands. These bands and supports were determined to be safe and adequate for reasonable repetitive movers' lateral acceleration limits of 0.1 g. The vertical motions of the coils are constrained by three stainless steel tubes and are fairly robust. But the vertical shipping accelerations are relatively large and this vertical acceleration is the most constraining to shippers at less than 1 g. Several shippers, specializing in moves of this type, can meet this specification and we are instrumenting dummy loads to ensure this specification can be met. A novel feature of this experiment move is the filling and freezing of LN_2 in the magnet bore and vacuum spaces to restrain coil movement. Overall, the preliminary technical evaluation of the magnet/cryostat move assess the risks as low.

Summary

In 2008, we began operating the Phase I ADMX upgrade. This includes taking data with the SQUID receiver chain, but not yet, of course, cooling with the dilution refrigerator for the Phase II upgrade. We have preliminary limits over our first target bandwidth. With the successful transition to Phase I operation we have begun to assemble the Phase II upgrade fabrication proposal. We plan to submit this proposal to DOE/HEP in fall 2009 for a project start in FY10. At the end of Phase I operations in 2009 we plan to move the experiment to its new site at the University of Washington.

The search for the identity of dark matter is one of the key missions in science, and ADMX is a cost-effective and highly sensitive search for what is one of the most compelling dark-matter candidates.

4 Nuclear Astrophysics

4.1 Target development for ^{22}Na(p,γ) measurements

T. A. D. Brown, K. Deryckx, A. García, A. L. Sallaska, K. A. Snover, D. W. Storm, and C. Wrede

Implanted ^{22}Na targets were originally fabricated at TRIUMF in preparation for a series of ^{22}Na(p,γ) resonance measurements around $E_p \simeq 200$ keV (see Sec. 4.2). Implanted targets are particularly vulnerable to beam related phenomena such as sputtering and heating as well as diffusion. The measurements and simulations of three ^{23}Na implanted targets, performed to understand how these ^{22}Na targets would behave under proton bombardment, have been discussed previously[1].

For the purposes of optimizing the production of future ^{22}Na implanted targets, a further seven ^{23}Na targets were fabricated and tested under proton bombardment. Targets were fabricated using copper, tantalum, and nickel as host materials, and implantation energies of E_{Na} = 10 - 30 keV were used. Thin layers (100 - 200 Å) of chromium and gold were also evaporated over some of the targets to provide a protective layer for the implanted sodium. Targets where lower implantation energies are used give rise to a higher peak resonance yield, which is desirable for weak ^{22}Na resonance measurements. Thin protective layers and different implantation hosts offer the possibility of improved resistance to beam sputtering. The ^{23}Na(p,γ) resonance at a lab proton energy of E_{p} = 309 keV was used to determine the implanted sodium distribution. The method of fabrication and bombardment of these targets was similar to the method used for the first three ^{23}Na targets.

Table 4.1-1 illustrates the properties of each target, the total amount of charge deposited during proton bombardment and the corresponding ^{23}Na loss. All ten ^{23}Na targets are shown for comparison. Targets 8-10 were fabricated by evaporating thin layers of nickel or tantalum over an OFHC copper target prior to implantation. The ^{23}Na ions were then implanted directly into the evaporated layer. The ^{23}Na loss was determined by comparing the integrated yield for the initial and final resonance profiles measured for each target. The uncertainties associated with the ^{23}Na loss represent the total error: statistical (determined from the measured total yield) folded with the systematic uncertainties.

Targets 8-9 showed significant sodium loss after less than 8 C of bombardment, indicating that the implantations into nickel and tantalum offer no improvement over the corresponding implantations into copper (i.e. Target 1 and Target 3). However, the results obtained from Targets 4-7 were much more encouraging. They suggest that an evaporated protective layer does inhibit sodium loss from the target. A 200 Å evaporated layer of chromium is the most attractive option since there was no evidence of layer loss during bombardment, and therefore no subsequent shift or change in the shape of the resonance profile. It should be noted that a significantly thicker protective layer (i.e 300 Å) is not desired because of concerns over the amount of straggling and the subsequent broadening of the resonance profile. It was

[1] CENPA Annual Report, University of Washington (2008) p. 47.

Target No.	E_{Na}(keV)	H.M.[1]	$t_{\mathrm{H.M.}}$(Å)[2]	P.L.[3]	$t_{\mathrm{P.L.}}$(Å)[4]	Q_{final}(C)[5]	^{23}Na loss(%)[6]
1	10	Cu	-	-	-	5.8	56 ± 4
2	20	Cu	-	-	-	7.8	41 ± 3
3	30	Cu	-	-	-	11.4	9 ± 6
4	10	Cu	-	Cr	100	2.7	24 ± 4
5	10	Cu	-	Cr	200	6.7	45 ± 5
6	30	Cu	-	Cr	200	7.0	6 ± 5
7	10	Cu	-	Cr/Au	10/100	4.9	12 ± 5
8	30	Ni	1000	-	-	7.5	28 ± 4
9	10	Ta	500	-	-	5.8	46 ± 4
10	30	Ta/Cu	94	-	-	3.4	30 ± 4

Table 4.1-1. ^{23}Na implantation conditions and sodium loss under proton bombardment.
[1]Host material used for implantation.
[2]Thickness of evaporated host material.
[3]Protective layer evaporated over target after implantation.
[4]Thickness of protective layer.
[5]Total charge deposited on target.
[6]Total amount of sodium lost from target.

determined that, among those targets tested, sodium implanted into copper at $E_{\mathrm{Na}} = 30$ keV with a 200 Å protective chromium layer offers the best method for ^{22}Na target fabrication. The details of these ^{23}Na target measurements have been submitted to Nuclear Instruments and Methods B for publication.

4.2 Determining the reaction rate for ^{22}Na(p,γ): preliminary results

L. Buchmann*, T. A. D. Brown, J. A. Caggiano†, K. Deryckx, A. García, D. A. Hutcheon*, D. F. Ottewell*, C. Ruiz*, A. L. Sallaska, K. A. Snover, D. W. Storm, C. Vockenhuber*, and C. Wrede

In order to refine models of nucleosynthesis in novae, which predict the abundances of some cosmic ray gamma emitters such as ^{22}Na, some of the inputs to the models need to be known to a higher level of accuracy. It has been suggested[1] that a new level in ^{23}Mg could lead to a resonance in ^{22}Na(p,γ) at E_p=198 keV, which would dominate the reaction rate in the temperature region of interest to novae, if the strength is above 0.4 meV. This resonance has never been directly measured, and other competing resonances in the energy region around 200 keV have only been determined to the ≈50% level in strength. This reaction, the dominant destructive reaction for ^{22}Na, should be more accurately determined in order to decrease uncertainties in predicted novae yields.

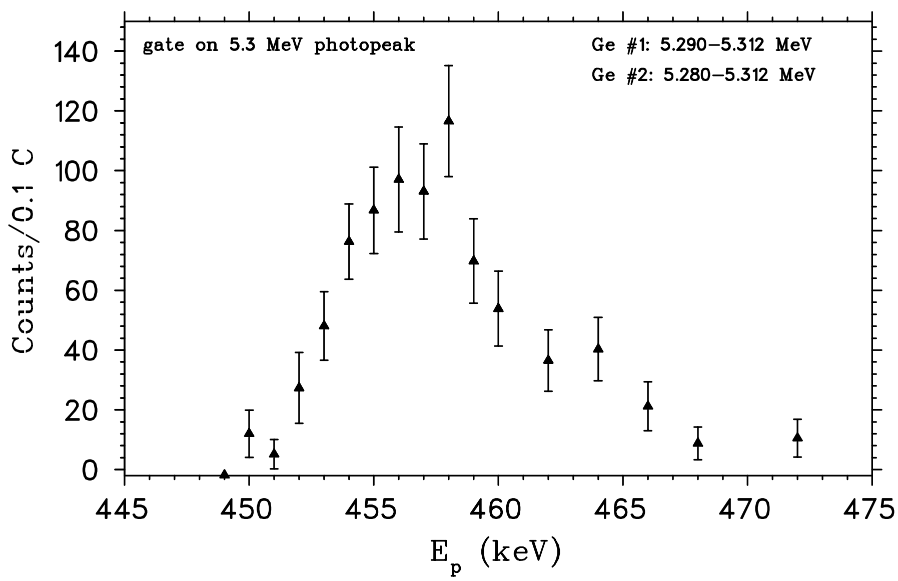

Figure 4.2-1. Excitation function for E_p=456 keV. Energy gates for each germanium detector are given.

The experimental setup has been previously described in detail[2] and consists of a dedicated beamline and chamber, water-cooled target mount, and two HPGe detectors each with cosmic ray shielding. Currently, we have used four ^{22}Na targets: 185 μCi and 300 μCi targets

*TRIUMF, Vancouver, B.C., Canada

†PNNL, Richland, WA

[1] Jenkins *et al*, Phys. Rev. Lett. **92**, 031101 (2004)

[2] CENPA Annual Report, University of Washington (2008) p. 43.

(circa 2005), and two 300 μCi targets (circa December 2008). All were implanted at TRIUMF into an OFHC copper substrate utilizing a 30 keV ^{22}Na beam, and the two most recently implanted targets also had protective layers of 20 nm of chromium evaporated at CENPA. The protective layer was added as the result of extensive target tests with the stable isotope ^{23}Na (see Sec. 4.1).

The bulk of the data to measure the reaction rate accurately has been taken this year, including the new resonance at 198 keV, and all four targets have been bombarded with various integrated beam ($\approx$18 to 25 C each). Relatively well-known resonances at E_p=456 keV (illustrated in Fig. 4.2-1) and at E_p=607 keV were used to monitor target degradation throughout bombardment, and no more than $\approx$20% of the sodium was lost from each target. The preliminary values of the resonance strengths from the E_p=214 keV and E_p=284 keV resonances are consistent with previous measurements; however, the resonance at E_p=232 keV was not observed with the intensity suggested from previous indirect measurements. It is clear that both this resonance, and the one at E_p=198 keV, shown in Fig. 4.2-2, have strengths less than 0.4 meV, which removes both from influencing the reaction rate in a dominant way. The in depth analysis begins in April 2009.

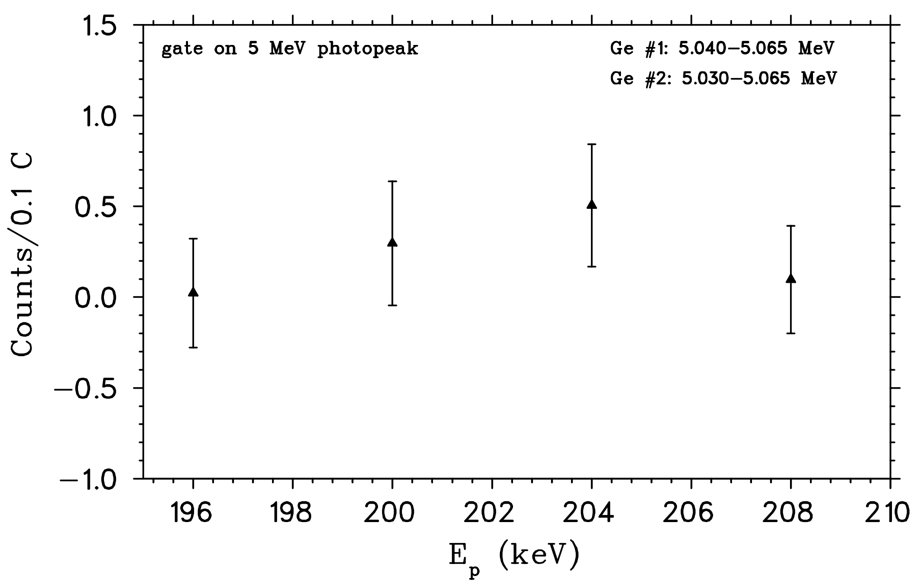

Figure 4.2-2. Excitation function for E_p=198 keV. Energy gates for each germanium detector are given.

4.3 Studies of explosive nucleosynthesis in proton-rich environments

C. Wrede and outside collaborators*,†,‡,§,¶

Classical novae and type I x-ray bursts are explosive events that occur on the surfaces of compact stars (white dwarfs and neutron stars, respectively) that are accreting hydrogen-rich material from the envelope of a companion star. Nucleosynthesis in these environments proceeds mainly via rapid proton captures and β decays along the neutron-deficient side of the valley of β stability (the *rp* process). A knowledge of thermonuclear resonant proton-capture reaction rates on both stable and unstable nuclides is needed to reliably model energy generation and nucleosynthesis in these events. Reactions on stable nuclides have already been studied thoroughly in the laboratory, and now direct and indirect measurements of reactions on unstable nuclides have become a very active field of study. In collaboration with several outside institutions, information is being accumulated on the key (p,γ) reactions on unstable nuclides in the $22 \leq A \leq 31$ region.

Of particular relevance to the study of novae are reactions that affect the production of ^{22}Na and ^{26}Al, which are targets of γ-ray telescopes. Studies at CENPA of ^{22}Na destruction via the ^{22}Na$(p,\gamma)^{23}$Mg reaction are presented elsewhere in this document (see Sec. 4.2). The subsequent ^{23}Mg$(p,\gamma)^{24}$Al reaction connects the NeNa nucleosynthetic cycle to the MgAl cycle and is therefore relevant to the production of both ^{22}Na and ^{26}Al. Resonance energies in the ^{23}Mg$(p,\gamma)^{24}$Al reaction have been determined indirectly by measuring excitation energies of ^{24}Al levels via the ^{24}Mg(^{3}He,t)^{24}Al reaction at Yale University, and the calibration has been updated at CENPA using new nuclear-physics data. These studies have facilitated direct measurements of the ^{23}Mg$(p,\gamma)^{24}$Al reaction using a radioactive-ion beam of ^{23}Mg at TRIUMF during 2008. Analysis of the TRIUMF measurements will also benefit from the ^{24}Al mass measurement (see Sec. 5.2). The nuclear-physics uncertainty associated with the production of ^{26}Al in novae is dominated by uncertainties in the ^{25}Al$(p,\gamma)^{26}$Si reaction rate. By combining the results of recent experiments with past work, the uncertainty in the ^{25}Al$(p,\gamma)^{26}$Si reaction rate has been reduced by roughly an order of magnitude (Fig. 4.3-1). This result should enable new studies of ^{26}Al nucleosynthesis in novae that are not dominated by nuclear-physics uncertainties.

Non-solar Si isotopic ratios measured in candidate presolar nova grains found embedded in primitive meteorites may also be compared to nova-nucleosynthesis model predictions. Models have shown that the ^{29}P$(p,\gamma)^{30}$S reaction rate and, in particular, the ^{30}P$(p,\gamma)^{31}$S

*^{24}Mg(^{3}He,t)^{24}Al work: D. W. Visser (Oak Ridge National Lab.), J. A. Clark, C. M. Deibel, R. Lewis, A. Parikh, and P. D. Parker (Yale Univ.), J. A. Caggiano (TRIUMF).

†^{23}Mg$(p,\gamma)^{24}$Al work: TRIUMF experiment S810, C. Vockenhuber and U. Greife spokespersons; the collaboration is formed by approximately 30 scientists from Argonne National Lab., Univ. of British Columbia, McMaster Univ., Colorado School of Mines, Tech. Univ. München, Univ. of Northern British Columbia, Simon Fraser Univ., TRIUMF, Univ. of Washington, and Univ. Wien.

‡^{25}Al$(p,\gamma)^{26}$Si work: no outside collaborators

§^{31}S and ^{31}Cl work: J. A. Clark, C. M. Deibel, A. Parikh, and P. D. Parker (Yale Univ.), J. A. Caggiano (TRIUMF).

¶^{32}S$(p,t)^{30}$S work: K. Setoodehnia, A. A. Chen, and D. Kahl (McMaster Univ.), J. A. Clark, C. M. Deibel, and P. D. Parker (Yale Univ.).

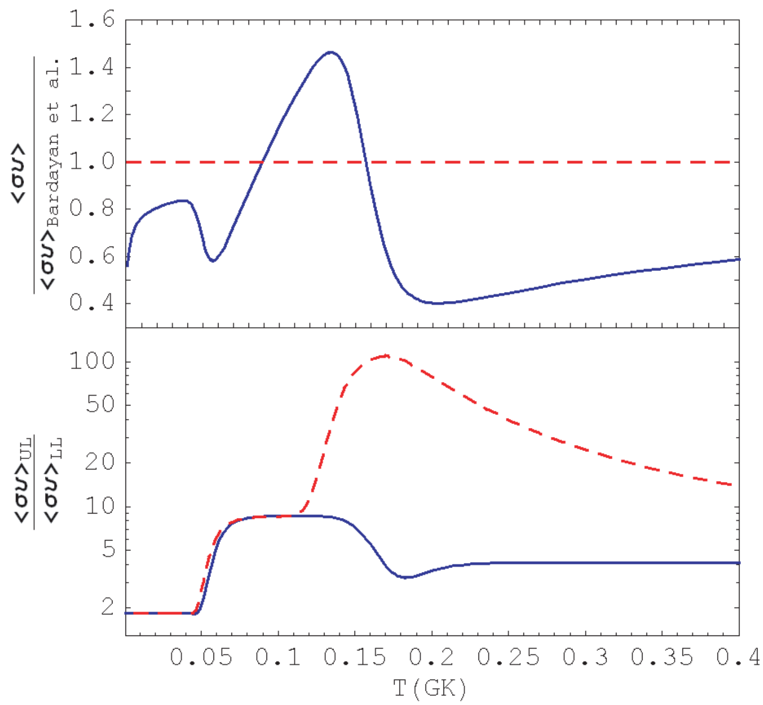

Figure 4.3-1. *Top panel-* Ratios of the ^{25}Al$(p,\gamma)^{26}$Si reaction rates per particle pair, $<\sigma v>$, from the present work (solid blue) and Bardayan *et al.*, PRC 74, 045804 (2006) (dashed red) to $<\sigma v>$ from Bardayan *et al.*. *Bottom panel-* Ratio of the upper-to-lower uncertainty limits of $<\sigma v>$ estimated in the present work (solid blue), and estimated from Bardayan *et al.* (dashed red).

reaction rate affect the Si isotopic ratios in nova ejecta. Indirect studies of these reactions have been (or are being) carried out at Yale University using the ^{32}S$(p,t)^{30}$S, ^{31}P(^{3}He,t)^{31}S, ^{31}P(^{3}He,t)^{31}S$^{*}(p)^{30}$P, and ^{32}S$(d,t)^{31}$S reactions. Preparation of the publication of the results from the latter three reactions was carried out, in part, at CENPA during 2008 and 2009. The ^{32}S$(p,t)^{30}$S work is led by McMaster University and has produced preliminary results but is still in progress. A run in May of 2008 provided an opportunity to successfully test a CENPA-made implanted ^{32}S target for the Q3D experiment outlined in this document (see Sec. 5.2).

In type I x-ray bursts, reactions involving waiting-point nuclides that may impede the nuclear-reaction flow to heavier species and affect the observed burst profile are the most important to study in the laboratory. A waiting point at ^{30}S has been suggested to explain a class of double-peaked x-ray bursts. The ^{31}P(^{3}He,t)^{31}S and ^{31}P(^{3}He,t)^{31}S$^{*}(p)^{30}$P reaction studies described in the preceding paragraph resulted in precise measurements of the energies of the first, and candidate second, $T = 3/2$ levels in ^{31}S. Using this new information with existing experimental information on the 1^{st} $T = 3/2$, $A = 31$ isobaric multiplet and the isobaric multiplet mass equation, the ^{30}S$(p,\gamma)^{31}$Cl Q value and reaction rate have been reevaluated. These results constrain the region of temperature-density-composition parameter space where the ^{30}S waiting point may be active. Preparation of the publication was carried out, in part, at CENPA during 2008 and 2009.

4.4 Investigation of claims about correlations between the decay rate of ^{54}Mn and solar activity

E. G. Adelberger, D. Bergsman, A. García, A. Jeng, A. Palmer, and H. E. Swanson

In a recent publication[1] Fischbach and Jenkins noted a correlation in their data between solar activity and a decrease in the nuclear decay rate of ^{54}Mn. They claim that the solar flare directly caused a decrease in the decay rate of ^{54}Mn through some physical mechanism which has yet to be fully understood. We seek to investigate the validity of this claim by measuring the decay rates of our own radioisotopes over the course of a solar flare.

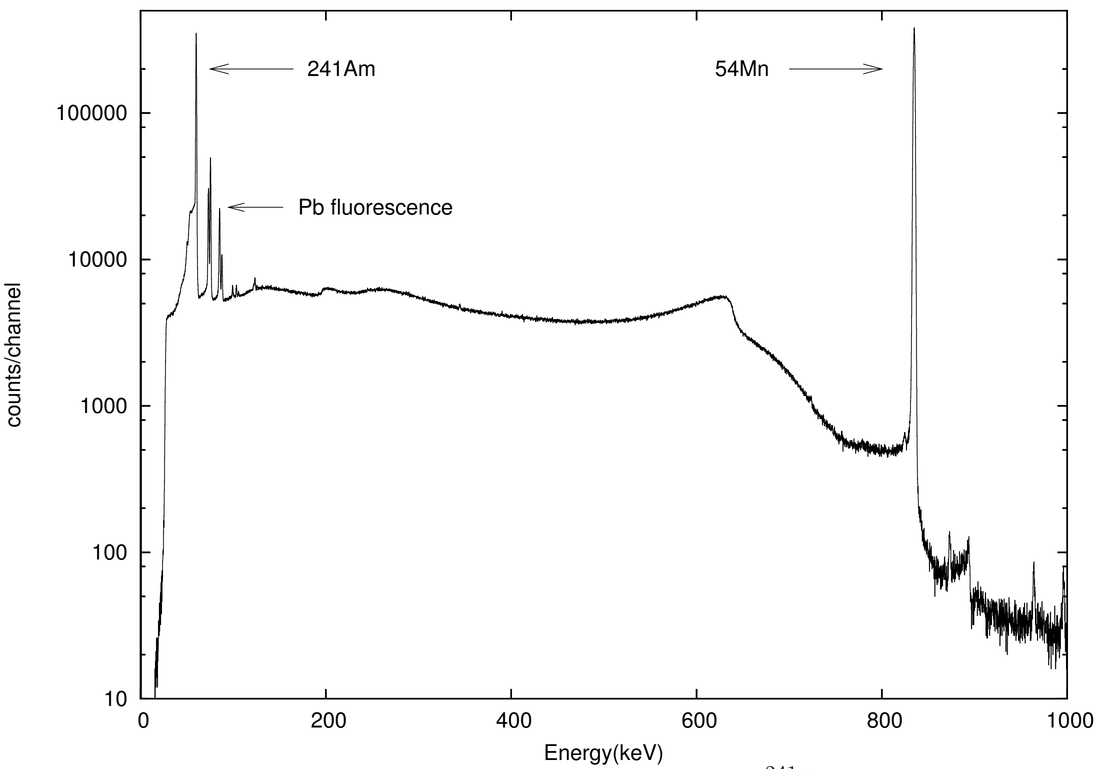

Figure 4.4-1. The γ-ray spectrum. The peak at $\approx$60 keV is from ^{241}Am decay and the one at $\approx$835 keV is from ^{54}Mn decay.

The procedure in this experiment is quite simple. Two active sources are observed by a germanium detector: ^{54}Mn which undergoes a K-capture decay, releasing a 835 keV γ-ray and has a half-life of 312 days, and ^{241}Am which undergoes an alpha decay, releases a 60 keV γ-ray and has a half-life of 432 years. These γ-ray events are compiled by a computer over four hour intervals as was done in the original experiment. The γ-ray events are then categorized into 8192 channels as shown in Fig. 4.4-1 where the two sharp peaks are produced by decays of ^{241}Am and ^{54}Mn. The decay count of each isotope during the time interval is then taken to be the area under each peak, with the average of the background immediately before and after each peak subtracted from its area.

[1]E. Fischbach and J.H. Jenkins, arXiv:0808.3156 [astro-ph] 22 Aug 2008.

In order to safeguard against possible systematic uncertainties which may have occurred in the original experiment, we are not simply analyzing the number of counts from the individual sources but instead are taking the ratio of counts from ^{54}Mn to those of ^{241}Am. This way any unaccounted for downtime, errors in data processing or other unknown issues which would affect the count rates of the two sources equally will be effectively bypassed.

As of now decay data is actively being recorded. While there have been no signs of significant solar activity having taken place during the data-taking process up to this point, we are forming a baseline of nuclear decay data against which we can compare the decay data when a solar event does occur.

5 Nuclear Structure

5.1 Electron capture branch for ^{100}Tc and ^{116}In and nuclear structure relevant for double-beta decays

I. Ahmad*, A. Algora†, J. Äystö‡, D. Bergsman, A. García, S. A. Hoedl, A. Jeng, A. Jokinen‡, D. Melconian§, I. Moore‡, H. Pentilä‡, S. Sjue, H. E. Swanson, S. Triambak, C. Wrede

We want to determine the small EC branches from ^{100}Tc and ^{116}In in order to provide benchmarks for calculations of nuclear beta decays[1]. The two systems have an intermediate nucleus with a $J^{\pi} = 1^{+}$ ground state which allows one to make a connection between the measured EC and beta-decay branches and the two-neutrino decays, which can be used to test the calculations. But the two systems are qualitatively different in that the $A = 100$ one is in a region where deformation may play a significant role, while for the $A = 116$ the nuclei are known to have small deformation.

Last year we published the work on ^{100}Tc[2]. The figure shows the spectrum that allowed extraction of the branch, $B(\mathrm{EC}) = (2.6 \pm 0.4) \times 10^{-5}$.

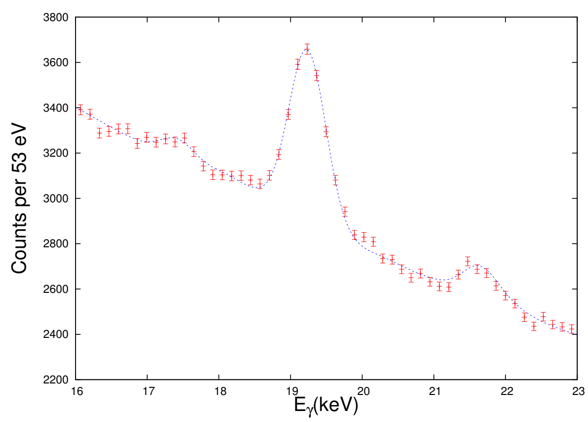

Figure 5.1-1. X ray spectrum from ^{100}Tc. The Mo x rays at $E_{\gamma} \sim 17.5$ keV are produced in EC decays.

We are presently getting ready for an experiment at Jyväskylä to determine the EC branch from ^{116}In. Here the expected branch is larger, but we expect contaminations from isomers that will produce strong In x rays that will generate background for the extraction of the Cd x rays that will allow extraction of the branch. In addition modifications of our electronics are expected to lessen a dead-time effect that limited the ability for determining the beta branches in our previous experiment on ^{100}Tc.

*Argonne National Laboratory, Argonne, IL 60439
†Instituto de Fisica Corpuscular, University of Valencia, Valencia, Spain
‡University of Jyväskylä, FIN-40351 Jyväskylä, Finland
§Texas A&M University, College Station, TX 77843

[1]See e.g. Fäessler *et al.*, Phys. Rev. G **35** , 075104 (2008).
[2]S. Sjue *et al.*, Phys. Rev. C **78**, 064317 (2008).

5.2 Precision mass measurements of ^{20}Na, ^{24}Al, ^{28}P, ^{31}S, and ^{32}Cl

G. C. Harper, K. Deryckx, A. García, D. I. Will, C. Wrede, and outside collaborators*,†

$\mathcal{F}t$ values for $T = 1$ superallowed $0^+ \to 0^+$ β decays impose the most stringent constraints on the CKM quark-mixing matrix-element V_{ud}. The uncertainty in V_{ud} is limited by uncertainties in theoretical correction terms, δ, that are used to convert raw ft values to $\mathcal{F}t \equiv ft(1 - \delta_C)(1 + \delta_R)$ values. One of these, δ_C, accounts for isospin symmetry breaking and is nucleus dependent. For the $T = 2$ superallowed $0^+ \to 0^+$ β decays, δ_C are expected to be much larger. Precise measurements of ft values for the $T = 2$ decays may be used to test calculations of δ_C by comparing to the mean value, $\overline{\mathcal{F}t}$, from the $T = 1$ cases. We have initiated mass measurements of ^{31}S and ^{32}Cl to further improve upon the precision of the $T = 2$ ^{32}Ar decay Q value obtained from CENPA-led work, and of ^{20}Na, ^{24}Al, ^{28}P to provide the first precision information on the Q values of the $T = 2$ decays of ^{20}Mg, ^{24}Si, and ^{28}S.

We are in the process of measuring the masses of ^{31}S and ^{32}Cl to sub-keV precision at the ATLAS facility at Argonne National Laboratory using the Canadian Penning Trap (CPT). A proposal for Experiment 1259 was approved by the ATLAS PAC in May of 2008 and a week of beam time was used in December of 2008. Due to leaks in the CPT gas catcher that corrals radionuclides following production, it was not possible to transport ^{31}S or ^{32}Cl to the precision Penning trap during the 2008 run. Another week of beam time is scheduled for May of 2009 to continue the experiment with improvements to the gas catcher.

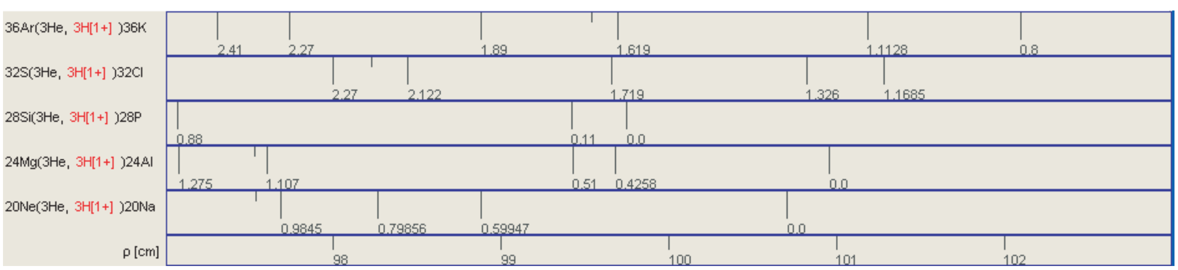

Figure 5.2-1. Kinematics simulation of the Q3D focal plane showing the triton bending radii, ρ, of peaks corresponding to the excitation energies of known nuclear levels in MeV.

The masses of ^{20}Na, ^{24}Al, ^{28}P, and ^{32}Cl will be determined using the Q3D spectrograph in Garching by measuring the Q values of the (^{3}He,t) reactions leading to these nuclides with the ^{36}K(^{3}He,t)^{36}Ar reaction Q value as a calibration (Fig. 5.2-1). Preliminary measurements of the reactions leading to ^{20}Na, ^{24}Al, ^{28}P, and ^{32}Cl were carried out using the Enge split-pole spectrometer at Yale University in December of 2007 to test the feasibility of undertaking sub-keV measurements by this method. Analysis of these data at CENPA show that target-thickness uncertainties contributing ≈ 3 keV dominate the total uncertainty in the Q-value

*ATLAS Experiment 1259: C. Wrede, C. M. Deibel spokespersons; the collaboration is formed by approximately 15 scientists from Argonne National Lab., Univ. of Chicago, Univ. of Manitoba, McGill Univ., Northwestern Univ., and Univ. of Washington.

†Garching Experiment: J. A. Clark and C. M. Deibel (Argonne National Lab.), T. Faestermann, R. Hertenberger, R. Krücken, A. Parikh, and H. Wirth (Tech. Univ. München), P. D. Parker (Yale Univ.).

measurements. To reduce this uncertainty we are preparing thin ion-implanted targets at CENPA (see Sec. 8.2) for use in Garching where systematic uncertainties can be reduced substantially without compromising statistics. Using the low-energy beam line of CENPA's tandem Van de Graaff, four 30 μg/cm^2 carbon foils have been been successfully implanted with ≈ 4 μg/cm^2 of ^{20}Ne, ^{28}Si, ^{32}S, and ^{36}Ar. Work is in progress to prepare a ^{24}Mg target by the same method, which would complete the set of targets. Packing and shipping of thin carbon foils to Garching (and back) has also been tested successfully. A proposal was submitted in March of 2009 and beam time in Garching is anticipated for September of 2009.

6 Relativistic Heavy Ions

6.1 Summary of event structure research

T. A. Trainor

In previous work we established the two-component model of nuclear collisions at RHIC for both single-particle spectra and two-particle angular and transverse-rapidity correlations. The two components are interpreted as longitudinal nucleon fragmentation and transverse scattered-parton fragmentation (dominated by minijets). We have also observed "elliptic flow" v_2 as an isolated azimuth quadrupole component in 2D angular autocorrelations.

In the past year we have extended that picture in several ways. Most importantly, we have achieved a direct quantitative relation between pQCD calculations and hard-component data, relating a minimum-bias parton spectrum and measured fragmentation functions to hard-components (fragment distributions) in spectra and correlations. The data so treated indicate that there is essentially no parton absorption or thermalization even in central Au-Au collisions, although the fragmentation process is strongly modified.

In related work we have re-examined conventional analysis methods for estimating jet yields. We find that certain spectrum ratio measures suppress jet structure at smaller p_t, and methods applied to jet azimuth correlations tend to underestimate higher-p_t jet yields for more-central A-A collisions. We have developed methods to reverse such biases.

General topics include

- Determination of the p_t dependence of the azimuth quadrupole component using 2D angular autocorrelations to eliminate systematic jet contributions
- Extending minijet angular correlation measurements to Cu-Cu to better understand A dependence, especially for our recently-discovered "sharp transition" from a Glauber linear-superposition reference on centrality.
- Re-examination of the hydrodynamic model applied to A-A collisions and related analysis methods
- Accurate descriptions of p-p̄ fragmentation functions in comparison to e^+-e^- fragmentation functions for the purpose of pQCD modeling
- pQCD calculations of fragment distributions in vacuum and medium
- Inference of a minimum-bias parton spectrum from hadron spectrum data
- Comparing evolution of spectrum and correlation hard components with A-A centrality with pQCD predictions
- Methods for isolating true jet yields from azimuth correlations and reducing systematic errors in existing data

6.2 Pileup rejection for angular correlations in high-luminosity A-A data

D. Prindle and T.A. Trainor

The primary tracking detector in STAR is a large TPC. Any collisions occuring within $\pm 40\mu$s of the triggered collision will be included in the TPC readout, and their tracks can be associated with the vertex from the triggered collision. Here we describe characteristics of pileup collisions and show that we can effectively remove pileup contaminated vertices.

Tracks from pileup *before* the trigger are not projected as far as their true drift distance. Tracks crossing the central membrane are split and appear to end (start) in the TPC active volume for the inner (outer) part of the track. This type of event is shown in Fig. 6.2-1. These events have tracks on one half of the TPC starting a distance d from the central membrane and in the other half of the TPC ending the same distance d from the central membrane. Tracks in each half of the TPC will form separate vertices which we find by extrapolating to r = 0 (r is radius) in r − z space. These vertices will be 2d apart.

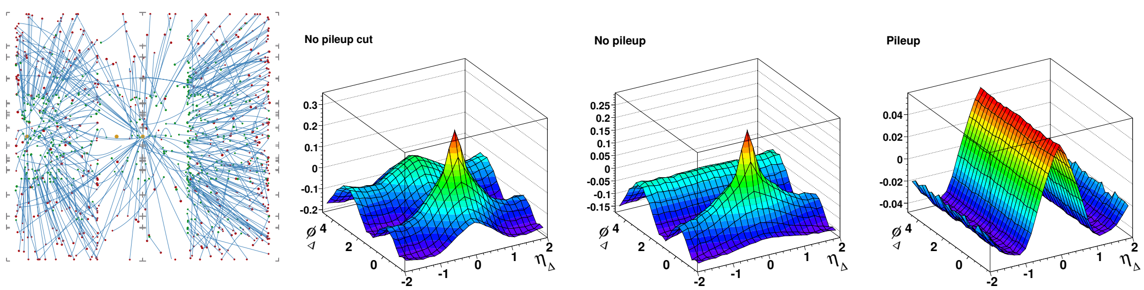

Figure 6.2-1. Panel 1 shows an image of a reconstructed TPC event containing a pileup collision about 10μs before the trigger. Panels 2, 3 and 4 show 2-point correlations with no pileup cut, after pileup rejection and the correlations of events that are rejected.

In contrast, for pileup *after* the trigger the tracks are projected farther than their true distance. The last points on the tracks are now a distance d from the readout plane at both ends of the TPC. Their reconstructed vertices will be a distance 2d apart.

The pileup rejection algorithm we have developed first identifies pairs of pileup candidates by examining the first/last measured z positions of global tracks. For each half of the TPC we estimate the pileup z-vertex position and predict the z-vertex of the other set of pileup tracks. If this position is too close to an otherwise good vertex we reject the event.

For Au-Au and Cu-Cu collisions we reject about 75% of vertices that can be contaminated with pileup tracks. We see residual signatures of pileup in 2-point correlations even after rejecting most of the pileup contamination. We complete the rejection by analysing with and without pileup rejection cuts and extrapolating using our estimated pileup rejection efficiency.

$$
\begin{aligned}
\frac{\Delta\rho}{\sqrt{\rho_{\rm ref}}}(\text{noCut}) &= \frac{\Delta\rho}{\sqrt{\rho_{ref}}}(noPileup) + \frac{\Delta\rho}{\sqrt{\rho_{ref}}}(pileup) \\
\frac{\Delta\rho}{\sqrt{\rho_{ref}}}(cut) &= \frac{\Delta\rho}{\sqrt{\rho_{ref}}}(noPileup) + \frac{\Delta\rho}{\sqrt{\rho_{ref}}}(pileup) \times (1 - f)
\end{aligned}
$$

6.3 Cu-Cu angular correlations and the sharp transition

D. Prindle and T.A. Trainor

Previous characterization of charge-independent angular autocorrelations for 62 and 200 GeV Au-Au collisions has observed a minijet component that has a strong centrality dependence with amplitude and η_Δ width suddenly increasing beyond a Glauber linear superposition (GLS) expectation at a well defined centrality.[1] Here we report a similar study for 200 and 62 GeV Cu-Cu collisions.

We have more Cu-Cu events than Au-Au, allowing us to do finer centrality binning. The lower multiplicity for Cu-Cu means track merging and splitting are not as big an affect as they are in Au-Au collisions. On the other hand, because of the higher luminosity, especially for the 200 GeV Cu-Cu, event pileup is a much bigger problem (see Sec. 6.2).

We characterize our 2-point correlations on $(\eta_\Delta, \phi_\Delta)$ by fitting to a function that includes

- same-side 2D Gaussian (interpreted as a minijet peak)
- $\cos(\phi_\Delta)$ (away side jet peak)
- $\cos(2\phi_\Delta)$ (elliptic flow)
- narrow 2D exponential on the same-side (accounting for HBT and e^+e^- conversions)
- 1D Gaussian on η_Δ (needed for p-p and peripheral A-A collisions)
- offset (accounts for fluctuations due to multiplicity width of bin)

Values for four of the parameters are shown in Fig. 6.3-1. The first three panels describe aspects of minijets and all initially follow the GLS expectation then show a rapid increase at a reasonably well-defined centrality. In contrast, the width of the same-side 2D Gaussian actually decreases with increasing centrality. The fouth panel in Fig. 6.3-1 shows the amplitude of the $\cos(2\phi_\Delta)$ quadrupole component. This component seems to be un-coupled from the minijet transition for all the systems we have studied.

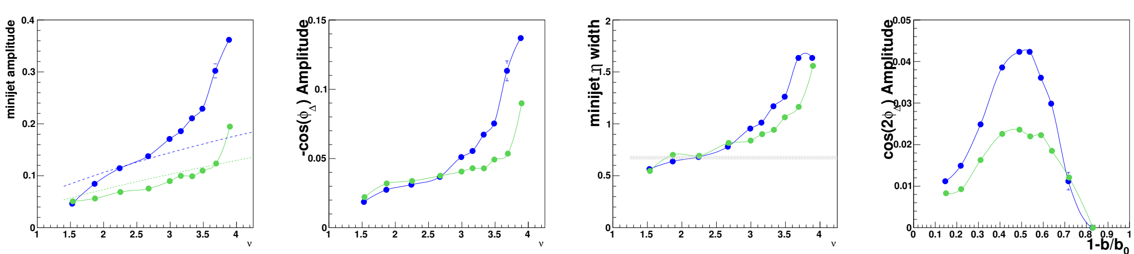

Figure 6.3-1. Panel 1 shows amplitudes of same-side 2D Gaussian. Panel 2 shows amplitude of $\cos(\phi_\Delta)$ term and tracks 2D Gaussian.amplitude. Panel 3 shows the η_Δ width of the same-side 2D Gaussian. The deviation from Glauber linear superposition happens near the same centrality as for the amplitude. Panel 4 shows the $\cos(2\phi_\Delta)$ amplitude. This shows a smooth behaviour where components describing a minijet peak show a transition.

[1] Nuclear Physics Laboratory Annual Report, University of Washington (2008) p. 61.

6.4 Azimuth quadrupole marginal p_t dependence

D. T. Kettler

Measurements of the azimuthal quadrupole moment, commonly represented as v_2, have been one of the major results at RHIC. Although there is a wide variety of techniques used to measure v_2, usually attributed to the phenomenon of 'elliptic flow', most of them either do not reliably distinguish between so-called flow and nonflow effects or do so in very model-dependent ways. In the past we have described a method which makes use of 2D angular autocorrelations to accurately and effectively measure the azimuth quadrupole even in the presence of large nonflow terms. An autocorrelation is derived from pair density $\rho(x_1, x_2)$ by averaging it along diagonals in space (x_1, x_2) parallel to the sum axis. A 2D autocorrelation is made by applying this procedure to two pairs of variables simultaneously, in this case a projection from the $(\phi_1, \phi_2, \eta_1, \eta_2)$ space onto the $(\phi_\Delta, \eta_\Delta)$ space. The left panel in the figure below gives an example of such a 2D autocorrelation.

It is often desirable to study the p_t dependence of the quadrupole rather than just the p_t-integrated quantity. As the quadrupole is measured with two-particle correlations the correlation amplitude depends on the p_t of each particle. However, typical $v_2(p_t)$ plots are done with marginal distributions, meaning that particles within the given p_t range are correlated with the entire event. We typically transform p_t into a transverse rapidity, represented by y_t. Due to the inherent diagonal symmetry of the $y_t \times y_t$ space this is equivalent to cross-shaped cuts as shown in the second panel of the figure below. After making these cuts the corresponding angular correlations can be fit to extract the quadrupole term. v_2 is related to the second Fourier components of the correlation on ϕ_Δ by $\Delta\rho[2]/\sqrt{\rho_{ref}} = n v_2^2/2\pi$

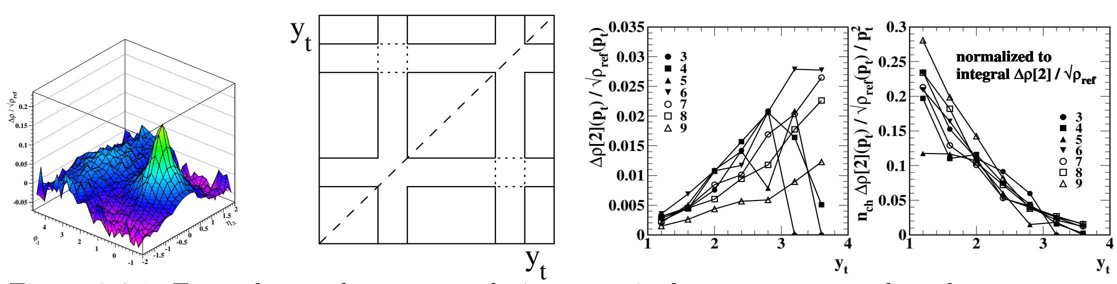

Figure 6.4-1. Example angular autocorrelation, marginal y_t cutspace, quadrupole term y_t dependence for different centralities.

A simple Fourier decomposition is all that is necessary if the only sources of correlations are related to flow. However, in real data there will also be significant contributions from nonflow (jet) terms which are distinguishable from their dependence on the η_Δ axis. The principal structures are a 2D same-side Gaussian peak, a 1D gaussian on η_Δ, a dipole component $\cos(\phi_\Delta)$, and a quadrupole component $\cos(2\phi_\Delta)$. There is also a sharp peak at the origin representing electron pairs and HBT effects which we can model with an exponential.

The extracted quadrupole marginal y_t dependence is plotted for several different centralities of 200 GeV Au-Au collisions in the third figure above. In the fourth panel the quadrupoles are normalized to their p_t-integrated values and multiplied by n_{ch}/p_t^2 which reveals a common trend.

6.5 Azimuth quadrupole joint (p_{t1}, p_{t2}) structure

D. T. Kettler

In the previous article I described the procedure for measuring the marginal p_t dependence of the azimuthal quadrupole. More information can be learned by studying the full 2D momentum space. The left figure below shows a number correlation in (y_{t1}, y_{t2}) space, which includes all possible sources of correlations. What we wish to do is make cuts in this space, fit the corresponding angular autocorrelations, and plot the analogous (y_{t1}, y_{t2})-dependence of a particular feature, such as the azimuthal quadrupole.

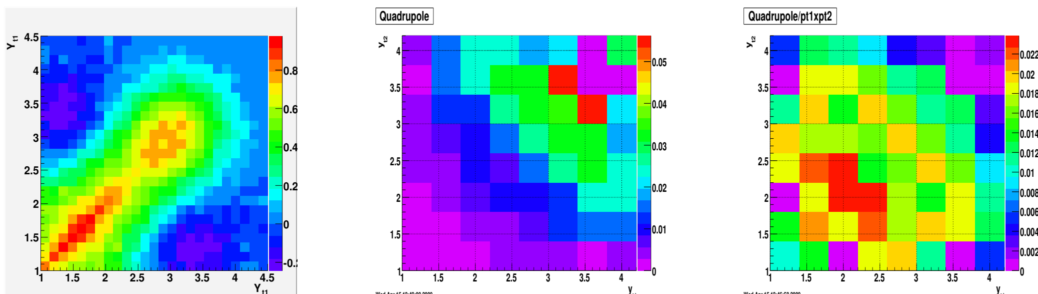

Figure 6.5-1. Example (y_{t1}, y_{t2}) number correlation, 2D quadrupole, and 2D quadrupole divided by $p_{t1}p_{t2}$

In order to measure the azimuthal quadrupole one can fit all components and extract the quadrupole term as described in the previous article. However, it is also notable that the only terms in our fit that contribute to the away-side structure and have ϕ_Δ-dependence are the dipole and quadrupole. Thus it is possible to project 2D angular correlations onto ϕ_Δ and fit *only the away side* with simple Fourier terms to extract the quadrupole. This procedure is much simpler and faster and is therefore useful when fitting a large number of histograms, as is required to examine the (y_{t1}, y_{t2})-dependence. It is also useful if there aren't enough statistics in a (y_{t1}, y_{t2}) cutbin to reliably measure the full 2D angular histograms.

The second panel above shows the quadrupole amplitude in (y_{t1}, y_{t2}) space for 20-30 percent central 200 GeV Au-Au collisions. The fourth panel shows the same quadrupole amplitudes divided by the product of p_{t1} and p_{t2}, which removes a trivial p_t dependence. There is still much work to be done to interpret these results. However it is immediately noteable that the quadrupole amplitudes are not factorizable in (y_{t1}, y_{t2}) space, meaning that the 2D quadrupole does not appear to be a product of two 1D functions. This has significant implications for any trigger-particle jet analysis that requires a v_2 subtraction, as they involve angular correlations in off-diagonal regions of the (y_{t1}, y_{t2}) space.

6.6 Online quality assurance for STAR data acquisition

D. T. Kettler

The STAR QA system is used to actively monitor data being taken by the various subcomponents of the STAR detector in order to ensure that they are working properly and that the data are valid. QA is divided into two components: online QA and offline QA. Online QA is what the shift crew monitors while actively taking data, and the offline QA is a more detailed analysis which is conducted in QA shifts on data that have already been taken. The importance of online QA is that while offline QA can be used to mark runs as bad it is less useful for noticing and responding to detector problems as they occur.

I began maintaining this system in 2007 in preparation for Run 8 and have continued to do so this year for Run 9. Most of the software development can be done via remote login. In order to respond to problems as they developed I coordinated activity with personnel at BNL.

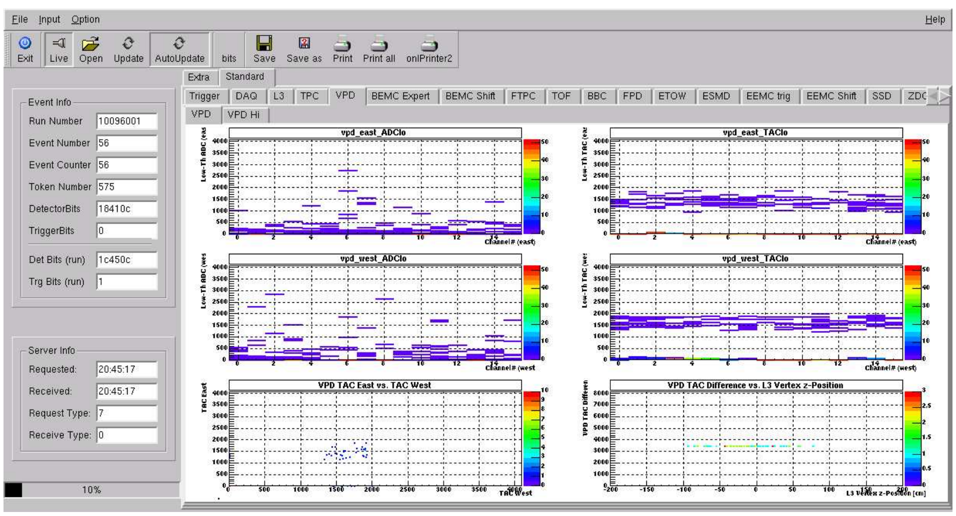

Figure 6.6-1. Example of plots in the online QA client software

In preparation for Run 9 these two significant changes impacted the online QA system. First, the STAR detector has upgraded to a new DAQ system, and much of the interface to the raw data had to be updated. Second, the decision was made to migrate the online QA system away from the custom "make files" it had been using and incorporate it into the standard STAR "build system" and software environment so a great deal of the code had to be revised or rewritten. While working on this aspect several small improvements were also made, such as moving away from hard-coded file paths in favor of configuration files.

Additional updates included major changes to the electromagnetic calorimeter (EMC) histograms, updates to the vertex position detector (VPD) histograms, updates to the pp2pp experiment histograms, incorporating reference plots into the main QA software, and improvements to the way histogram groups are managed. Many of the changes made this year were designed to improve maintainability of the codebase in the future.

6.7 The blast-wave model and the myth of radial flow

T. A. Trainor

Evidence for radial flow in nuclear collisions is essential to sustain the hydro model at RHIC. Evidence is sought via so-called *blast wave* (BW) fits to spectra, for A-A collisions and even p-p collisions. Fig. 6.7-1 (first panel) shows a simple procedure to generate a BW model spectrum. A Maxwell-Boltzmann (MB) spectrum $1/m_t\, dn/dm_t \propto \exp(-m_t/T)$ transformed to transverse rapidity y_t with $m_t = m_0 \cosh(y_t)$ is boosted (blue shifted) by varying amounts $\Delta y_t \sim \beta_t$ according to Hubble expansion). The resulting BW spectrum corresponds to mean transverse speed $\langle\beta_t\rangle \sim 0.25$ sometimes attributed to p-p collisions. Fig. 6.7-1 (second panel) compares the resulting BW model (upper solid curve) with a two-component representation of 200 GeV p-p data (dash-dotted curve). BW fits are typically restricted to a "hydro" y_t interval bounded above by $y_t \sim 3.3$ ($p_t \sim 2$ GeV/c, vertical dashed line). $\Delta y_t = 0.25$ is the "radial flow" value typically obtained from BW fits to p-p spectra. Although the BW model appears to describe data within a restricted y_t interval it cannot describe an extended interval because the curvature is much larger than typical data trends. From this comparison it is clear that for p-p spectra the BW model is mainly accomodating spectrum soft component $S_0(y_t)$, which describes the *zero-density limit* of p-p collisions where radial flow would be least likely.

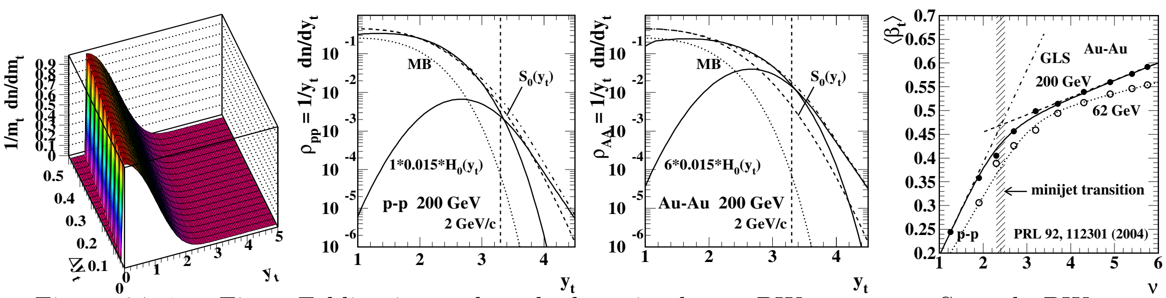

Figure 6.7-1. First: Folding-integral method to simulate a BW spectrum, Second: BW spectrum (upper solid curve) compared to p-p data (dash-dotted curve), Third: A similar comparison for central Au-Au collisions, Fourth: Inferred BW radial velocity $\langle\beta_t\rangle$ vs centrality ν, showing correspondence to a sharp transition in jet correlations at $\nu = 2.4$.

Fig. 6.7-1 (third panel) shows the two-component reference for central Au-Au collisions at 200 GeV ($\nu = 6$, dash-dotted curve) and fixed soft component $S_0(y_t)$. The solid curve is a simple BW model with $\langle\beta_t\rangle = 0.6$ and $T_{kin} = 0.10$ GeV. Within the restricted y_t interval conventionally assigned to hydro (left of the dashed line) the BW model again seems to describe the data well, but fails elsewhere. Fig. 6.7-1 (fourth panel) shows published $\langle\beta_t\rangle$ (solid dots) from BW fits to identified-particle spectra for p-p and Au-Au collisions at $\sqrt{s_{NN}} = 200$ GeV. The solid curve interpolates the lines through points. The hatched region denotes a sharp transition observed in minijet characteristics from correlation data and in the Au-Au spectrum hard component for pions and protons. Evolution of BW parameters $(\langle\beta_t\rangle, T_{kin})$ from (0.25,0.15 GeV) to (0.6,0.09 GeV) corresponds to *six-fold increase* of the spectrum hard component with centrality. The hydro BW model competes with QCD jet processes previously identified in elementary collisions and expected to follow binary-collision scaling in A-A collisions.

6.8 The spectrum soft component as a unversal feature of all fragmentation processes

T. A. Trainor

The hydro-motivated blast-wave (BW) spectrum model assumes that radial flow distorts a nominal Maxwell-Boltzmann (M-B) spectrum shape by raising the spectrum at larger m_t. The deviation from M-B is parametrized by mean transverse flow velocity $\langle\beta_t\rangle$. An early application of the BW model was to SPS S-S spectrum data at 19 GeV. Fig. 6.8-1 (first panel) shows a π^- spectrum on m_t (solid points) for SPS fixed-target 0-2% central S-S collisions at 200A GeV ($\sqrt{s_{NN}} \approx 19$ GeV). A BW model was used to infer radial flow with mean speed $\langle\beta_t\rangle \sim 0.25$. The curve labeled S_0 is just the spectrum soft component (zero-density limit) for $\sqrt{s} = 200$ GeV NSD p-p collisions. S-S collisions at 19 GeV appear to be completely described for all centralities by a 200 GeV soft reference with negligible hard component. Is there significant radial flow in p-p collisions, or was the BW model mis-applied to S-S data?

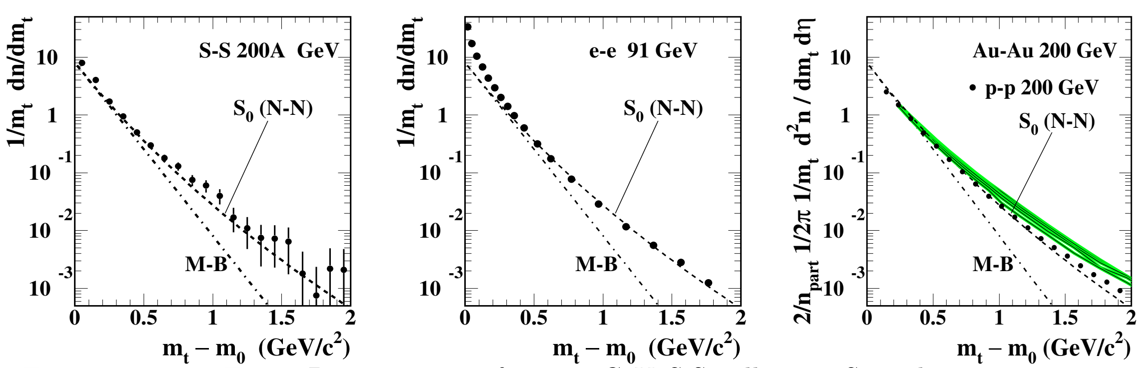

Figure 6.8-1. First: Pion spectrum from 19 GeV S-S collisions, Second: Transverse momentum spectrum from 91 GeV dijets, Third: Spectra from five centralities of 200 GeV Au-Au collisions (solid curves) and from 200 GeV p-p collisions (points).

Fig. 6.8-1 (second panel) shows an m_t spectrum (solid dots) from LEP e^+-e^- collisions at $\sqrt{s} = 91$ GeV. The spectrum is derived from a sphericity analysis of q-$\bar{q}$ dijets and represents the fragment momentum distribution transverse to the q-$\bar{q}$ axis. The LEP data were normalized to match the same p-p soft component S_0 plotted in the left panel (dashed curve), and hence the SPS S-S spectrum. The shape of the transverse mass spectrum from LEP FFs at 91 GeV thus agrees well with the soft component of p-p spectra at 200 GeV and with the spectrum from central S-S collisions at 19 GeV.

The BW model has been more recently applied to RHIC spectra to infer systematic variation of transverse speed $\langle\beta_t\rangle$ and kinetic decoupling temperature T_{kin}. Fig. 6.8-1 (third panel) shows spectra from 200 GeV Au-Au for five centralities (solid curves) and 200 GeV p-p data (points) compared to the same M-B and S_0 curves in the left panels. The commonality of the S_0 spectrum shape (Lévy distribution) across energies and collisions systems suggests that the spectrum soft component is a universal feature of longitudinal fragmentation whatever the leading particle—parton or hadron. It is quite unlikely that hydro expansion plays a role in LEP e^+-e^- collisions. Thus, inference of a radial flow velocity from the same spectrum shape in A-A collisions (and especially p-p collisions) is also doubtful.

6.9 Dramatic differences between p-p̄ and e$^+$-e$^-$ fragmentation functions: Does the hard Pomeron break FF universality?

T. A. Trainor

Fig. 6.9-1 (first panel) shows fragmentation function (FF) data from p-p̄ collisions at FNAL (CDF) for nine jet energies (points). The dashed curves represent LEP/HERA e-e FFs (parameterized) for the same jet energies. The solid curves through the data are derived by modifying the e-e FFs by a cutoff function $g_{cut}(y) = \tanh\{(y - y_0)/\xi_y\}$. The CDF FFs also reveal a systematic amplitude saturation or suppression at larger parton energies compared to LEP systematics which has been incorporated in the solid curves. The cutoff function represents real fragment and energy loss from p-p relative to e-e FFs. The difference implies that FFs are not universal. Fig. 6.9-1 (second panel) shows ratios of p-p̄ to e-e FFs on fragment rapidity $y = \ln\{(E + p)/m_\pi\}$. Whereas the low-momentum cutoff is common to all parton energies the suppression at larger fragment momentum increases with increasing parton energy.

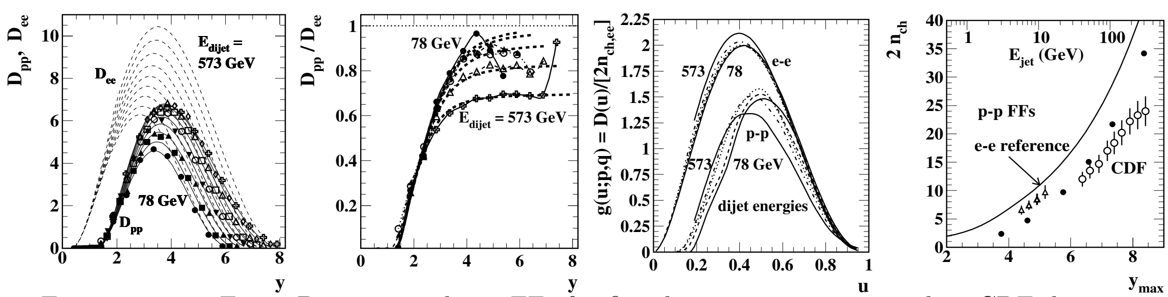

Figure 6.9-1. First: Parametrized p-p̄ FFs for five dijet energies compared to CDF data (points), Second: p-p̄ / e-e FF ratios, Third: FF comparison on normalized rapidity $u = (y - y_{min})/(y_{max} - y_{min})$, Fourth: Corresponding dijet multiplicities for p-p FFs (solid points) and published values (open points).

Fig. 6.9-1 (third panel) shows FFs normalized to unit integral plotted on normalized rapidity u. Whereas e-e FFs so plotted are nearly independent of energy scale p-p̄ FFs are obviously strongly suppressed depending on energy scale. Fig. 6.9-1 (fourth panel) shows parametrized dijet multiplicity systematics (solid points) for p-p̄ FFs (from the modified e-e parametrization). The solid curve represents unmodified e-e FFs as a reference. There is substantial reduction of p-p FF multiplicities due to the suppression. Also plotted are CDF FF multiplicities from reconstructed jets (open triangles and open circles). Dijet multiplicities are strongly suppressed in p-p collisions compared to equivalent FFs in e-e collisions, reduced by 30-70%. FFs are apparently strongly "modified" in p-p collisions as well as A-A collisions.

A possible explanation for the large difference in parton fragmentation is hard-Pomeron exchange. In p-p collisions two color singlets (protons) exchange momentum. If the exchange is also color singlet (Pomeron) then the "scattered" partons are not color connected to each other, are connected instead to their parent projectile nucleons. The geometry of color fields in p-p collisions may not be that of a q-q̄ color dipole as in e-e collisions. For Pomeron exchange two dipoles are involved, and parts of the dipole radiation may appear outside the acceptance in which the observed jets appear.

6.10 The minimum-bias parton spectrum and saturation-scale arguments

T. A. Trainor

A model for the parton p_t spectrum resulting from minimum-bias scattering into an η acceptance near projectile mid-rapidity can be parametrized as

$$\frac{1}{p_t}\frac{d\sigma_{dijet}}{dp_t} = f_{cut}(p_t)\frac{A_{p_t}}{p_t^{n_{QCD}}} \rightarrow \frac{d\sigma_{dijet}}{dy_{max}} = f_{cut}(y_{max})\, A_{y_{max}}\, \exp\{-(n_{QCD}-2)\, y_{max}\}, \qquad (1)$$

which defines QCD exponent n_{QCD}, with $y_{max} \equiv \ln(2\, p_t/m_\pi)$. The cutoff factor

$$f_{cut}(y_{max}) = \{\tanh[(y_{max} - y_{cut})/\xi_{cut}] + 1\}/2 \qquad (2)$$

represents the minimum parton momentum which leads to detectable charged hadrons as neutral pairs (i.e., local charge ordering). Parton spectrum and cutoff parameters are determined via fragment distribution (FD) compared with p-p and Au-Au spectrum hard components.

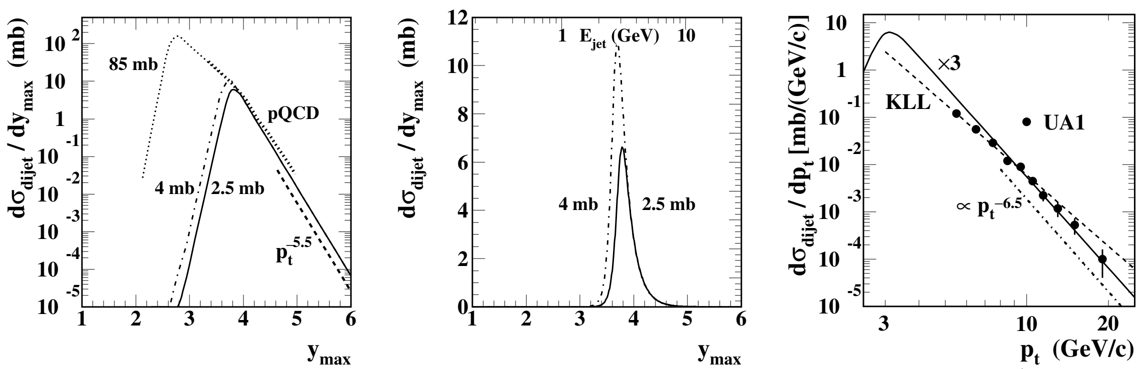

Figure 6.10-1. First: Parton spectra inferred from this analysis for p-p collisions (solid curve) and central Au-Au collisions (dash-dotted curve) compared to an ab-initio pQCD theory result (bold dotted curve), Second: Parton spectra from this analysis in a linear plot, Third: Parton spectrum from reconstructed jets (UA1, solid points) compared to theory (dashed curve) and this analysis (solid curve, note factor 3).

Fig. 6.10-1 (left panels, semilog and linear formats) shows the parton spectrum (solid curve) inferred from a measured p-p spectrum hard component. y_{cut} and $A_{y_{max}}$ are well-defined by the p-p hard component, and n_{QCD} is defined by Au-Au spectrum hard components extending to larger y_t. The dotted curve in the first panel is an ab-initio pQCD calculation. The linear plot (second panel) indicates the narrowness of the spectrum, with effective mean energy near 3 GeV (defining minijets). Fig. 6.10-1 (third panel) compares the spectrum defined in this analysis (solid curve, and note the factor 3) with 200 GeV UA1 jet cross-section data obtained by event-wise jet reconstruction (points). The UA1 spectrum integral is 4 mb. The spectrum from Eq. (1) integrates to 2.5 ± 0.6 mb with well-defined cutoff $\sim$ 3 GeV which agrees well with pQCD theory. The KLL parametrization $600/p_t^5$ mb/(GeV/c) (dashed line) integrates to 2.2 mb above 3 GeV/c. The pQCD dotted curve in the first panel extends down to 1 GeV based on *saturation scale* arguments, implying 25× greater gluon yield than is observed in p-p collisions (spectrum hard component). The large predicted gluon yield provides a basis for the large energy densities which are said to drive hydrodynamic flows.

6.11 pQCD calculations of minimum-bias fragment distributions

T. A. Trainor

The pQCD folding integral used to obtain fragment distributions (FDs) can be written

$$\frac{d^2n_h}{dy\,d\eta} \approx \frac{\epsilon(\delta\eta,\Delta\eta)}{\sigma_{NSD}\,\Delta\eta}\int_0^\infty dy_{max}\, D_{xx}(y,y_{max})\,\frac{d\sigma_{dijet}}{dy_{max}}, \tag{1}$$

where $D_{xx}(y, y_{max})$ is the dijet FF ensemble with xx = e-e, p-p, A-A, in-medium or in-vacuum, and $d\sigma_{dijet}/dy_{max}$ is the parton energy spectrum. Spectrum hard component $d^2n_h/dy\,d\eta$ represents the hadron yield from scattered parton pairs into one unit of η. Efficiency factor $\epsilon \sim 0.5$ includes the probability that a partner jet falls within η acceptance $\delta\eta$. $\Delta\eta \sim 5$ is the effective 4π interval for scattered partons. σ_{NSD} is the cross section for NSD p-p collisions.

Fig. 6.11-1 (first panel) shows the integrand of Eq. (1) incorporating unmodified FFs from e-e collisions with lower bound at $y_{min} \sim 0.35$ ($p_t \sim 0.05$ GeV/c) (dotted line). Fig. 6.11-1 (second panel) shows the corresponding FD (solid curve), the "correct answer" for an FD describing inclusive hadrons from inclusive partons produced by *free* parton scattering from p-p collisions. The dash-dotted curve represents the hard-component model inferred from p-p collisions. The FD from e-e FFs lies well above the measured p-p hard component for hadron $p_t < 2$ GeV/c ($y_t < 3.3$), and the mode is shifted down to ~ 0.5 GeV/c. The "correct" e-e FD strongly disagrees with the relevant part of the p-p p_t spectrum—the hard component. Despite the strong disagreement the e-e FD is the correct reference for nuclear collisions.

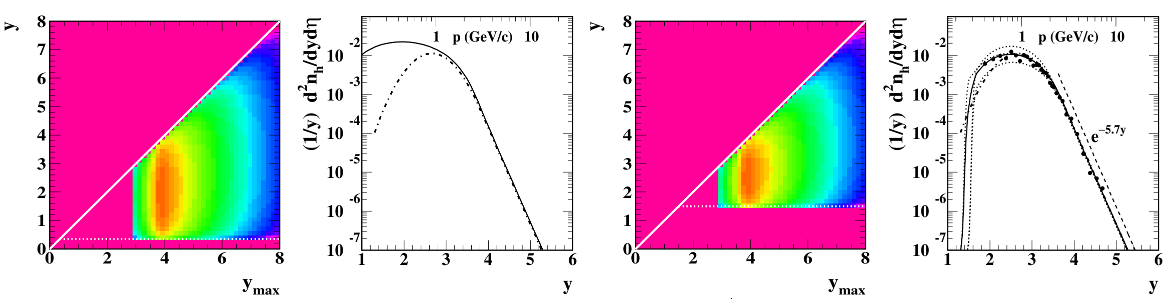

Figure 6.11-1. First: pQCD folding-integral argument for e^+-e^- FFs, Second: Corresponding fragment distribution (solid curve) and p-p hard-component reference (dash-dotted curve), Third: Folding-integral argument for p-p̄ FFs, Fourth: Corresponding fragment distribution (solid curve) compared to p-p hard-component data (points). Dotted curves correspond to ±10% change in parton spectrum cutoff energy about 3 GeV.

Fig. 6.11-1 (third panel) shows the integrand of Eq. (1) incorporating e-e FFs modified by a cutoff function to describe p-p̄ FFs. The lower bound of p-p FFs is raised to $y_{min} \sim 1.5$. Fig. 6.11-1 (fourth panel) shows the corresponding FD H_{NN-vac} (integration of the third panel over y_{max}) as the solid curve. The mode of the FD is ~ 1 GeV/c. The dash-dotted curve is a Gaussian-plus-tail model function, and the solid points are hard-component data from p-p collisions. That comparison determines the parton spectrum parameters. The p-p data are well-described by the pQCD folding integral. This procedure establishes an absolute quantitative relationship among parametrized parton spectrum, measured FFs and measured spectrum hard components over all p_t, not just a restricted interval (e.g., above 2 GeV/c).

6.12 Comparisons of calculated pQCD fragment distributions and measured spectrum hard components

T. A. Trainor

Parton energy loss in a thermalized bulk medium is of central importance at RHIC. In some models the medium is opaque to most hard-scattered partons. But minijet systematics suggest no parton loss to thermalization. I adopt a pQCD-inspired minimal model of FF modification (Borghini-Wiedemann or BW) with no loss of scattered partons to a medium.

Fig. 6.12-1 (first panel) illustrates the BW model of fragmentation function (FF) modification. In-vacuum e-e FFs for $Q = 14$ and 200 GeV from a beta-function $\beta(u;p,q)$ parametrization are shown as dashed and solid curves respectively. FFs are plotted on fragment rapidity y. The energy scale is $Q = 2\,p_{jet}$. The BW "energy-loss" mechanism is essentially momentum-conserving rescaling of FFs on momentum fraction $x_p = p/p_{jet}$. Small density reductions at larger fragment momenta are compensated by much larger increases at smaller momenta. The largest changes (central Au-Au) correspond to an inferred 25% leading-parton fractional "energy loss." I model the BW modification simply by changing parameter q in $\beta(u;p,q)$ by $\Delta q \sim 1$, which accurately reproduces the BW result. The modified FFs are the dash-dotted and dotted curves. Fig. 6.12-1 (second panel) shows the modified e-e FF ensemble with FF modes shifted to smaller fragment rapidities. No energy is lost from FFs in this model.

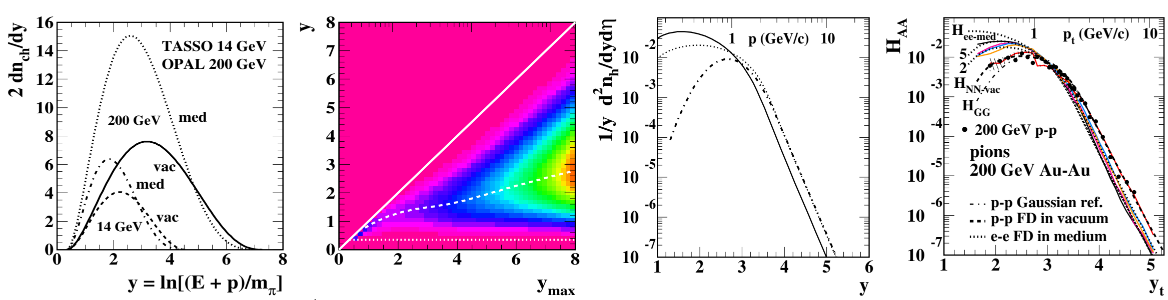

Figure 6.12-1. First: e^+-e^- FFs for two energies unmodified (solid and dashed curves) and modified (dash-dotted and dotted curves) to emulate parton "energy loss," Second: e^+-e^- FF ensemble modified as in the first panel, Third: Medium-modified FD from e^+-e^- FFs (solid curve) compared to in-vacuum e^+-e^- FD (dotted curve) Fourth: Hard-component evolution in central Au-Au collisions vs centrality with structure similar to the third panel.

Fig. 6.12-1 (third panel) shows H_{ee-med} (solid curve), the fragment distribution (FD) obtained by inserting e-e in-medium FFs from the second panel into the pQCD folding integral and integrating over parton rapidity y_{max}. The dotted curve is the H_{ee-vac} reference from in-vacuum e-e FFs. The dash-dotted curve is hard component reference function H_{GG} derived from p-p collisions. The mode of H_{ee-med} is ~ 0.3 GeV/c. Fig. 6.12-1 (fourth panel) shows data from p-p collisions (points) and from five centralities of Au-Au collisions at $\sqrt{s_{NN}} =$ 200 GeV (solid curves). Especially for the more-central collisions the data are well-described by the solid curve in the third panel obtained by folding a minimum-bias parton spectrum with measured e-e FFs altered by a simple medium modification scheme based on rescaling pQCD splitting functions. Spectrum hard components in p-p and Au-Au are theoretically described.

6.13 Good, bad and ugly ratio measures of fragmentation

T. A. Trainor

Spectrum ratios are used to measure deviations of parton fragmentation in A-A collisions from a reference system, conventionally p-p or d-Au collisions at RHIC. Two questions emerge: what is the validity of the ratio definition, and what should be the reference for such a ratio. The conventional spectrum ratio at RHIC is R_{AA}, defined at the left in

$$R_{AA} \equiv \frac{1}{\nu} \times \frac{S_{NN}(y_t) + \nu\, H_{AA}(y_t;\nu)}{S_{NN}(y_t) + H_{NN}(y_t)} \to \frac{1}{\nu} + \frac{H_{NN}}{S_{NN}} r_{AA} \quad \text{at} \quad y_t = 2. \tag{1}$$

The terms in numerator and denominator are normalized per participant pair $n_{part}/2$, so the prefactor is $1/\nu$ rather than $1/n_{binary}$. Fig. 6.13-1 (first panel) illustrates problems. Hard-component evolution with centrality, the object of analysis, is described by ratio $r_{AA} \equiv H_{AA}/H_{NN}$. The last term of Eq. (1) gives the limiting value of R_{AA} near $y_t \sim 2$ where the H_{NN}/S_{NN} ratio is typically $\sim 1/170$. r_{AA} is thus suppressed by a large factor in just the interval where fragmentation details are most important.

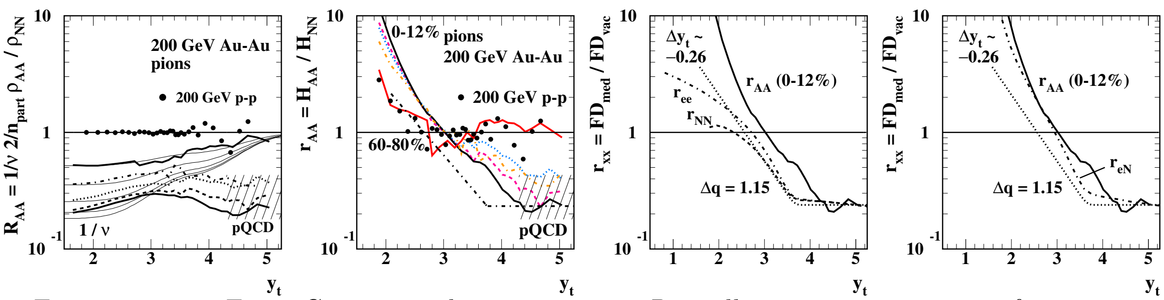

Figure 6.13-1. First: Conventional spectrum ratio R_{AA}, illustrating suppression of spectrum information below 4 GeV/c ($y_t = 4$), Second: Hard-component ratio r_{AA} illustrating restoration of suppressed structure at small y_t, Third: Comparison of measured r_{AA} for central Au-Au collisions (solid curve) to calculated FD ratios, Fourth: Comparison of novel FD ratio r_{eN} (dash-dotted curve) to measured r_{AA} for central Au-Au collisions.

Fig. 6.13-1 (second panel) shows alternative spectrum ratio r_{AA} defined with the hard components from the left panel. With soft component S_{NN} eliminated full access to hard-component centrality trends is evident. The 200 GeV p-p and 60-80% central Au-Au data fall on the reference (unity), and *sensitivity* to deviations from the reference is uniform over all y_t. Large-amplitude structure now appears at the left end of the spectra. Fig. 6.13-1 (third panel) shows calculated FD ratios $r_{xx} = FD_{xx-med}/FD_{xx-vac}$ with xx = e-e (dash-dotted curve, e-e FFs) or N-N (dashed curve, p-p FFs) compared to measured r_{AA} from central (0-12%) Au-Au collisions at 200 GeV(solid curve). Several aspects reveal that the references in these ratios are inappropriate. Fig. 6.13-1 (fourth panel) introduces a novel concept. The in-medium FD for e-e is compared with the in-vacuum FD for N-N by defining ratio

$$r_{eN} = \frac{FD_{ee-med}}{FD_{NN-vac}}. \tag{2}$$

Calculated r_{eN} describes the measured r_{AA} well over the entire fragment momentum range. We conclude that the proper in-vacuum reference for all systems is an FD from e-e FFs, not p-p FFs. Ratios for all fragment distributions are formed with reference FD_{ee-vac}.

6.14 Centrality evolution of fragment distributions and the sharp transition in jet angular correlations

T. A. Trainor

Fig. 6.14-1 (first panel) shows spectrum hard components (fragment distributions) H_{AA} (solid curves) for five centralities from 200 GeV Au-Au collisions which scale proportional to n_{binary}, as expected for parton scattering and fragmentation (jets). The points are hard-component data from 200 GeV p-p collisions. The dash-dotted curve is the standard p-p reference function $H_{\rm GG}$. Calculated pQCD fragment distributions (FDs) (dashed and dotted curves) compare well with data. Fig. 6.14-1 (second panel) shows spectrum ratios defined in terms of an e-e vacuum reference: H_{pp} (p-p data – points), H_{AA} (peripheral Au-Au data – solid curve) and pQCD calculated $H_{\text{ee-med}}$ (dash-dotted curve) and H_{NN-vac} (dashed curve) all divided by reference H_{ee-vac}. The strong suppression of p-p and peripheral Au-Au data apparent at smaller y_t results from the low-y_t suppression of p-p FFs noted elsewhere.

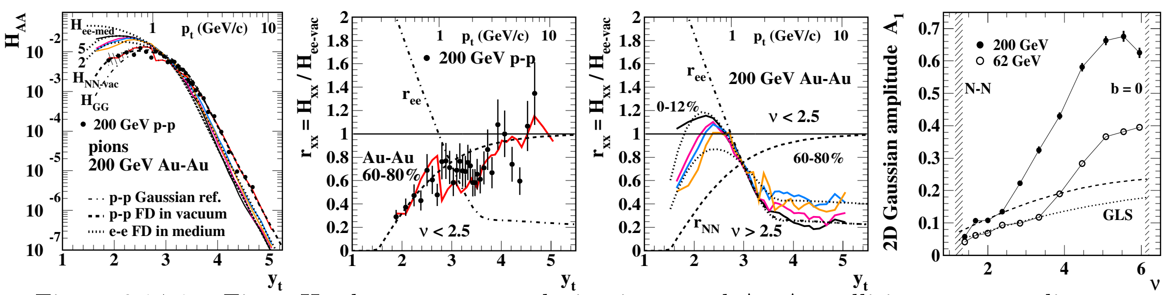

Figure 6.14-1. First: Hard-component evolution in central Au-Au collisions vs centrality. Large increases in fragment yield at smaller y_t accompany suppression at large y_t. Second: FD ratios relative to an ee-vacuum reference for Au-Au collisions below the sharp transition, Third: FD ratios relative to an ee-vacuum reference for Au-Au collisions above the sharp transition revealing major changes in FD structure, Fourth: Jet peak amplitude vs Au-Au centrality revealing a sharp transition from Glauber linear superposition (GLS).

Fig. 6.14-1 (third panel) shows measured $H_{\rm AA}/H_{\text{ee-vac}}$ for more-central Au-Au collisions (solid curves) above a transition point on centrality at $\nu \sim 2.5$. The main difference is partial restoration of the suppressed region at smaller y_t and suppression at larger y_t. The latter has been the major observation at RHIC for jet-related modification (high-p_t suppression, "jet quenching"). Newly apparent from this analysis is the accompanying very large *increase* in fragment yield *below* 2 GeV/c, still strongly correlated with the parent parton. Also notable is the substantial gap between the peripheral data and the four more-central spectra. Changes in fragmentation depend very strongly on centrality near the transition point. It is remarkable that the trend at 10 GeV/c corresponds closely to the trend at 0.5 GeV/c.

Fig. 6.14-1 (fourth panel) shows complementary structure in two-particle angular correlations. The points record the same-side (SS) jet peak amplitude for eleven Au-Au centralities and two energies. Glauber linear superposition trends (dashed and dotted curves) are expected for N-N physics only. The sharp transition to rapid increase of jet yields (at $\nu = 2.4$ at 200 GeV) reveals novel jet physics in more-central collisions. The correspondence between spectrum hard-component trends in the center panels and jet angular correlations is notable.

6.15 Periodicity effects and jet-structure modeling on azimuth

T. A. Trainor

Particle distributions on azimuth are periodic. Jet peaks (nominally Gaussian) at 0 (SS, same-side) and π (AS, away-side) are elements of periodic arrays. The SS array is centered on *even* multiples of π, the AS array on *odd* multiples. Nearby elements of an array outside a 2π interval can have a significant effect on distributions and should be included in fit models. A peak array (SS or AS) can be represented by a Fourier series of the form

$$S(\Delta\phi; \sigma_{\Delta\phi}, n) \;=\; A_{0,n} + A_{1,n}\{1 + \cos(\Delta\phi - n\,\pi)\}/2 + \sum_{m=2}^{\infty} A_{m,n}\,\cos(m\,[\Delta\phi - n\,\pi]), \quad (1)$$

where the $A_{m,n}$ are functions of Gaussian width $\sigma_{\Delta\phi}$, n is even for SS peak arrays (+), and odd for AS arrays (−). Terms represent multipoles: dipole ($m = 1$), quadrupole ($m = 2$), sextupole ($m = 3$). As peak width $\sigma_{\Delta\phi}$ increases the number of terms in the series decreases. If $\sigma_{\Delta\phi} \sim \pi/2$ the peak array is approximated by a constant plus single dipole term.

Fig. 6.15-1 (first panel) shows peak arrays (solid points) for SS and AS peaks. The SS Gaussian peak array is the dash-dotted curve, the AS array is the dashed curve (pure dipole). The dotted curve is the SS quadrupole term which would add a large "nonflow" contribution to $v_2^2\{2\}$. Fig. 6.15-1 (second panel) shows the Fourier amplitudes of a Gaussian peak for five terms of Eq. (1) as functions of the peak width. For $\sigma_{\Delta\phi} \sim \pi/2$ only the constant and dipole terms contribute. For narrower peaks terms with $m > 1$ become significant.

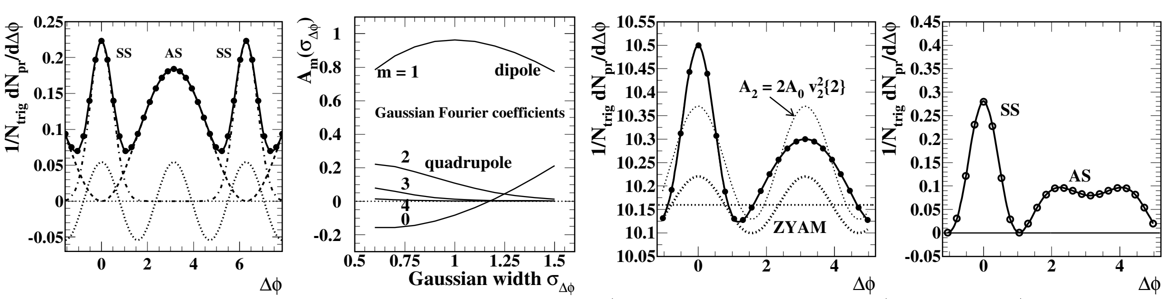

Figure 6.15-1. First: Periodic arrays of SS (same-side, dash-dotted) and AS (away-side, dashed) peaks. The SS peaks are Gaussians. The AS peaks are well-described by a dipole. The dotted sinusoid is the $m = 2$ Fourier component of the SS peaks. Second: Fourier amplitudes A_m of a Gaussian [Eq. (1)] vs peak width Third: Simulated "raw" (unsubtracted) dihadron correlations (solid dots), azimuth quadrupole amplitude A_2 with corresponding sinusoid (light dotted curve) and ZYAM subtracted background (bold dotted curve). Fourth: Result of ZYAM background subtraction in the third panel. The minimum at π in the AS (away-side) peak is notable.

Fig. 6.15-1 (third panel) illustrates ZYAM (zero yield at minimum) subtraction. The points simulate a measured pair distribution R. The light dotted curve represents "elliptic flow" $v_2^2\{2\}$ obtained by fitting the entire distribution. The bold dotted curve is background B, with $v_2^2 = v_2^2\{2\}/2$ and constant B_0 adjusted so that "jet" correlations $S = R - B$ satisfy ZYAM. Fig. 6.15-1 (fourth panel) shows S as the points. The "raw" jet component has been substantially reduced in amplitude, and the AS peak has a minimum at π. That is the general form of dihadron correlations for more-central A-A collisions after ZYAM subtraction.

6.16 The ZYAM prescription and underestimation of jet yields at RHIC

T. A. Trainor

Fig. 6.16-1 (first panel) shows simulated azimuth correlation data (points) for central ($b = 0$) Au-Au collisions. The distribution consists of SS Gaussian and AS dipole only. A fit to unsubtracted data using a Gaussian+dipole+quadrupole+constant model (solid curve) returns the simulation parameters. A fit to the distribution with $A_0 + A_2 \cos(2\Delta\phi)$ only (dotted curve) corresponds to $A_2 \equiv 2A_0\, v_2^2\{2\} = 0.12 \simeq P_2/4$ by definition of $v_2^2\{2\}$. Fig. 6.16-1 (second panel) shows the result of ZYAM subtraction as the points. The dash-dotted and dashed curves show the simulation input, the "right answer." The bold solid curve through the points is a free fit with the SS Gaussian+AS dipole+quadrupole model. The original parameters are returned in addition to the ZYAM-imposed v_2^2 and offset. No information is lost by the ZYAM subtraction, but the result is visually misleading. The v_2^2 oversubtraction results in a minimum in the AS peak, and the ZYAM offset subtraction imposes a large reduction in apparent jet yields.

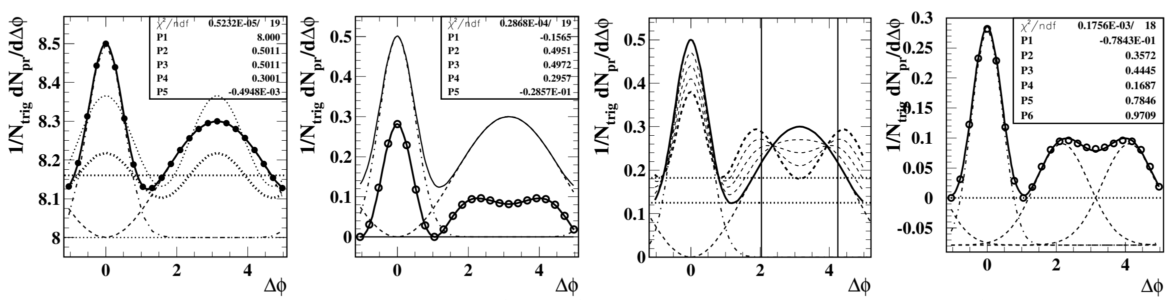

Figure 6.16-1. First: Simulated data (points) with ZYAM background model (bold dotted curve). Second: Result of subtracting ZYAM background model from simulated data (points). The bold solid curve is a free fit to the subtracted data which returns the original SS Gaussian and AS dipole model parameters plus the ZYAM offset and quadrupole parameters. Third: Demonstration of the effects of v_2 oversubtraction. Model jet correlations are the "data" (solid curve) from which quadrupole components of successively larger amplitudes are subtracted (dashed curves). Dotted lines represent zero levels established according to the ZYAM principle. Vertical solid reference lines are at $\pi \pm 1.1$. Fourth: ZYAM-subtracted distribution fitted with single SS Gaussian and two AS Gaussians located symmetrically about π. Common AS Gaussian amplitudes and widths are P4 and P5. Displacements from π are P6.

Fig. 6.16-1 (third panel) demonstrates that maxima near $\Delta\phi \approx \pi \pm 1$ resulting from ZYAM subtraction are an inevitable consequence of v_2 oversubtraction for typical angular correlations from RHIC collisions. Several values of A_2 (integer multiples of $2A_0\, v_2^2 = 0.015$) including zero (solid curve) are invoked in the subtraction. The persistence of apparently-displaced peaks at the same locations is evident. Note the effect of ZYAM subtraction even for $v_2^2 = 0$ (solid curve and dotted line). Fig. 6.16-1 (fourth panel) illustrates attempts to characterize the AS peak structure with two Gaussians. Nominal medium-induced "shoulder" Gaussians are located near $\Delta\phi \approx \pi \pm 1$. In some cases a fragmentation-related "head" Gaussian is introduced at $\Delta\phi = \pi$. The bold solid curve is a free fit with shoulder Gaussians allowed to vary in centroid, width and amplitude, but symmetrically about $\Delta\phi = \pi$.

6.17 Recovering valid jet structure – two RHIC case studies

T. A. Trainor

A combination of ZYAM (zero yield at minimum) offset estimates and v_2 oversubtraction can result in substantial underestimation of jet yields in more-central RHIC A-A collisions. With free model fits it is possible to reverse the analysis bias to recover the true jet yields. Fig. 6.17-1 (first panel) shows data from 200 GeV 0-12% central Au-Au collisions for (trigger×associated) 4-6×0.15-4 GeV/c p_t cuts (solid points). Corresponding p-p data are shown as open circles. The bold solid curve is a free fit with offset (P1), SS Gaussian (amplitude P2, width P3), AS dipole (P4) and quadrupole (P5). The resulting offset is the solid line at P_1, the SS Gaussian is the dash-dotted curve, the dipole is the dashed curve, and the (negative) quadrupole is the dotted curve. Fig. 6.17-1 (second panel) shows a reconstruction of the original ("raw") data distribution prior to ZYAM subtraction based on P_1 and P_5. The relation of p-p to central Au-Au data is quite different. Both SS and AS peaks *increase by a factor six* from p-p to central Au-Au, a large increase in the jet yield which is not apparent in the first panel.

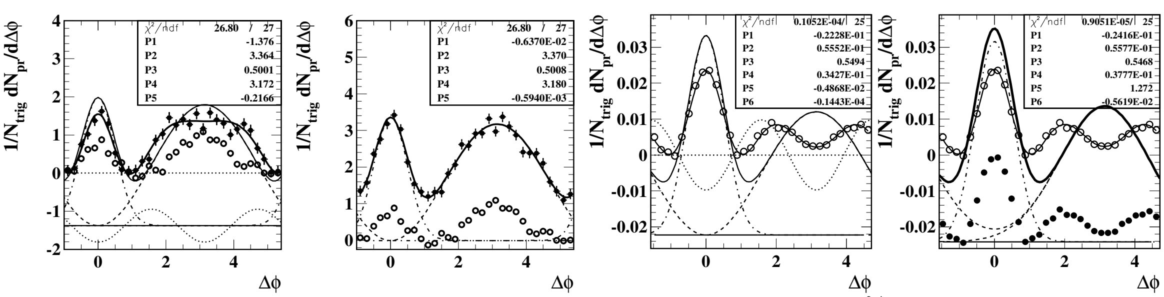

Figure 6.17-1. First: ZYAM-subtracted angular correlations for 0-12% central 200 GeV Au-Au collisions (solid points). Open points are p-p data relative to ZYAM zero. Second: ZYAM subtraction reversed, true zero level recovered from free fits to data (solid points), compared to p-p data (open symbols). Third: ZYAM-subtracted correlation data (open circles). Fourth: The same data fitted with SS Gaussian (P2, P3), AS Gaussian (P4, P5) and quadrupole (P6), leading to equivalent results. The solid points are the open points translated by offset P_1.

Fig. 6.17-1 (third panel) shows ZYAM-subtracted azimuth correlation data corresponding to 2-3×2-3 GeV/c p_t cuts. The data are from 0-5% central Au-Au collisions at $\sqrt{s_{NN}} =$ 200 GeV. The bold solid curve is a free fit with offset (P1), SS Gaussian (amplitude P2, width P3) and away-side Fourier series (dipole P4, quadrupole P5, sextupole P6). The dash-dotted curve is the fitted SS Gaussian, the dashed curve is the fitted dipole, and the dotted curve is the fitted negative quadrupole. Fig. 6.17-1 (fourth panel) shows a fit replacing the AS Fourier series with an AS Gaussian (amplitude P4, width P5) plus quadrupole (P6), which describes the data equally well. The SS peak parameters are the same in the two panels. The free fit recovers the correct AS jet structure and background offset. Fig. 6.17-1 (right panels) reveals that the increase in the SS peak yield over ZYAM subtraction is $(0.056 \times 0.55)/(0.024 \times 0.3) \sim 4$, and the increase in the AS yield is $(0.038 \times 1.3)/(2 \times 0.008 \times 0.3) \sim 10$. The increase can be appreciated visually in the right panel by comparing the solid points to the bold solid curve. Again, jet yields are strongly suppressed by conventional ZYAM and v_2 subtraction.

6.18 Relativistic heavy ion physics-analysis of pionic interferometry: the DWEF model

J. G. Cramer, G. A. Miller* and M. Luzum †

We have continued our work on developing a dynamic model to explain puzzling aspects of RHIC data, using the *ansatz* that the medium through which emitted pions must pass in RHIC collisions is opaque rather than transparent and that the pion may lose mass in that medium through chiral symmetry restoration[1]. We model this opacity with a pion relativistic optical model, formulated in the Bjorken Tube geometry of a RHIC heavy ion collision. We have been able to extend the model to non central collisions and obtain excellent agreement with central and non-central 200 GeV/A HBT data taken with the STAR detector for Au+Au and Cu+Cu collisions at RHIC.

Recently we have found and fixed convergence and coding problems with the original program. These corrections have required refitting of the 200 GeV/A STAR HBT and spectrum data. The main conclusions of our original work were not changed by these revisions and refits, but the source temperature to obtained optimum data fits has decreased from about 193 MeV (a rather high temperature that is about the expected temperature of a chiral phase transition) to 168 MeV (a more reasonable temperature that is about that of chemical freeze-out of the system), making our model more plausible, since it is only looking back and tracking pion evolution from chemical freeze-out.

We have also investigated in more detail the use of optical potentials in the regime of ultra-relativistic heavy ion collisions[2]. We find that if the optical potential is real, the standard formalism is modified as described in our previous work. However, if the optical potential is complex, a new term involving pion emission from eliminated states must be included. We presently know of no way of precisely evaluating this term, but we can estimate its size. In the context of our previous work, the new term appears to be of the same order of magnitude as the terms evaluated. In an effort to assess the importance of this phenomenon, we have re-fitted the STAR data wit a purely real potential, so that the extra term is zero. The resulting fits are slightly worse in reproducing the slope of the pion specturm and the R_{out}/R_{side} ratio, and we find that the fit parameters change significantly, with the emission temperature dropping from about 160 MeV to 120 MeV and the emission duration time dropping to 0. This indicates that in our model, either the final state interactions occur in the later times of the collision and that the emission occurs at only one proper time, or that the inclusion of emission terms from the states eliminated in the construction of the complex optical potential is necessary.

---

*supported by the UW Nuclear Theory DOE Contract

†UW Nuclear Theory Grad. Student

[1] "Polishing the lens: I. Pionic final state interactions and HBT correlations: distorted wave emission-function (DWEF) formalism and examples", Gerald A. Miller and John G. Cramer, J. Phys. G: Nucl. Part. Phys. **34** 703 (2007).

[2] "Understanding the Optical Potential in HBT Interferometry", Matthew Luzum, John G. Cramer, and Gerald A. Miller, Phys. Rev. C **78** 054905 (2008).

7 Electronics, Computing, and Detector Infrastructure

7.1 Electronic equipment

A. W. Myers, and T. D. Van Wechel

The electronics shop is responsible for the design and construction of new laboratory electronic equipment, as well as the maintenance and repair of existing CENPA electronics. Projects undertaken by the electronics shop included the following:

1. The development of a pulsed reset preamp (see Sec. 7.2) for the MAJORANA experiment has been the most significant design project this year. The design is now complete. Initial tests will commence as soon as construction of the first prototype is completed.

2. An optically isolated femtoammeter was developed for the determination of the efficiency of the KATRIN Si multi pixel focal-plane detector (see Sec. 1.12).

3. An 8 channel RTD temperature sensor to ADC interface board was developed for the KATRIN experiment.

4. A multi-channel controller for high voltage power supplies for MAJORANA was developed.

5. Designed and constructed a raster trigger module for the ^{22}Na experiment.

6. New equipment was acquired to support the manufacture of the pulse reset amplifier (see Sec. 7.2) front end boards. This included a wire bonding machine, a die bonding machine and a parylene deposition system.

7.2 Pulsed reset preamp for MAJORANA

A. W. Myers, R. G.H. Robertson, and T. D. Van Wechel

A pulsed reset preamp is currently being developed for MAJORANA. MAJORANA will make use of p-type point-contact (PPC) detectors, perhaps of the existing Canberra BEGe design. The low capacitance of the contact and the modest drift fields make low-noise, high-resolution spectroscopy and pulse-shape analysis possible. Additional physics goals beyond neutrinoless double beta decay motivate an effort to reduce the noise threshold to the extent possible.

A goal is to have the entire preamp front end mounted as near to the detector as possible. It is customary to put the FET and feedback components close to the detector and at a similar temperature, with the second stage at a distance and at a different temperature. However, there are advantages in closing the loop close to the detector. It is easier to assure high-speed response and the phase stability of the amplifier is easier to control with the short feedback line. Preamp radiopurity is another concern. This obviates the use of higher value capacitors such as bypass capacitors since the dielectrics tend to be hot.

Charge sensitive amplifiers have a capacitor as the feedback element. Leakage currents, as well as ionizing events, will charge the feedback capacitor until the amplifier's output limit is reached. Some means of resetting or removing the charge from the feedback capacitor is necessary, the most common method being a high value resistor in parallel with the feedback capacitor, also providing DC feedback to stabilize the DC operating point. The disadvantage of the resistive feedback is that it is a source of 'parallel' Johnson noise, with a contribution that has the same frequency spectrum as the shot noise due to detector (and FET) leakage current. A resistor that is too small will be noisier than the shot noise, making it impossible to reach the ultimate resolution of which the detector itself is capable. For comparison, a 52-G resistor produces the same noise as 1 pA of leakage current.

A pulse reset preamplifier has only a capacitor for feedback. Periodic resets, or discharges of the feedback capacitor, are required. Several schemes have been devised over the years, including the following:

1. Pulsed Optical Reset where a flash of light from an LED illuminates the FET and creates charge carriers in the depletion region of the gate-channel junction, which discharges the capacitor.
2. Transistor Reset where a transistor is connected to the FET gate and is switched on to discharge the capacitance.
3. Reset Pulse through the Detector, where a reset pulse is applied to the biased side of the detector.
4. Pulsed-Drain Reset, where a negative pulse is applied to the drain, to forward-bias the drain-gate junction.
5. Pulsed-Source Reset, where a negative pulse is applied to the source, to forward bias

the source-gate junction. This method is the subject of the Jordanov patent[1] and is used in some of Canberra's pulse reset preamps.

6. Reset Pulse applied through the feedback capacitor, where a reset pulse is applied at the output side of the feedback capacitor.

7. Special 4-terminal FET devices with a second gate for reset.

We have investigated and simulated several of the above reset methods. By simulation we determined that some methods such as the reset pulse applied through the detector or the feedback capacitor work well, but are impractical in our case because relatively large amplitude voltage pulses are required when the detector capacitance or feedback is small. This is because the total capacitance at the input of the preamplifier has to be charged through the low value feedback capacitor or detector capacitance, before the source-gate junction can be forward-biased to reset the feedback capacitor. We settled on a variation of the source pulse reset method for our design.

The preamp is divided into two sections, a front end board, and a reset control and interface board. The front end board is mounted at the detector and has the FET, the second stage op-amp, feedback capacitor, the current steering diodes for applying the reset signal to the FET source, and heater diodes. The reset control electronics and the interface electronics to the DAQ electronics are on the other board, which is mounted outside of the cryostat. The interconnecting signal and power wires are twisted-pair wires with deposited parylene insulation. They are terminated in the characteristic impedance of the twisted pair, at the reset control and interface board. Since one of the goals is to avoid high value capacitors on the front end board, power is applied through a twisted pair terminated and bypassed at the far end. When simulated this worked better than expected; we will soon see if it works in practice when the first prototype is completed.

The reset control and interface board provides a differential receiver, buffers, DC blocking with a 50 μs time constant, and two channels of output with different gains. The reset signal is initiated and terminated by comparators and is dispatched to the preamp after a 100 μs delay. Provision for a global reset in a multiple-detector system has been made. The front end board is thermally connected to the same temperature as the detector, which may be too cold for the operation of the electronics, and so a temperature regulation circuit for the front end board is on the reset board.

A low cost U440 FET will be used for the prototype tests. Based on Spice simulations the expected resolution for the U440 FET with a detector capacitance of 1 pF, and a shaping timing of 0.5 uS should be 406 eV FWHM, and at a shaping time of 10 uS should be 92 eV FWHM for a detector with no leakage or 106 eV FWHM for a detector leakage of 1 pA. Eventually we plan on using a Moxtek MX-120 FET. For the MX-120 FET, the simulations predict that for a 0.5 uS shaping time a resolution of 121 eV FWHM, and for a shaping time of 10 uS a resolution of 38 eV FWHM for a detector with no leakage, or 64 eV FWHM for a detector leakage of 1 pA.

[1] Valentin T. Jordanov, US Patent 6,587,003 B2, July 1, 2003.

7.3 Data acquisition development for the MAJORANA experiment

M. A. Howe*, M. G. Marino, M. L. Miller, J. Orrell†, and J. F. Wilkerson*

The MAJORANA experiment plans to use low-capacitance, low-noise germanium detectors which will extend the sensitivity of the experiment to energies below 1 keV. Fast digitizers will be used to record signals in the MAJORANA experiment enabling post-processing to extract event characteristics such as energy and event topology. The experiment will use the Gretina Mark IV digitizer card, a 100 MS/s, 14 bit, VME-based digitizer being developed at Lawrence Berkeley Laboratory. Additional characteristics of this card were reported earlier[1].

Recent work has progressed to analyze the effectiveness of the Gretina card to acquire low-amplitude signals ∼0.1 mV. Two different triggering methods have been explored, one using an un-shaped signal triggered directly by the leading-edge discrimination (LED) of the digitizer, the other using a signal shaped by an analog spectroscopy amplifier input to the digitizer to generate a trigger with the Gretina card LED. In the latter case, two channels are used: one channel with analog shaped input for triggering, the other channel with un-shaped input for digitization.

Efficiency of the triggers was tested using a set of pulses of amplitudes which scanned across the noise threshold. The amplitude of each pulse is given in units of the full-width-half-maximum (FWHM) of the noise. Results are presented for each trigger case (Fig. 7.3-1). We found that triggering on the analog shaped pulse allowed a far better efficiency much closer to the noise. Work is planned to investigate modifying the digital triggering algorithms to achieve performance comparable to or better than triggering on an analog shaped pulse.

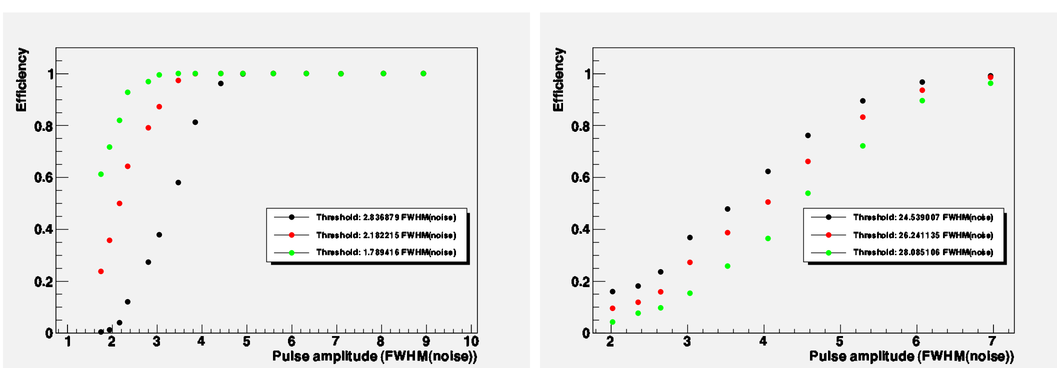

Figure 7.3-1. (left) Triggering on shaped pulses. (right) Triggering on un-shaped pulses. Pulse amplitudes and trigger thresholds are in units of FWHM of the noise.

*Currently at the University of North Carolina
†At Pacific Northwest National Lab
[1]CENPA Annual Report, University of Washington (2008) p. 27.

7.4 Laboratory computer systems

R. C. Coffey*, M. A. Howe†, R. J. Seymour, H. E. Swanson, N. R. Tolich, J. F. Wilkerson† and D. I. Will

We are a mixed shop of Windows XP, Vista, Mac OS X and various flavors of Linux. Windows Vista is being installed on new systems, but we are predominantly running Windows XP Pro. We have three shared-usage Fedora-based systems, one hosting our 6.5 TB RAID farm. We are now staging all daily Linux and Windows backups through one third of that system, from whence they are written to LTO tape by the Physics Computer Center. One of the other Fedora hosts is holding a terabyte drive for archival backups.

This year we upgraded the building's network in two stages: first by providing gigabit ethernet to all building wired sockets. That entailed replacing a hodge-podge of small 8 and 16-port 10/100 and 10/100/1000 switches with three 48-port and two 24-port D-Link DGS-1248T and 1224T. We then replaced a ten-year old 10/100 HP800 switch serving as our primary link to the campus with a ten gigabit-capable D-Link DXS-3227. Then the campus network folks installed a ten gigabit fiber to that DXS-3227, and added another to service the Athena cluster. Most of our "heavy" computation has shifted to the Athena cluster (see Sec. 7.5), although most of our usage has been as "single machines" instead of making maximum use of the cluster's parallel architecture.

Our computing and analysis facility consists of:

- The 140-node, 1120-core Athena cluster as a shared resource with Physics, the Institute for Nuclear Theory (INT) and Astronomy Department.
- A mix of Linux systems, RedHat v7.3 through v9.0 and Fedora Cores 6 through 10
- Three VMS/MicroVaxes and two VMS Alphas for "legacy" computing.
- The SNO, NCD, KATRIN, Majorana and emiT groups rely upon Macintosh systems.
- One SunBlade 100 workstation serves CADENCE circuit design, analysis and layout duties.
- A VAXstation is the Linac and Vacuum systems' control and display system.
- Various WindowsXP desktop JAM acquisition and analysis systems, plus two laptops for taking to other installations.
- The bulk of CENPA's Windows-based PCs are behind a Gibraltar Linux-based logical firewall using an automated setup procedure developed by Corey Satten, previously of the University's Networks and Distributed Computing group. http://staff.washington.edu/corey/fw/
- Although not directly used by Lab personnel, we provide additional legacy co-location services for the INT and the Physics Nuclear Theory group in the form of one VMS Alphastation 500. The Astronomy Department has located a 64-processor Xeon-based Beowulf cluster in our old "counting" room.

---

*UW Physics Department

†Presently at the University of North Carolina

7.5 Athena: a high end computing deployment for scientific computing

R. Coffey, J. Garder, D. B. Kaplan, M. L. Miller, T. Quinn, R. J. Seymour, D. I. Will

Initiated by Co-Investigators D. Kaplan and T. Quinn, Athena[1] is a high end computing (HEC) cluster, hosted at CENPA, for use within Physics, Astronomy, and Computer Science. The cluster supports high performance scientific computing applications that cannot be efficiently executed on typical commodity server infrastructures (e.g., the Amazon EC2 Cloud). The current Athena configuration consists of 140 machines linked together by a high speed InfiniBand network fabric, 1.23 TB of RAM, and 23.7 TB of high rate shared storage. The peak performance of the system is greater than 10 TeraFlops. Access to the computing nodes is controlled via the PBS job submission application. Aside from the raw horsepower mentioned above, the Athena cluster's key differentiating characteristic is the InfiniBand interconnect ($\sim$80 Gbs communication between any two nodes) which radically outpaces the traditional 1 Gbs ethernet connections used in a typical data center, allowing for seamless integration of parallel methods such as MPI into application design and execution.

The cluster has already proven to be an invaluable resource for local researches. A full list of publications is available online.[2] Notable uses of the cluster in the last year include:

- Providing the 5x speedup that the SNO collaboration needed to perform an emergency reprocessing of the Phase-3 data to meet conference and publication deadlines.[3]
- Integrating MPI into an existing C++ application to perform massively parallel analytic calculations of the EM fields in the KATRIN spectrometer.
- Simulations of new detector configurations for the rapidly evolving MAJORANA project.
- Computing the interactions of 2- and 3-baryons using lattice QCD.
- Simulating structure formation in the early universe.
- Searching for systematic patterns in the masses of medium and heavy nuclei.
- Rapid prototyping and benchmarking of existing parallel data management solutions (Hadoop, PIG, etc.) leading to a deadline driven, inter-disciplenary eScience proposal to build a custom Database Management System for HEC applications.

The common theme in these examples is that access to similar architectures at national computing facilities would have introduced prohibitively high bureaucratic overhead and scheduling latencies for completion of the aforementioned projects.

[1]http://librarian.phys.washington.edu/athena/index.php/
[2]http://physoffice.phys.washington.edu/athenapreprint/display/view.aspx
[3]B. Aharmim *et al.*, Phys. Rev. Letters **101**, 111301 (2008).

7.6 Linux driver development for VME-based single-board computers

M. A. Howe*, M. G. Marino, and J. F. Wilkerson*

Embedded computers (single-board computers or SBCs) directly resident on a bus maximize the functionality of that bus by providing fast data access to installed peripherals. An SBC running a Linux-based operating system allows for fast software development time. In many VME-based SBC systems, the Tundra Universe II chip provides bus translation to enable reads across the PCI bus to access the VME bus. This article presents development of an open-source Linux driver (kernel version ≥ 2.6) for Universe II chips.

The driver makes full use of PCI device functions provided by the Linux 2.6 kernel, maximizing portability of the driver across different hardware configurations. Additionally, the driver supports memory mapping and interrupt-based direct memory access (DMA) for fast data transfers with minimal CPU usage across the VME bus. Access to the Universe II device can be obtained directly through char device files or through the provided Application Programming Interface (API).

The Linux driver resides in kernel space, but provides both a C and C++ based Application Programming Interface (API) for simple integration into single or multi-threaded user programs such as the one used to interface with the ORCA DAQ software[1]. An example of the usage of API is provided below:

```
#include "universe_api.h"
// Obtain a device
TUVMEDevice* aDevice = get_new_device( /* base VME address */     0x0,
                                       /* VME Address Modifier */ 0x29,
                                       /* Data size (bytes) */    2,
                                       /* VME add. window size */ 0x10000 );
// Read from device
int32_t bytes_read = read_device( /* Device */                aDevice,
                                  /* (char*) */               buffer,
                                  /* Bytes to read */         numBytes,
                                  /* Offset from base add. */ offset );
// Close Device
close_device( aDevice );
...
// Get DMA Device
TUVMEDevice* dmaDevice = get_dma_device( /* base VME address */     0xFF00,
                                         /* VME Address Modifier */ 0xB,
                                         /* Data size (bytes) */    4,
                                         /* auto-increment add. */  true );
// Read DMA device
read_device( dmaDevice, buffer, 0xFFFF, 0 );
```

*Currently at the University of North Carolina

[1] CENPA Annual Report, University of Washington (2008) p. 82.

7.7 Drift filter for difference measurements - understanding the errors

S. Schlamminger, H. E. Swanson

AB difference measurements can be expressed as a time series of x_i where the quantity of interest δ changes sign with each measurement. x_0 is an additive background term that may vary with i. δ can be recovered by calculating the mean of the N data points $x_i \times (-1)^i$.

$$x_i = x_o(i) + (-1)^i \delta \tag{1}$$

The problem is that the mean and its variance may also have contributions from the varying background. We can write an expression for a linear combination of these x_is that cancels drifts for all orders less than some number p.

$$y_i(p) = \frac{1}{2^p} \sum_{k=0}^{p} (-1)^{i+k} \left(\begin{array}{c} p \\ k \end{array} \right) x_{i+k} \tag{2}$$

where $\left(\begin{array}{c} p \\ k \end{array} \right)$ is a binomial coefficient. When this filter is applied sequentially to all x_is there are $N - p$ new degrees of freedom and the mean of these y_is yields δ directly. The y_is are correlated with each other so to compute the variance we need to construct the full covariance matrix and sum all its terms. Fig. 7.7-1 shows the error costs that result from applying the filter compared with just taking differences. For example the solid curve labled $(p = 3)$ gives the increase in error that results from applying the filter to cancel linear and quadratic drifts.

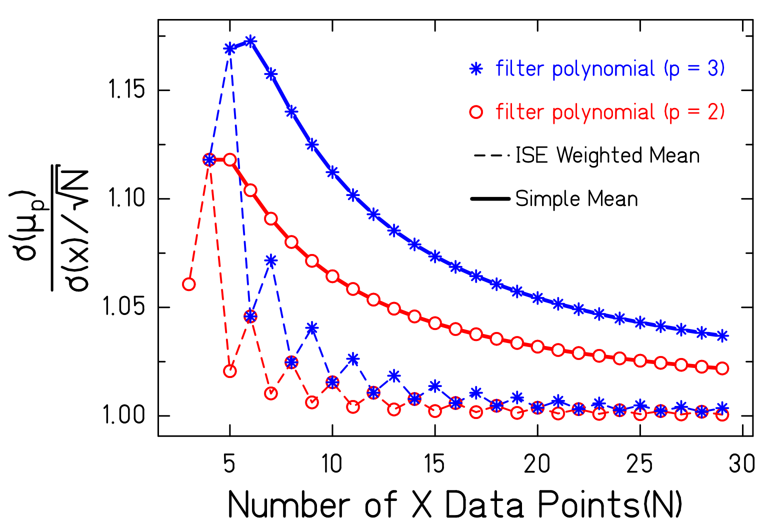

Figure 7.7-1. The figure shows the additional uncertainty in the mean that results from applying the filter to N data points. $\sigma(x)$ is the error in each x. The circles are for the linear only filter and the asterisks for the linear plus quadratic filter. The points connected by solid lines show the uniformly weighted mean and those by dashed lines are for the inverse square error weighted mean.

The filter weights the x_is at the beginning and end of the time series less than those values in the middle. The corresponding y_is are correlated with fewer terms and thus they have on average smaller errors. The simple mean is appropriate when the points are all drawn from the same distribution. In this case where the errors are different it makes sense to use an inverse square error (ISE) weighting. We have developed a formalism for doing this using the inverse covariance matrix. The plot shows the resulting uncertainty in an ISE weighted mean by points connected with dashed lines. For most values of N the error of this ISE weighted mean is significantly less than for the uniformly weighted mean. The errors are smallest when the number of data points N has the same evenness or oddness as the number of terms in the filter expression.

One can think of this in terms of efficiency as in how many measurement values does it take to achieve a desired uncertainty. The smallest statistical error is obtained taking only differences so this would require the least number of measurements. In this case however one has the added uncertainty of the drift systematic. Applying a filter removes drift from consideration but incurs a cost of increasing the statistical uncertainty. It is a much more efficient use of the N data points if the filtered points are weighted by the inverse square of their errors.

7.8 Characterization of the version 3 IPE crate and optimization of the onboard trapezoidal filter

T. Bergman*, D. Horning†, A. Kopmann*, M. L. Leber, M. G. Marino, and J. F. Wilkerson‡

The requirements for KATRIN's data acquisition system (DAQ) are to process signals from 148 silicon PIN diode channels and 8 scintillator channels, handle data rates from mHz to MHz, and tag coincidences between channels. The solution is a custom DAQ crate designed by KATRIN collaborators at the Institut für Prozessdatenverarbeitung und Elektronik (IPE). The version 3 IPE crate's energy resolution and dead time have been tested at CENPA. A digital pulser programmed with detector-like pulses was used for testing.

The IPE crate input is continuously digitized and filtered by an onboard trapezoidal filter. A pulse is readout if the filtered pulse is above threshold. Initially, poor energy was observed with the IPE crate. A software trapezoidal filter was written as an exact replica of the filter implemented onboard the IPE crate, and the filter parameters were optimized. The rise time of detector pulses was longer than the gap in the trapezoidal filter, creating tails in the energy spectrum. By increasing the filter gap length, the energy resolution was improved. The detector pulses have a fall time of 100 μs, much longer than the 3.2 μs filter length. The IPE crate does not account for the fall time of the pulse by using a pole-zero correction. In the software filter, a pole-zero correction was implemented, increasing the energy resolution by 16%. Although the improvement is minimal, this pole zero correction may be implemented into the Version 4 IPE crate.

To test the dead time, a random pulser was used to trigger a fast square pulse. Using detector-like pulses was not possible because the pulser will only output a single pulse at a time, so it introduced an inherent dead time. The IPE crate has three modes to handle the large range of rates: waveform, event, and histogram modes. In waveform mode, the entire digitized pulse is read out, along with peak height and timing information, causing the largest dead time. This mode is only used for debugging. In event mode, the pulse height and timing of each event is read out. To achieve the lowest dead time, in histogramming mode the pulse heights are stored in a histogram onboard the crate, and all timing information is lost. Every few seconds the histogram is read out. Using the random pulser, we verified that the histogramming mode reads out 100% of events up to 50 kHz, although some histograms are read out twice. This is due to the buffers not being cleared, a bug that will be fixed. In event mode, up to 7 kHz can be read out with zero dead time.

In conclusion, tests of the Version 3 IPE crate have been designed and carried out. Similar tests will be needed for the final version of the crate. Additionally, the trapezoidal filter has been verified with a software version.

*Forschungszentrum Karlsruhe, Institut für Experimentelle Kernphysik, Postfach 3640, 76021 Karlsruhe, Germany.

†Entering undergraduate student, Yale

‡University of North Carolina, Chapel Hill, NC

8 Accelerator and ion sources

8.1 Van de Graaff accelerator and ion source operations and development

N. A. Gillgren, G. C. Harper, A. W. Myers, T. D. Van Wechel, D. I. Will

The tandem was entered four times this year. Two parallel connected gas bottles of $^1H_2$ were either installed or refilled during three of the tank openings. The internal TIS parts which had survived a record 3000 hours were replaced during one opening. Tandem column shorting balls had been disturbed during one opening, probably when the column was bumped when exiting the tank. This required a subsequent opening during which the accelerator tube gradient was repaired by restoring two of the column shorting balls to their correct locations. During one opening the spark bars at the chain pulleys at both the low energy and high energy ends were moved out to reduce corona of the charging system at low tank pressures.

This year modifications were made to the DEIS to produce positive ion beams of the noble gases ^{4}He, ^{20}Ne, ^{36}Ar, and ^{40}Ar for subsequent implantation. These modifications are discussed elsewhere in this annual report (see Sec. 8.2). This year, for the first time, the SpIS was used for implantations of ^{113}In.

During the 12 months from April 1, 2008 to March 31, 2009 the tandem pellet chains operated 1569 hours, the SpIS operated 967 hours, and the DEIS operated 193 hours. Additional statistics of accelerator operations are given in Table 8.1-1.

ACTIVITY SCHEDULED	**DAYS SCHEDULED**	**PERCENT of AVAILABLE TIME**
Ion implantation, deck ion sources	60	16
Nuclear physics research, terminal ion source	139	38
Subtotal, ion implant or nuclear physics research	199	54
Machine development, maintenance, or crew training	48	13
Grand total	246	67

Table 8.1-1. Tandem Accelerator Operations April 1, 2008 to March 31, 2009

8.2 Modification of the DEIS and injector deck for noble gas ion implantation

N. A. Gillgren, G. C. Harper, D. W. Storm, D. I. Will

This year requests were made for implants of the noble gases ^{20}Ne and ^{36}Ar. The negative ions of the noble gases are unstable and so cannot be formed in the ion sources as they are set up on the injector platform. The initial plan was to use the terminal ion source to produce the positive ion, accelerate it to the lowest reasonable tandem energy, and use stopper foils at the target to slow it to about 30 keV. This approach would have required modifications to the tandem, testing the terminal ion source with neon and argon, and modifying an existing experimental beamline to accept the stopper foils. Testing the terminal ion source with neon and argon would have involved several tank openings. An idea to use the direct extraction source (DEIS) on the injector deck was instead proposed.

The duoplasmatron in the DEIS can produce copius amounts (up to 1 mA) of positive ion beam current from a variety of gases. In fact, a section of the small halo of negative ions around the hot core of positive ions is what is extracted to produce the negative ion beams from the DEIS. There are two advantages to using the DEIS to produce the ion beams. The implantation setup already exists right off of the accelerator tube from the injector deck and all modifications can be done without a tank entry. To use the DEIS to produce positive beams a few things had to be changed.

For the extraction voltage we installed a +60 kV surplus supply that could deliver 20 mA and plugged it into the interlocked AC outlet. We used the DEIS HV cable identifier key to complete the interlock loop. The DEIS focus electrode voltage was taken from a Glassman −10 kV, 15 mA supply dedicated to the sputter source (SpIS) in the high voltage rack. The high current cables to the analyzing magnet were reversed. The einzel lenses on deck and off deck are both set up in decel/accel mode to provide strong focussing for negative ion beams. They simply had to be operated at a higher voltage in the weaker accel/decel mode for positive ion beams. The Keithley meter output repeater amps are unipolar so the positive ion beam current could only be read locally, not remotely. The plasma bottle aperture in the DEIS is offset from the beam axis by about 0.5 mm to locate the negative ion sheath over the ion source aperture. This facilitates the extraction of negative ions. For extracting positive ions we moved the plasma bottle aperture back onto the ion beam axis. To elevate the deck, the +50 kV, 3 mA gridded lens supply was disconnected from the gridded lens and attached to the injector deck in place of the −300 kV, 1 mA supply.

We tested with helium which has the highest ionization potential of all of the noble gases. We were able to produce ion beams of ^{4}He^{+} with intensities of 20 μA to 40 μA in the 20 keV to 50 keV range. Offdeck, with the additional acceleration, we were able to get about 20 μA of 100 keV ^{4}He^{+}. Neon proved to be the most prolific with beam intensities of ^{20}Ne^{+} as high as 60 μA observed with an extraction voltage of +50 kV. We were able to produce about 40 μA of ^{40}Ar^{+} with the correct isotopic fractions of 0.33% ^{36}Ar^{+} and 0.063% ^{38}Ar^{+} present and observed. The 130 nA of ^{36}Ar^{+} was considered adequate to do a reasonable implantation of the rare isotope.

9 Status of the Career Development Organization

L. Bodine, R. A. Johnson, M. L. Leber, M. G. Marino, N. S. Oblath, and B. L. Wall

The Career Development Organization has successfully completed its ninth year and continues to be led by CENPA students. The eighth annual Networking Day was well received. Twenty eight students participated, giving talks, posters, and lab tours. As in previous years, almost all of the past CDO presidents were in attendance, mostly as employer representatives. Four national labs attended in addition to five international companies.

Given the success in previous years, we again held an employer talk session providing potential employers with an opportunity to present to students. Additionally, a resume workshop focused on physics and astronomy graduate students was given by UW's Career Services. The employer talk session was open to all students and enjoyed a strong attendance. As always, the website lists information about students and employers participating in Networking Day. Links to job listings and resources for students looking for employment are also available. The CDO website houses all this information and is available at `http://students.washington.edu/cdophys/`.

In addition to Networking Day, the CDO organizes lab tours, speakers, and informational meetings for grad students. Plans to invite local companies from the spring quarter are underway. Officers of the CDO gain valuable leadership experience and many contacts outside the University. The continuity of Networking Day has strengthened our contacts and visibility. Past CDO presidents have maintained their commitment to CDO by attending as employers, and their organizations benefit from this support. CENPA has always supported the CDO with storage space, office supplies, and donated printing. Planning for next year's Networking Day has already begun.

10 CENPA Personnel

10.1 Faculty

Eric G. Adelberger[1]	Professor Emeritus
Hans Bichsel[1]	Affiliate Professor
John G. Cramer	Professor
Peter J. Doe	Research Professor
Alejandro García	Professor
Jens H. Gundlach[1]	Professor
Blayne R. Heckel[1]	Professor
Michael L. Miller	Research Assistant Professor; CENPA Fellow
R. G. Hamish Robertson	Professor; Director
Leslie J. Rosenberg[1]	Professor
Stephan Schlamminger[1]	Research Assistant Professor
Kurt A. Snover[1]	Research Professor Emeritus
Derek W. Storm[1]	Research Professor Emeritus
Nikolai R. Tolich	Assistant Professor
Thomas A. Trainor	Research Professor
Robert Vandenbosch[1]	Professor Emeritus
William G. Weitkamp[1]	Research Professor Emeritus
John F. Wilkerson[2]	Professor

10.2 CENPA External Advisory Committee

Baha Balantekin	University of Wisconsin
Stuart Freedman	UC Berkeley
William Zajc	Columbia University

[1]Not supported by DOE CENPA grant.
[2]Departed January 2009; Faculty, University of North Carolina

10.3 Postdoctoral Research Associates

Thomas Brown[1]	Jessica Dunmore[2]
Frank Fleischer[3,4]	Seth Hoedl
Jarek Kaspar	Gray Rybka[3]
Kazumi Tolich	Brent VanDevender
Hok Wan Chan Tseung[3]	Chris Wrede

10.4 Predoctoral Research Associates

Laura Bodine	Ted Cook[3]
G. Adam Cox-Mobrand[5]	Ian Derrington[3]
Charles Hagedorn[3]	Michael Hotz[3]
Robert Johnson	David Kettler
Michelle Leber	Michael Marino
Eric Martin	Erik Mohrmann[6]
Noah Oblath	Pascal Renschler[7]
Anne Sallaska	Alexis Schubert
Sky Sjue[8]	William Terrano[3]
Matthew Turner[3]	Grant Volle[3]
Todd Wagner[3]	Brandon Wall
Brett Wolfe	David Zumwalt

10.5 Non-RA graduate students taking research credit

Daniel Scislowski	Nikolai Tolich, Advisor

10.6 NSF Research Experience for Undergraduates participants

Alex Cunliffe	Northwestern University
Jessica McIver	Syracuse University

[1]Departed March 2009; Patent Examiner
[2]Departed July 2008; Faculty, West Point Military Academy
[3]Not supported by DOE CENPA grant.
[4]Feodor Lynen Fellow
[5]Ph.D., January, 2008. Faculty, DigiPen Institute, Redmond, WA.
[6]Ph.D., August, 2008. Faculty, DigiPen Institute, Redmond, WA.
[7]Visiting Graduate Student, University of Karlsruhe.
[8]Ph.D., October, 2008. Postdoctoral Fellow, TRIUMF.

10.7 University of Washington undergraduates taking research credit

Jennie Chen	Blayne Heckel, Advisor
Kseniya Deryckx	A. García, Advisor
Matthew Haefele	Ted Cook, Advisor
William Norton Haycox	Michael Miller, Advisor
Holly Hess	Eric Adelberger, Seth Hoedl, Advisors
Chantelle Jacques	Nikolai Tolich, Advisor
Marianne Knauer[1]	Peter Doe, Advisor
Eric Lee-Wong	Blayne Heckel, Advisor
John Mower	Nikolai Tolich, Advisor
Evan Nelson	Michael Miller, Brent VanDevender, Advisors
Andrew Palmer	A. García, Advisor
Natalie Ann Ramien	Nikolai Tolich, Advisor
Carin Schlimmer	Stephan Schlamminger, Advisor
Cosmo Smith	Brent VanDevender, Advisor
Elizabeth Waldren	Nikolai Tolich, Advisor
Elizabeth Weiss[2]	Peter Doe, Advisor
Thomas Wolowiec	Leslie Rosenberg, Advisor

10.8 Professional staff

The professional staff are listed with a description of their recent major efforts.

John F. Amsbaugh	Research Engineer	KATRIN vacuum systems
Tom H. Burritt	Research Engineer	Design of KATRIN detector system
Gregory C. Harper	Research Engineer[3]	Electronic and mechanical design
Mark A. Howe[4]	Research Engineer	Software for DAQ, control systems
Allan Myers	Research Engineer	Electronic fabrication
Duncan J. Prindle, Ph.D.	Research Scientist	Heavy ion software
Richard J. Seymour	Computer Systems Manager	
Hendrik Simons	Instrument Maker, Shop Supervisor	
H. Erik Swanson, Ph.D.	Research Physicist	Precision experimental equipment
Timothy D. Van Wechel	Electronics Engineer	Analog and digital electronics design
Douglas I. Will	Research Engineer	Cryogenics, ion sources

[1]Intern, Berufsakademie Karlsruhe.
[2]Intern, Berufsakademie Mannheim.
[3]CENPA Associate Director with effect from April 2009.
[4]Departed August 2008.

10.9 Technical staff

James Elms	Instrument Maker
David Hyde	Instrument Maker

10.10 Administrative staff

Victoria A. Clarkson	Administrator
Kate J. Higgins	Fiscal Specialist

10.11 Part time staff and student helpers

Nora Boyd
James Geier[1]
Nathaniel Gillgren
Donna Horning[2]
Eugene Ngai
Ahn Ngo
Cosmo Smith

[1] Departed August 2008.
[2] Entering undergraduate student, Yale

11 Publications

Publications and presentations with a date of 2008 or 2009 are included below. Some entries from early 2008 may therefore also appear in the 2008 Annual Report.

11.1 Published papers

"Independent measurement of the total active ^{8}B solar neutrino flux using an array of ^{3}He proportional counters for the Sudbury Neutrino Observatory," B. Aharmim and the SNO Collaborators,* Phys. Rev. Lett. **101**, 111301 (2008).

"Experimental constraints on a dark matter origin for the DAMA annual modulation effect," C. E. Aalseth, P. S. Barbeau, D. G. Cerdeno, J. Colaresi, J. I. Collar, P. de Lurgio, G. Drake, J. E. Fast, C. H Greenberg, T. W. Hossbach, J. D. Kephart, M. G. Marino, H. S. Miley, J. L. Orrell, D. Reyna, R. G. H. Robertson, R. Talaga, O. Tench, T. D. Van Wechel, J. F. Wilkerson and K. M. Yocum, Phys. Rev. Lett. **101**, 251301 (2008) asXiv:0807.0879vl [astro-ph].

"Improved limit on the permanent electric dipole moment of ^{199}Hg," W. C. Griffith, M. D. Swallows, T. H. Loftus, M. V. Romalis, B R. Heckel and E N. Fortson, Phys. Rev. Lett. **102**, 101601 (2009).

"Preferred-frame and CP-violation tests with polarized electrons," B. R. Heckel, E. G. Adelberger, C. E. Cramer, T. S. Cook, S. Schlamminger and U. Schmidt, Phys. Rev. **D 78**, 092006 (2008).

"Torsion balance experiments: a low-energy frontier of particle physics," E. G. Adelberger, J. H. Gundlach, B. R. Heckel, S. Hoedl and S. Schlamminger, Progress in Particle and Nuclear Physics **62**, 102 (2009).

"Temporal extent of surface potentials between closely spaced metals," J. H. Gundlach, S. E. Pollack and S. Schlamminger, Phys. Rev. Lett. **101**, No. 7, 071101 (2008).

"The KamLAND full-volume calibration system," B. E. Berger and the KamLAND Collaborators,* (2009) arXiv:0903.0441vl [physics.ins-det].

"Longitudinal double-spin asymmetry for inclusive jet production in polarized p+p collisions at $\sqrt{s} = 200$ GeV," B. I. Abelev and the STAR collaborators,* Phys. Rev. Lett. **100**, 232003 (2008).

"Beam-energy and system-size dependence of dynamical net charge fluctuations," B. I. Abelev and the STAR collaborators,* Phys. Rev. C **79**, 0204906 (2009).

"System-size independence of directed flow at the relativistic heavy-ion collider," B. I. Abelev and the STAR collaborators,* Phys. Rev. Lett. **101**, 252301 (2008).

"Indications of conical emission of charged hadrons at RHIC," B. I. Abelev and the STAR collaborators,* Phys. Rev. Lett. **102**, 052302 (2009).

"Centrality dependence of charged hadron and strange hadron elliptic flow from $\sqrt{s} = 200$ GeV Au+Au collisions," B. I. Abelev and the STAR collaborators,* Phys. Rev. C **77**, 054901 (2008).

"Ft-value of the $0^+ \rightarrow 0^+$ decay of ^{32}Ar: a measurement of isospin symmetry breaking in a super-allowed decay," M. Bhattacharya, D. Melconian, A. Komives, S. Triambak, A. García, E. G. Adelberger, B. A. Brown, M. W. Cooper, T. Glasmacher, V. Guimaraes, P. F. Mantica, A. M. Oros-Pesquens, J. I. Prisciandaro, M. Steiner, H. E. Swanson, S. L. Tabor and M. Wiedeking, Phys. Rev. C **77**, 065503 (2008).

"Electron-capture branch of ^{100}Tc and tests of nuclear wave functions for double-β decays," S. K. L. Sjue, D. Melconian, A. García, I. Ahmad, A. Algora, J.Äystö, V.-V. Elomaa, T. Eronen, J. Hakala, S. A. Hoedl, A. Kankainen, T. Kessler, I. D. Moore, F. Naab, H. Penttilä, S. Rahaman, A. Saastamoinen, H. E. Swanson, C. Weber, S. Triambak and K. Deryckx, Phys. Rev. C **78**, 064317 (2008).

"Limits on Scalar Currents from the $0^+ \rightarrow 0^+$ decay of ^{32}Ar and Isospin Breaking in ^{33}Cl and ^{32}Cl," A. García, Proceedings of the 4th ANL/MSU/INT/JINA RIA Theory Workshop, Proceedings from the Institute for Nuclear Theory - Vol. 16, WorldScientific, (2008).

"First Measurement of the Neutron β-Asymmetry with Ultracold Neutrons," R. W. Pattie Jr., J. Anaya, H. O. Back, J. G. Boissevain, T. J. Bowles, L. J. Broussard, R. Carr, D. J. Clark, S. Currie, S. Du, B. W. Filippone, P. Geltenbort, A. García, A. Hawari, K. P. Hickerson, R. Hill, M. Hino, S. A. Hoedl, G. E. Hogan, A. T. Holley, T. M. Ito, T. Kawai, K. Kirch, S. Kitagaki, S. K. Lamoreaux, C.-Y. Liu, J. Liu, M. Makela, R. R. Mammei, J. W. Martin, D. Melconian, N. Meier, M. P. Mendenhall, C. L. Morris, R. Mortensen, A. Pichlmaier, M. L. Pitt, B. Plaster, J. C. Ramsey, R. Rios, K. Sabourov, A. Sallaska, A. Saunders, R. Schmid, S. Seestrom, C. Servicky, S. K. L. Sjue, D. Smith, W. E. Sondheim, E. Tatar, W. Teasdale, C. Terai, B. Tipton, M. Utsuro, R. B. Vogelaar, B. W. Wehring, Y. P. Xu, A. R. Young and J. Yuan (The UCNA Collaboration) Phys. Rev. Lett. **102**, 012301 (2009).

"Thermonuclear $^{25}\mathrm{Al}(p,\gamma)^{26}$Si reaction rate in classical novae and Galactic ^{26}Al," C. Wrede, Phys. Rev. C 79, 035803 (2009).

"Nuclear Structure Relevant to Neutrinoless Double β Decay: the Valence Protons in ^{76}Ge and ^{76}Se," B. P. Kay, J. P. Schiffer, S. J. Freeman, T. Adachi, J. A. Clark, C. M. Deibel, H. Fujita, P. Grabmayr, H. Hatanaka, D. Ishikawa, H. Matsubara, Y. Meada, H. Okamura, K. E. Rehm, Y. Sakemi, Y. Shimizu, H. Shimoda, K. Suda, Y. Tameshige, A. Tamii and C. Wrede, Phys. Rev. C **79**, 021301(R)(2009).

"A determination of the proton separation energy of ^{93}Rh from mass measurements," J. Fallis, J. A. Clark, K. S. Sharma, G. Savard, F. Buchinger, S. Caldwell, J. E. Crawford, C. Deibel, S. Gulick, A. A. Hecht, D. Lascar, J. K. P. Lee, A. F. Levand, G. Li, B. F. Lundgren, A. Parikh, S. Russell, M. Scholte-van de Vorst, N. D. Scielzo, R. E. Segel, S. Sinha, M. Sternberg, T. Sun, J. Van Schelt, I. Tanihata, J. C. Wang, Y. Wang, C. Wrede and Z. Zhou, Phys. Rev. C **78**, 022801(R) (2008).

"Addendum to 'Measurement of ^{23}Mg$(p,\gamma)^{24}$Al resonance energies'," D. W. Visser, C. Wrede, J. A. Caggiano, J. A. Clark, C. Deibel, R. Lewis, A. Parikh and P. D. Parker, and Phys. Rev. C **78**, 028802 (2008).

"Nuclear Structure Relevant to Neutrinoless Double β Decay: ^{76}Ge and ^{76}Se," J. P. Schiffer, S. J. Freeman, J. A. Clark, C. Deibel, C. R. Fitzpatrick, S. Gros, A. Heinz, D. Hirata, C. L. Jiang, B. P. Kay, A. Parikh, P. D. Parker, K. E. Rehm, X. D. Tang, A. C. C. Villari, V. Werner and C. Wrede, Phys. Rev. Lett. **100**, 112501 (2008).

"High-j single-particle neutron states outside the $N = 82$ core," B. P. Kay, S. J. Freeman, J. P. Schiffer J. A. Clark, C. Deibel, A. Heinz, A. Parikh, P. D. Parker, K. E. Rehm, and C. Wrede, Phys. Lett. B **658**, 216 (2008).

"Azimuth quadrupole component spectra on transverse rapidity $\mathbf{y_t}$ for identified hadrons from Au-Au collisions at $\sqrt{s_{NN}} = 200$ GeV," T. A. Trainor, Phys. Rev. C **78**, 064908 (2008), arXiv:0803.4002.

"Centrality evolution of p_t and y_t spectra from Au-Au collisions at $\sqrt{s_{NN}} = 200$ GeV," T. A. Trainor, Int. J. Mod. Phys. E **17**, 1499 (2008), arXiv:0710.4504.

"The azimuth structure of nuclear collisions – I," T. A. Trainor and D. T. Kettler, Int. J. Mod. Phys. E **17**, 1219 (2008), arXiv:0704.1674.

"Understanding the Optical Potential in HBT Interferometry," M. Luzum, J. G. Cramer and G. A. Miller, Phys. Rev. C **78**, 054905 (2008), arXiv:0809.0520.

"Centrality dependence of charged hadron and strange hadron elliptic flow from $\sqrt{s_{NN}} = 200$ GeV Au+Au collisions," B. I. Abelev and the STAR collaborators,* Phys. Rev. C **77**, 54901 (2008), arXiv:0801.3466.

"Forward Neutral Pion Transverse Single Spin Asymmetries in p+p Collisions at $\sqrt{s} = 200$ GeV," B. I. Abelev and the STAR collaborators,* Phys. Rev. Lett. **101**, 222001 (2008), arXiv:0801.2990.

"Spin alignment measurements of the K* and phi vector meson at RHIC," B. I. Abelev and the STAR collaborators,* Phys. Rev. C **77**, 61902 (2008), arXiv:0801.1729.

"Hadronic resonance production in d+Au collisions at 200 GeV at RHIC," B. I. Abelev and the STAR collaborators,* Phys. Rev. C **78**, 44906 (2008), arXiv:0801.0450.

"ρ^0 Photoproduction in Ultra-Peripheral Relativistic Heavy Ion Collisions with STAR," B. I. Abelev and the STAR collaborators,* Phys. Rev. C **77**, 34910 (2008), arXiv:0712.3320.

"Longitudinal double-spin asymmetry for inclusive jet production in $\vec{p}+\vec{p}$ collisions at $\sqrt{s}$=200 GeV," B. I. Abelev and the STAR collaborators,* Phys. Rev. Lett. **100**, 232003 (2008), arXiv:0710.2048.

"Enhanced strange baryon production in Au+Au collisions compared to p+p at $\sqrt{s_{NN}} = 200$ GeV," B. I. Abelev and the STAR collaborators,* Phys. Rev. C **77**, 44908 (2008), arXiv:0705.2511.

"Observation of Two-source Interference in the Photoproduction Reaction $AuAu \rightarrow AuAu\rho^0$," B. I. Abelev and the STAR collaborators,* Phys. Rev. Lett. **102**, 112301 (2009), arXiv:0812.1063.

"Energy and system size dependence of ϕ meson production in Cu+Cu and Au+Au collisions," B. I. Abelev and the STAR collaborators,* Phys. Lett. B **673**, 183-191, (2009), arXiv:0810.4979.

"Beam-Energy and System-Size Dependence of Dynamical Net Charge," B. I. Abelev and the STAR collaborators,* Phys. Rev. C **79**, 024906 (2009), arXiv:0807.3269.

"Systematic Measurements of Identified Particle Spectra in pp, d+Au and Au+Au Collisions from STAR," B. I. Abelev and the STAR collaborators,* Phys. Rev. C **79**, 034909 (2009), arXiv:0808.2041.

"Indications of Conical Emission of Charged Hadrons at RHIC," B. I. Abelev and the STAR collaborators,* Phys. Rev. Lett. **102**, 052302 (2009), arXiv:0805.0622.

"Energy dependence of phi meson production in central Pb+Pb collisions at $s_{NN}^{1/2} = 6$ to 17 GeV," C. Alt and the NA49 collaborators,* Phys. Rev. C **78**, 044907 (2008), arXiv:0806.1937 [nucl-ex].

"Energy dependence of Lambda and Xi production in central Pb+Pb collisions at A-20, A-30, A-40, A-80, and A-158 GeV measured at the CERN Super Proton Synchrotron," C. Alt and the NA49 collaborators,* Phys. Rev. C **78**, 034918 (2008).

"Measurements of ^{31}S energy levels and reevaluation of the thermonuclear resonant ^{30}P$(p,\gamma)^{31}$S reaction rate," C. Wrede, J. A. Caggiano, J. A. Clark, C. M. Deibel, A. Parikh and P. D. Parker, Phys. Rev. C **79**, 045803 (2009).

"Thermonuclear ^{30}S$(p,\gamma)^{31}$Cl reaction in type I x-ray bursts," C. Wrede, J. A. Caggiano, J. A. Clark, C. M. Deibel, A. Parikh and P. D. Parker, Phys. Rev. C. **79**, 045808 (2009).

"Test of the Equivalence Principle Using a Rotating Torsion Balance," S. Schlamminger, K.-Y. Choi, T. A. Wagner, J. H. Gundlach and E. G. Adelberger, Phys. Rev. Lett. **100**, 041101 (2008).

“The Apache Point Observatory Lunar Laser-ranging Operation: Instrument Description and First Detections,” T. W. Murphy, Jr., E. G. Adelberger, J. B. R. Battat, L. N. Carey, C. D. Hoyle, P. LeBlanc, E. L. Michelsen, K. Nordtvedt, A E. Orin, J. D. Strasburg, C. W. Stubbs, H. E. Swanson, and E. Williams, Pub. Astr. Soc. Pacific **120**, 20 (2008).

“Preferred-Frame and CP-Violation Tests with Polarized Electrons,” B. R. Heckel, E. G. Adelberger, C. E. Cramer, T. S. Cook, and S. Schlamminger, Phys. Rev. D **78**, 092006 (2008).

“Torsion Balance Experiments: A Low-energy Frontier of Particle Physics,” E. G. Adelberger, J. H. Gundlach, B. R. Heckel, S. Hoedl and S. Schlamminger, Progress in Particle and Nuclear Physics **62**, 102 (2009).

“The Apache Point Observatory Lunar Laser-ranging Operation (APOLLO): Two Years of Millimeter-Precision Measurements of the Earth-Moon Range,” J. B. R. Battat, T. W. Murphy, Jr., E. G. Adelberger, B. Gillespie, C. D. Hoyle, R. R. McMillan, K. Nordtvedt, A. E. Orin, C. W. Stubbs, and H. E. Swanson, Pub. Astr. Soc. Pacific **121**, 29 (2009).

11.2 Papers submitted or to be published 2009

“Measurement of the cosmic ray and neutrino-induced muon flux at the Sudbury Neutrino Observatory,” B. Aharmim and the SNO Collaborators,* submitted for publication to Phys. Rev. D, arXiv:0902.2776 [hep-ex].

“Characterization of Thin-Foil Ultracold Neutron Detectors,” A. García, S. P. Geltenbort, A. Hoedl, A. T. Holley, D. Melconian, A. L. Sallaska, S. K. L. Sjue and A. R. Young, accepted for publication in Nucl. Inst. and Meth. A.

“Determination of Gamow-Teller Strength for ^{40}Ar $\rightarrow^{40}$ K,” M. Bhattacharya, C. D. Goodman and A. García, submitted for publication to Phys. Rev. C.

“Properties of ^{23}Na implanted targets,” T. A. D. Brown, K. Deryckx, A. García, A. L. Sallaska, K. A. Snover, D. W. Storm and C. Wrede, submitted for publication to Nucl. Inst. and Meth. B.

“Mass measurements of proton-rich nuclides from Nb to Rh along the νp- and rp-process paths performed with the Canadian Penning Trap mass spectrometer,” J. Fallis, J. A. Clark, K. S. Sharma, G. Savard, F. Buchinger, S. Caldwell, A. Chaudhuri, J. E. Crawford, C. Deibel, S. Gulick, A. A. Hecht, D. Lascar, J. K. P. Lee, A. F. Levand, G. Li, B. F. Lundgren, A. Parikh, S. Russell, M. Scholte-van de Vorst, N. D. Scielzo, R. E. Segel, H. Sharma, S. Sinha, M. Sternberg, T. Sun, I. Tanihata, J. Van Schelt, J. C. Wang, Y. Wang, C. Wrede and Z. Zhou,” in preparation for Eur. Phys. J. A.

“Towards an experimentally determined ^{26m}Al$(p,\gamma)^{27}$Si reaction rate in ONe novae,” C. M. Deibel, J. A. Clark, R. Lewis, A. Parikh, P. D. Parker and C. Wrede, March, 2009, submitted for publication to Phys. Rev. C.

“Measurement of ^{23}Mg+p resonance energies,” C. Wrede, D. W. Visser, J. A. Caggiano, J. A. Clark, C. Deibel, R. Lewis, A. Parikh and P. D. Parker, accepted for publication in Proceedings of Science.

“First measurement of the ^{31}P(^{3}He,t)^{31}S reaction: a study of the thermonuclear ^{30}P$(p,\gamma)^{31}$S reaction rate,” C. Wrede, J. A. Caggiano, J. A. Clark, C. Deibel, A. Parikh and P. D. Parker, accepted for publication in Proceedings of Science.

“The ^{26m}Al$(p,\gamma)^{27}$Si Reaction Rate in ONe Novae,” C. M. Deibel, J. A. Clark, R. Lewis, A. Parikh, P. D. Parker and C. Wrede, accepted for publication in Proceedings of Science.

“Study of Astrophysically Important Resonant States in ^{30}S Using the ^{32}S$(p,t)^{30}$S Reaction,” K. Setoodehnia, A. A. Chen, J. A. Clark, C. M. Deibel, D. Kahl, P. D. Parker, and C. Wrede, accepted for publication in Proceedings of Science.

“Evolution of minimum-bias parton fragmentation in nuclear collisions,” T. A. Trainor, submitted for publication to Phys. Rev. C, arXiv:0901.3387.

“ZYAM and $\mathbf{v_2}$: Underestimating jet yields from dihadron azimuth correlations,” T. A. Trainor, submitted for publication to Phys. Rev. C, arXiv:0904.1733.

“Measurements of ϕ meson production in relativistic heavy-ion collisions at RHIC,” B. I. Abelev and the STAR collaborators,* September, 2008, submitted for publication to Phys. Rev. C, arXiv:0809.4737.

“System-size independence of directed flow at the Relativistic Heavy-Ion Collider,” B. I. Abelev and the STAR collaborators,* July, 2008, submitted for publication to Phys. Rev. Lett., arXiv:0807.1518v2.

“Charge Independent(CI) and Charge Dependent(CD) correlations as a function of Centrality formed from $\Delta\phi\Delta\eta$ Charged Pair Correlations in Minimum Bias Au+Au Collisions at 200 GeV,” B. I. Abelev and the STAR collaborators,* June, 2008, submitted for publication to Phys. Rev. C, arXiv:0806.0513.

“Charmed hadron production at low transverse momentum in Au+Au collisions at RHIC,” B. I. Abelev and the STAR collaborators,* May, 2008, submitted for publication to Phys. Rev. Lett., arXiv:0805.0364.

“System size dependence of associated yields in hadron-triggered jets,” B. I. Abelev and the STAR collaborators,* April, 2009, submitted for publication to Phys. Rev. C, arXiv:0904.1722.

"J/psi production at high transverse momentum in p+p and Cu+Cu collisions at $\sqrt{s_{NN}} = 200$ GeV," B. I. Abelev and the STAR collaborators,* April, 2009, submitted for publication to Phys. Rev. Lett., arXiv:0904.0439.

"Pion Interferometry in Au+Au and Cu+Cu Collisions at RHIC," B. I. Abelev and the STAR collaborators,* March, 2009, submitted for publication to Phys. Rev. C, arXiv:0903.1296.

"K/pi Fluctuations at Relativistic Energies," B. I. Abelev and the STAR collaborators,* January, 2009, submitted for publication to Phys. Rev. Lett., arXiv:0901.1795v1.

"Measurement of D* Mesons in Jets from p+p Collisions at $\sqrt{s} = 200$ GeV," B. I. Abelev and the STAR collaborators,* January, 2009, submitted for publication to Phys. Rev. Lett., arXiv:0901.0740.

"The Energy Dependence of Transverse Momentum Fluctuations in Pb+Pb Collisions at CERN SPS," T. Anticic and the NA49 collaborators,* October, 2008, submitted for publication to Phys. Rev. C, arXiv:0810.5580.

"Three-Dimensional two-pion source image from Pb+Pb Collisions at $s_{NN}^{1/2} = 17.3$ GeV: New constraints for source breakup dynamics," C. Alt and the NA49 collaborators,* September, 2008, submitted for publication to Phys. Rev. Lett., arXiv::0809.1445 [nucl-ex].

"Energy dependence of particle ratio fluctuations in central Pb + Pb collisions from $s_{NN}^{1/2} = 6.3$-GeV to 17.3-GeV," C. Alt and the NA49 collaborators,* August, 2008, submitted for publication to Phys. Rev. Lett., arXiv:0808.1237 [nucl-ex].

11.3 Book Publications

"Faster-than-Light Implications of Quantum Entanglement and Nonlocality," John G. Cramer, Chapter 16 of *Frontiers of Propulsion Science*, Eds. Marc G. Millis and Eric W. Davis, American Institute of Aeronautics and Astronautics (2009), ISBN-10: 1-56347-956-7, ISBN-13: 978-1-56347-956-4.

"The Transactional Interpretation of Quantum Mechanics," John G. Cramer, book chapter published in *Compendium of Quantum Physics: Concepts, Experiments, History, and Philosophy*, Eds. Daniel Greenberger, Klaus Hentschel and Friedel Weinert, Springer-Verlag Berlin Heidelberg (2009), ISBN 978-3-540-70622-9.

11.4 Invited talks, abstracts and other conference presentations

"Experimental determination of neutrino mass," R. G. H. Robertson, Focus Meeting on Neutrinos, Institute for Physics and Mathematics of the Universe, Kashiwa, Japan, March, 2008.

"Report on the third and final phase of the Sudbury Neutrino Observatory," R. G. H. Robertson, in Proc. International Conference on Neutrino Physics and Astrophysics "Neutrinos 2008," Christchurch, New Zealand, May, 2008.

"Direct determination of neutrino mass," R. G. H. Robertson, in Proc. Caroline International Symposium on Neutrino Physics (CISNP), Columbia, SC, May, 2008.

"Neutrinos: particles with maddeningly few properties," R. G. H. Robertson, APS DNP Meeting, Oakland, CA, October, 2008.

"Neutrino physics for the masses," R. G. H. Robertson, Colloquium, Michigan State University, East Lansing, MI, February, 2009.

"Neutrino physics for the masses," R. G. H. Robertson, Colloquium, University of Chicago, Chicago, IL, February, 2009.

"Neutrino physics for the masses," R. G. H. Robertson, Colloquium, University of Victoria, Victoria, British Columbia, Canada, April, 2009.

"New results from a search for the electric dipole moment of ^{199}Hg," B. R. Heckel, Colloquium, University of Chicago, Chicago, IL, March, 2009.

"New results from a search for the electric dipole moment of ^{199}Hg," B. R. Heckel, Colloquium, Argonne National Laboratory, Argonne, IL, March, 2009.

"A high precision test of the equivalence of inertial and gravitational mass," S. Schlamminger, Art Institute, Seattle, WA, May, 2008.

"Measurement of the gravitational constant with a mass comparator," S. Schlamminger, CPEM, Broomsfield, CO, June, 2008.

"A high precision test of the equivalence of inertial and gravitational mass," S. Schlamminger, NRC-INMS, Ottawa, CA, December, 2008.

"Weighing the neutrino," B. A. VanDevender, Postdoctoral Association Annual Research Symposium, University of Washington, Seattle, WA, November, 2008.

"The next pieces in the puzzle of mass," M. L. Miller, Particle Physics Colloquium, University of California, San Diego, CA, April, 2008.

"The next pieces in the puzzle of mass," M. L. Miller, CENPA Colloquium, University of Washington, Seattle, WA, July, 2008.

"Precision determination of some correlations in nuclear beta decay," A. García, *Low Energy Precision Electroweak Physics in the LHC Era* program at the Seattle Institute for Nuclear Theory, Seattle, WA, November, 2008.

" Scalar currents and isospin breaking in ^{32}Ar decay," A. García, University of Jyväskylä, Finland, March, 2008.

"Isospin breaking and searches for scalar currents in ^{32}Ar decay," A. García, National Superconducting Laboratory at Michigan State University, East Lansing, MI, April, 2008.

"Isospin breaking and searches for scalar currents in ^{32}Ar decay," A. García, TUNL, Durham, NC, May, 2008.

"Isospin breaking and searches for scalar currents in ^{32}Ar decay," A. García, TRIUMF, Vancouver, BC, CA, July, 2008.

"Measurement of ^{23}Mg+p resonance energies," C. Wrede, 10th International Symposium on Nuclei in the Cosmos, Mackinac Island, MI, July, 2008.

"First measurement of the ^{31}P(^{3}He,t)^{31}S reaction: a study of the thermonuclear $^{30}\mathrm{P}(p,\gamma)^{31}$S reaction rate," C. Wrede, 10th International Symposium on Nuclei in the Cosmos, Mackinac Island, MI, July, 2008.

"Methods for deploying ultra-clean detectors," A. G. Schubert on behalf of the Majorana Collaboration, APS April Meeting, St. Louis, MO, April, 2008.

"Using neutrinos to study the earth," N. R. Tolich, APS April Meeting, St. Louis, MO, April, 2008.

"Neutrino detectors," N. R. Tolich, Neutrino Geoscience, Sudbury, Canada, September, 2008.

"Using neutrinos to study the Earth," N. R. Tolich, Neutrino Frontiers, Minneapolis, MN, October, 2008.

"Evolution of parton fragmentation in nuclear collisions," T. A. Trainor, 4^{th} Int. Workshop on high-p_t physics at LHC '09, Seminar, Prague, Czechoslovakia, February, 2009.

"Probing parton-medium interactions in heavy ion collisions with STAR," T. A. Trainor, Diffraction 2008, Seminar, La Londes-les-Maures, France, September, 2008.

"Universal centrality and collision-energy trends for v2 measurements from two-dimensional angular correlations," D. T. Kettler, Hot Quarks, Estes Park, CO, August, 2008.

"Questioning hydro at RHIC: is it QCD all the way down?," T. A. Trainor, Theory seminar, BNL, May, 2008.

"STAR recent results and perspective," T. A. Trainor, Plenary STAR talk, RHIC-AGS Users meeting, BNL, May, 2008.

"Minijets and their interactions," T. A. Trainor, Workshop seminar, BNL, May, 2008.

"Semiotics of heavy ion collisions," T. A. Trainor, Workshop seminar American Chemical Society, New Orleans, LA, April, 2008.

"Planck scale test of Lorentz invariance with a spin pendulum," E. G. Adelberger, Michigan Quantum Summer School, Ann Arbor MI, June, 2008.

“Tests of the Equivalence Principle,” E. G. Adelberger, Michigan Quantum Summer School, Ann Arbor MI, June, 2008.

“Sub-millimeter test of the gravitational inverse-square law,” E. G. Adelberger, Michigan Quantum Summer School, Ann Arbor MI, June, 2008.

“Sub-millimeter test of the gravitational inverse-square law: motivations, techniques and results,” E. G. Adelberger, 418th WE-Heraeus Seminar: Models of Gravity in Higher Dimensions - From Theory to Experimental Search - Bremen, Germany, August, 2008.

“A low-energy frontier of particle physics,” E. G. Adelberger, Colloquium, CERN, Geneva Switzerland, September, 2008.

“Testing Enstein’s ‘happiest idea’ by watching things fall sideways,” E. G. Adelberger, Phi Beta Kappa Visiting Scholar Lecture, Valparaiso University, Valparaiso, IN, September, 2008.

“Testing Enstein’s ‘happiest idea’ by watching things fall sideways,” E. G. Adelberger, Phi Beta Kappa Visiting Scholar Lecture, College of William and Mary, Williamsburg VA, October, 2008.

“Testing Enstein’s ‘happiest idea’ by watching things fall sideways,” E. G. Adelberger, Phi Beta Kappa Visiting Scholar Lecture, Loyola College in Maryland, Baltimore MD, October, 2008.

“Testing Enstein’s ‘happiest idea’ by watching things fall sideways,” E. G. Adelberger, Phi Beta Kappa Visiting Scholar Lecture, UC Berkeley, Berkeley CA, November, 2008.

“Short-distance gravity: from Newton to Einstein to Strings,” E. G. Adelberger, Phi Beta Kappa Visiting Scholar Lecture, University of North Carolina, Chapel Hill NC, January, 2009.

“Short-distance gravity: from Newton to Einstein to Strings,” E. G. Adelberger, Phi Beta Kappa Visiting Scholar Lecture, Furman University, Greenville SC, January, 2009.

“Short-distance gravity: from Newton to Einstein to Strings,” E. G. Adelberger, Phi Beta Kappa Visiting Scholar Lecture, University of Connecticut, Storrs CT, February, 2009.

“Short-distance gravity: from Newton to Einstein to Strings,” E. G. Adelberger, Phi Beta Kappa Visiting Scholar Lecture, Bucknell University, Lewisburg PA, March, 2009.

“Short-distance gravity: from Newton to Einstein to Strings,” E. G. Adelberger, Phi Beta Kappa Visiting Scholar Lecture, Washington & Jefferson College, Washington PA, March, 2009.

*UW collaborators for the various CENPA research groups are listed below (April 1, 2008 - March 31, 2009):

KamLAND Collaborators: K. Tolich

NA49 Collaborators: J. G. Cramer

SNO Collaborators: J. F. Amsbaugh, T. H. Burritt, G. A. Cox-Mobrand, P. J. Doe, C. A. Duba, G. C. Harper, M. A. Howe, S. McGee, A. Myers, N. S. Oblath, R. G. H. Robertson, N. Tolich, B. A. VanDevender, T. D. Van Wechel, B. L. Wall, J. F. Wilkerson

STAR Collaborators: H. Bichsel, J. G. Cramer, D. T. Kettler, R. J. Porter, D. J. Prindle and T. A. Trainor. In cases where some CENPA personnel played a major role in a STAR publication, their names are listed explicitly.

11.5 Ph.D. degrees granted

Data Integrity and Electronic Calibrations for the Neutral Current Detector Phase Measurement of the 8B Solar Neutrino Flux at the Sudbury Neutrino Observatory, Adam Cox-Mobrand, (January, 2008)[1].

Precise Measurement of the ^{7}Be(p,γ)^{8}B *S-factor*, Erik C. Mohrmann (August, 2008).

The Electron-Capture Branch of ^{100}Tc *and Implications for Neutrino Physics*, Sky Sjue (December, 2008).

[1] Also reported in the CENPA 2008 annual report.